

Analysis report on the $ep \rightarrow e'p'\pi^+\pi^-$ reaction in the CLAS detector with a 1.515 GeV beam for $0.2 < Q^2 < 0.6$ GeV 2 and
 $1.3 < W < 1.6$ GeV

G. Fedotov^a, V. Burkert^b, L. Elouadrhiri^b, V. Mokeev^{a,b}

^a*Moscow State University,
Vorob'evi gory, 119899 Moscow, Russia*

^b*Thomas Jefferson National Accelerator Facility,
12000 Jefferson Avenue, Newport News, Virginia, 23606*

Contents

1 Physics motivation	4
1.1 Axial $N\Delta$ transition form factor	4
1.2 N^* physics	6
2 Event selection	9
2.1 Particles identification	9
2.1.1 Electron identification	9
2.1.2 Positive hadron identification	11
2.2 Momentum corrections	13
2.2.1 Electron momentum corrections	13
2.2.2 Proton momentum corrections (Energy loss)	15
3 Other cuts and corrections	20
3.1 Fiducial cuts	20
3.1.1 Electron fiducial cuts	20
3.1.2 Hadron fiducial cuts	23
3.2 Bad scintillators removal	23
3.3 Čerenkov counter efficiency	26
3.4 Target stability and normalization	26
3.5 vertex cut	28
3.6 Missing energy cut	28
3.7 Exclusivity cut	28
3.8 Cuts summary	28
4 Cross section calculation	30
4.1 Selected 2π events and 2π cross sections	30
4.2 Efficiency evaluation	36
4.3 Interpolation of cross sections to the kinematics areas corresponded to zero efficiency	39
5 Radiative corrections	42
6 Correction for binning effects	44

7 Systematic errors	46
7.1 Integration	46
7.2 Fiducial cuts	46
7.3 Missing mass cut	46
7.4 Errors due to normalization, electron identification and electron detection efficiency	48
7.5 Systematic errors summary	49
8 Conclusions	51
Appendix A: Measured cross section and fit within a framework of JM05	52
Bibliography	93

Chapter 1

Physics motivation

There are two major objectives for analysis of double charged pion production at low W and Q^2 :

- extraction of transition $p \rightarrow \Delta$ axial form factor;
- the studies of $P_{11}(1440)$ and $D_{13}(1520)$ photo and poorly determined 2π hadronic coupling at the photon virtualities $Q^2 < 0.5$ GeV 2 , corresponded to the maximal sensitivity to meson cloud contribution.

1.1 Axial $N\Delta$ transition form factor

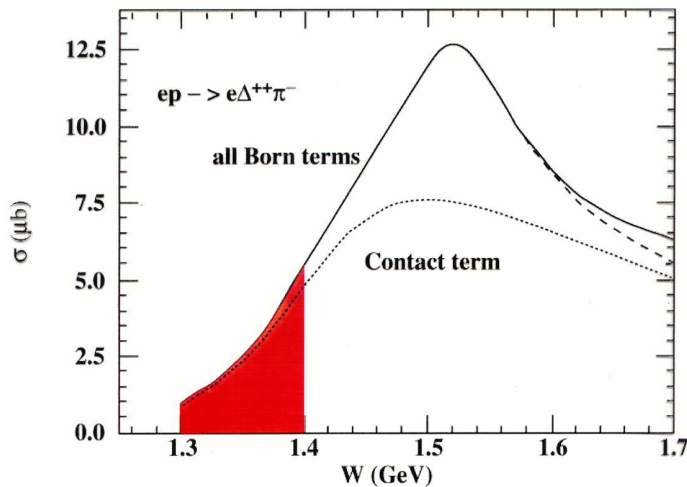


Figure 1.1: W dependence of total $ep \rightarrow e\Delta^{++}\pi^-$ cross section (solid curve) and contact term contribution (dashed curve).

Current algebra [1] relates contact term in 2π production non-resonant mechanisms to the axial transition $p \rightarrow \Delta$ form factors. The contact term could be fitted to the data

within the framework of JLAB-MSU dynamical model [2–5] for double charged pion production. Contact term has leading contribution to the double charged pion production at $W < 1.4$ GeV, as it shown on Fig. 1.1. Therefore analysis of CLAS data at $W < 1.4$ GeV within the framework of model [2–5] enable us to extract contact term and subsequently through current algebra [1] to extract $p \rightarrow \Delta$ axial transition form factor.

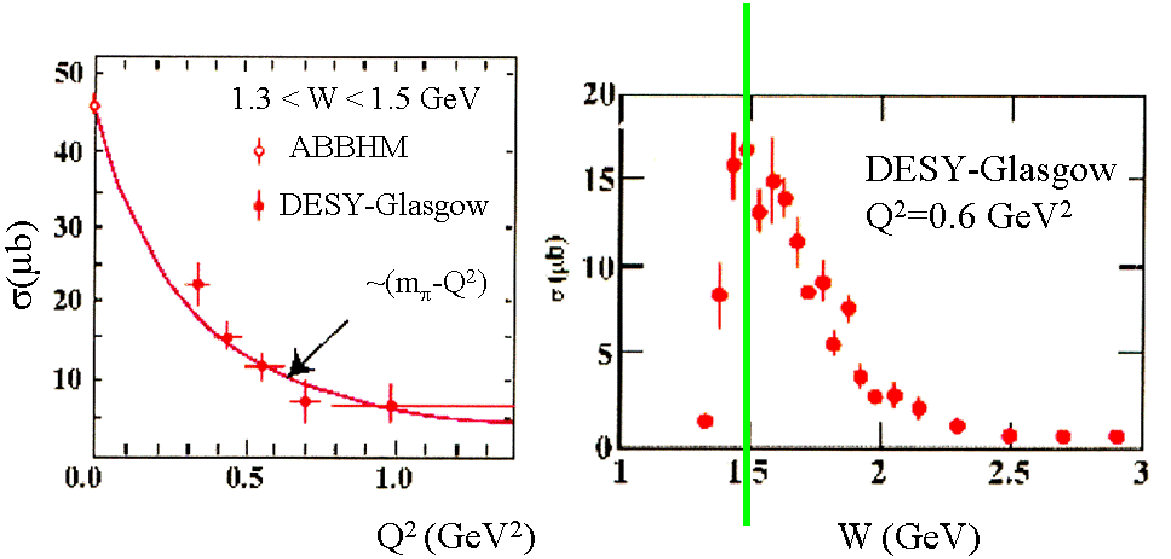


Figure 1.2: The total cross section for $\gamma_v p \rightarrow \pi^- \Delta^{++}$ as function of Q^2 in the threshold region ($1.3 < W < 1.5$) GeV.

Figure 1.3: The total cross section for $\gamma_v p \rightarrow \pi^- \Delta^{++}$ as function of W averaged over Q^2 interval $0.3 - 1.4$ GeV 2 .

So far the data on axial form factors were restricted by diagonal $p \rightarrow p$ transitions only [6–8]. Data on transition $p \rightarrow \Delta$ axial form factor are absent up to date. The reason for that is limited capability of previous experiments to determine $\gamma_v p \rightarrow \pi^- \Delta^{++}$ cross sections in electroproduction. Previous data on measured cross sections are shown on Fig. 1.2– 1.4. To provide information on Q^2 dependence of Δ electroproduction cross section we need to study electroproduction in a wide Q^2 region. To collect sufficient statistic with pulsed electron beam (and small detector acceptance used in previous experiments) wide W bin was required ~ 200 MeV. At low $W < 1.5$ GeV contact term vary considerably in so wide interval of averaging. This circumstance predated extraction of reliable information on $p \rightarrow \Delta$ axial transition form factor. Measurements with near 4π detector CLAS on continuous electron beam open up new opportunities to extract contact term in $\pi\Delta$ electroproduction. As it is shown on Fig. 1.4 recent CLAS measurements enable us to measure W - dependence of $\gamma_v p \rightarrow \pi^- \Delta^{++}$ cross section with pretty good resolution ~ 25 MeV. For such fine W resolution contact term actually does not change within W - bin size. So the CLAS data allow us to extract transition $p \rightarrow \Delta$ axial form factor for the first time.

The axial form factors provide new insight into internal structure of nucleon. N^* photo-couplings $A_{1/2}$, $A_{3/2}$, $C_{1/2}$ correspond to vector transition electromagnetic currents. Axial form factors result from axial transition hadronic currents with emission of pseudo-scalar

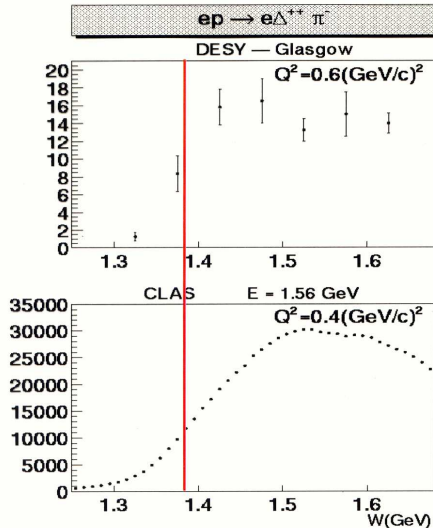


Figure 1.4: W dependence of reaction yield for $ep \rightarrow e\Delta^{++}\pi^-$ obtained in DESY (top plot) and JLAB (bottom plot).

meson. $p \rightarrow \Delta$ axial transition form factor was studied extensively in various quark models of baryons [9]. Recently this quantity is studied based on fundamental QCD within the framework of lattice simulation [10]. Therefore first data on axial transition $p \rightarrow \Delta$ form factor may provide direct confrontation between measured observables and predictions from fundamental QCD.

1.2 N^* physics

Analysis of recent CLAS data on single pion production by virtual photons at $Q^2 = 0.4$ and 0.65 GeV^2 [11] reveal compelling evidences for considerable contribution from meson cloud effects to the structure of $P_{11}(1440)$. On Fig. 1.5 experimental data from CLAS are compared to evaluation within the framework of various model approach. The closest to data prediction for $P_{11}(1440)$ photocouplings come from model [2–5] which is based on assumption on considerable meson cloud contribution. The 2π data obtained in this analysis cover Q^2 area between $0.2 - 0.5$ GeV^2 , which corresponds to the maximal sensitivity to meson cloud effects, as it possible to see from Fig. 1.6. In double charged pion production an Δ excitation is not possible kinematically. Therefore the signal from $P_{11}(1440)$ in 2π exclusive channel is clean and is not contaminated by the Δ - tail as in the single pion production. Moreover combined analysis of single and double charged pion production data from CLAS enables us to extract most reliable information on N^* photocouplings with essentially reduced systematical uncertainties, caused by phenomenological separation between resonant/background mechanisms. Single and double charged pion production combined at $W < 1.6$ GeV account for almost 100% of the total photon proton cross section. Non-resonant mechanisms in these two exclusive channels are entirely different. Therefore successful description both single

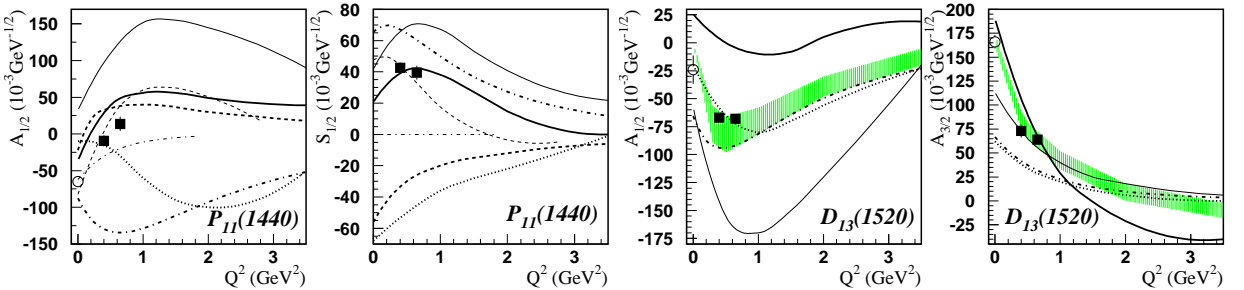


Figure 1.5: Helicity amplitudes for $P_{11}(1440)$ and $D_{13}(1520)$ electroexcitation on protons. Full boxes are average values of results obtained in the analysis of π electroproduction data [11]. Open circles at $Q^2 = 0$ are the RPP estimates [13]. Shadowed area [14] corresponds to the results obtained from the existing Bonn, DESY, and NINA data, and from JLAB measurements of η electroproduction [15]. Bold and thin solid curves correspond to relativistic and non-relativistic quark model calculations in [16]. Bold dashed curves correspond to the light-front calculations of [17, 18]. Dotted, bold dashed-dotted and thin dashed curves correspond to the quark models of [19–21]. Thin dashed-dotted curves are the predictions obtained assuming that the $P_{11}(1440)$ is a q^3G hybrid state [22].

Table 1.1: Hadronic BF $P_{11}(1440)$ and $D_{13}(1520)$ to 2π final states [23].

Resonance	Channel	Pitt-ANL (%)	KSU (%)	PDG (%)
$P_{11}(1440)$	$\pi\Delta$	16 ± 1	22 ± 3	$20 - 30$
$D_{13}(1520)$	$\pi\Delta$	16 ± 3	5 ± 3	$10 - 20$
	ρp	9 ± 1	21 ± 4	$15 - 25$

and double pion data with the same N^* photocouplings represent sensitive test for validity of approaches used both for single and double pion channel analysis.

Combined analysis of single and double pion production data at low Q^2 will provide considerable extension of available data on N^* photocouplings for $P_{11}(1440)$ and $D_{13}(1520)$ states shown on Fig. 1.7. Moreover we will be able to obtain most reliable data on N^* photocouplings at Q^2 corresponded to the maximal sensitivity to meson cloud effects. Therefore results will have considerable impact on understanding of the role of quark meson interactions expected from fundamental phenomenon of chiral symmetry breaking at hadronisation distance scale [12].

Major hadronic decay for $P_{11}(1440)$ and $D_{13}(1520)$ states go to πN final state. The information for complementary hadronic 2π decays for $P_{11}(1440)$ and $D_{13}(1520)$ is still considerably uncertain (see table 1.1). Our analysis may allow to improve knowledge on 2π hadronic decays for $P_{11}(1440)$ and $D_{13}(1520)$. Analysis of 6 available Q^2 - bins combined may enable us to extract reliable data on 2π hadronic couplings for mentioned above N^* 's. Combined fit of various Q^2 - bins provides useful constraint: the 2π hadronic couplings should be Q^2 - independent.

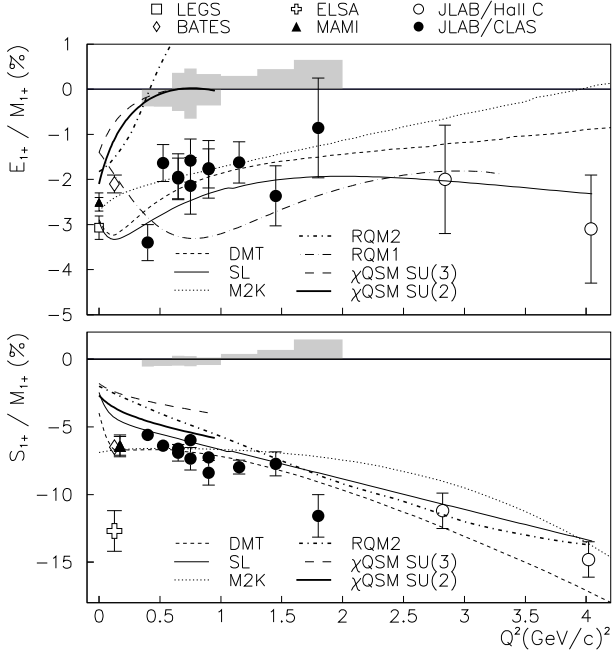


Figure 1.6: Q^2 dependence of electric (E_{1+}) and scalar (S_{1+}) quadrupole/magnetic dipole ratios from experiment [24] (bold circles). Shaded bands show systematic errors. Other points are from BATES [25], ELSA [26], JLAB/Hall C [27], LEGS [28] and MAMI [29, 30]. The curves show recent model calculations: χ QSM [31], DMT [32], SL [33], M2K [32, 34], RQM1 [19], RQM2 [35].

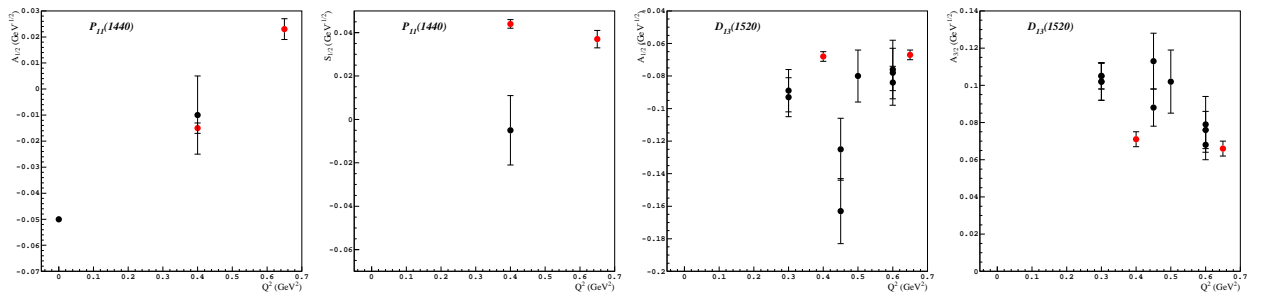


Figure 1.7: Q^2 dependence of helicity amplitudes for $P_{11}(1440)$ and $D_{13}(1520)$. Black circles correspond JLAB data, red circles - world data.

Chapter 2

Event selection

This analysis is based on the experimental data taken during 1999 e1c run period with electron beam energy of $E_b = 1.515$ GeV. The analysis is performed on ≈ 420 million triggers taken at the $I_t = 1500$ Amps torus current setting. We used cooked files obtained from the PROD-1-9 version of the code and reduced to HBOOK ntuples as "quasi-DST" format with smaller size, containing the basic information. Only the qualified "golden" runs have been analyzed. A run is classified as "GOLD" if there were no obvious detector, target, beam stability, hardware failures. These runs are listed on the http://www.jlab.org/~claschef/cooked_1.5.html web page and counts 50 runs (692 files).

2.1 Particles identification

2.1.1 Electron identification

The hardware trigger in CLAS was based on a coincidence between Čerenkov counter and electromagnetic calorimeter. Discriminator threshold in the Čerenkov was put at a signal level of less than a single photoelectron produced on the photocathode, to avoid losing good events and to perform some rejection of pion background. Threshold in the calorimeter was set such to cut off events as close as possible to the kinematic edges of the W and Q^2 domain covered by the measurement, but far enough to keep the low energy contamination within reasonable limits.

So first of all it was necessary to study the calorimeter response to identified electrons and develop appropriate cuts to eliminate in part pion contamination. In the Calorimeter, the electrons and pions have different energy deposition patterns. An electron produces an electromagnetic shower where the deposited energy is proportional to the electron momentum whereas a π^- loses a constant amount of energy per scintillator (2 MeV/cm) independently of its energy. The π^- is called a minimum ionizing particle (MIP).

We identify as possible electron the first in time negative charged particle detected in calorimeter. To select among such particles true electrons, discussed above peculiarities in π^-/e^- energy losses were exploited. The distributions of total energy deposited in calorime-

ter by first negative particles for various values of particle momenta versus momentum of electrons for different electron scattering angles are shown on the left part of Fig. 2.1. Events between red lines were identified as electrons. So, we isolate electrons applying the following cut on the total energy deposited in calorimeter EC_{tot} as a function of ingoing particle momentum P :

$$EC_{tot} > 0.217 * P - 0.09, \quad EC_{tot} < 0.36 * P + 0.07 \quad (2.1)$$

Threshold effects from the calorimeter were controlled applying Kim Egiyan's function [36] as a fiducial cut on the outgoing electron energy ($E_{e'} < 500$ MeV).

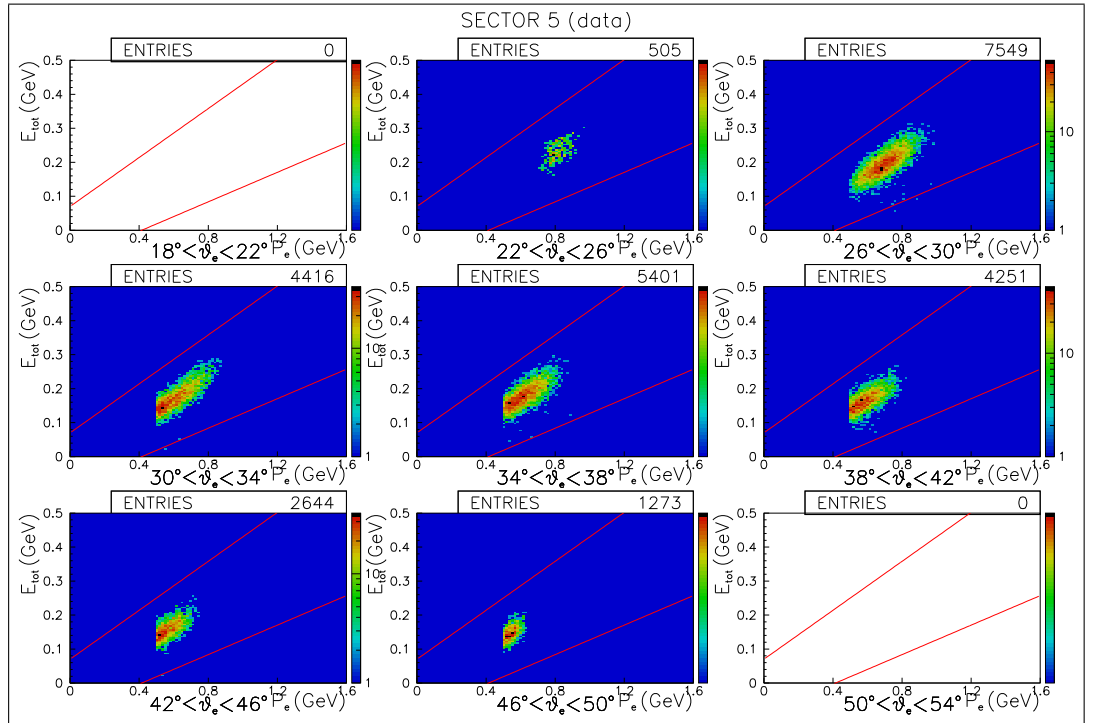


Figure 2.1: Total energy deposited in calorimeter versus momentum of electrons for different electron scattering angles for Sector 5. Red lines show the cuts. Events inside cuts were identified as electrons.

To improve the π^-/e^- separation quality we also apply cut in the number of photoelectrons ($N_{phe} \geq 2.5$). In Fig. 2.2 we show the plot of the outer energy released in the calorimeter versus the inner energy: before (top plot) and after (bottom plot) EC and photoelectron cuts. As it shown on Fig. 2.2 after EC and photoelectron cuts most of the pions in the left spot disappear.

However photoelectron cut also eliminate part of electrons. It is possible to see from the plots on Fig. 2.3, where we present the distributions for photoelectrons, collected at various W -bins. Blue shadowed areas correspond to drop-out electrons. To recover these eliminated

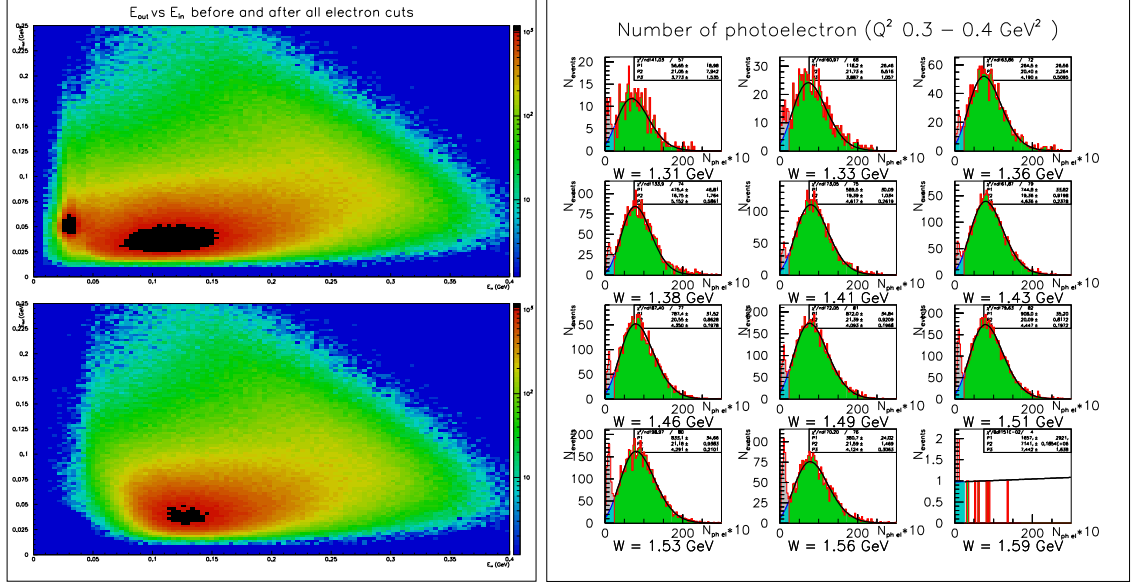


Figure 2.2: Forward calorimeter outer energy versus inner energy deposition. Before (top plot) and after (bottom plot) EC and photoelectron cuts.

Figure 2.3: Distribution of photoelectron in the Čerenkov counter for $0.3 < Q^2 < 0.4 \text{ GeV}^2$ various W ranges. Curves represent Poisson fit.

electrons we used the following procedure. Photoelectron distributions at $N_{phe} \geq 2.5$ were fitted by Poisson curves (2.2) with P_1 , P_2 , P_3 treated as free parameters and fitted to the measured N_{phe} distributions.

$$y = P_1 \left(\frac{P_3^{\frac{x}{P_2}}}{\Gamma \left(\frac{x}{P_2} + 1 \right)} \right) e^{-P_3} \quad (2.2)$$

Quality of the fit is shown on Fig. 2.3 by black solid lines. The curves obtained were extrapolated to the areas $N_{phe} < 2.5$. In this way we derived a correction factors (2.3) for each W and Q^2 bin. This factor accounts for lost electron events after cut $N_{phe} \geq 2.5$ and represents a particular contribution to the electron detection efficiency.

$$\text{corr factor} = \frac{\text{green area}}{\text{green area} + \text{blue area}} \quad (2.3)$$

2.1.2 Positive hadron identification

Using information from Time Of Flight scintillators, particle velocity (β) was determined. The information from Drift Chambers will allow to measure particle momentum (p). Therefore, we can identify charged hadron regarding relation between particle mass, momentum

and velocity (2.4).

$$m = \frac{p\sqrt{1-\beta^2}}{\beta} \quad (2.4)$$

In events with detected electrons selected at previous step, we identified types of positive charged hadrons (π^+ or proton). Fig. 2.4 shows the velocity versus the momentum for the positive charged particles. In this plot one can see the cuts applied to select the π^+ (red curves) and the proton (yellow curves); dashed curves show estimated of explicit particle mass dependence. Cuts on Fig. 2.4 given by following formulas: (2.5) - π^+ upper cut, (2.6) - π^+ lower cut, (2.7) - proton upper and lower cuts. For the π^+ , at low momentum a narrow cut is necessary to avoid the misidentification with the e^+ .

$$\beta < \frac{(205.98 - x) \left(\frac{200-x}{200+x} \right)^{0.7} (x + 0.5)}{(200.02 + x) \sqrt{(x + 0.5)^2 + 0.019}} + 0.02 \quad (2.5)$$

$$\beta > \frac{(1. + 5. \times 1.07 \times (x - 0.07))(x - 0.07)}{(1. + 5.(x - 0.07)) \sqrt{(x - 0.07)^2 + 0.138^2}} - 0.1 \quad (2.6)$$

$$\beta < \left(\frac{x}{\sqrt{x^2 + 0.938^2}} + 0.02 \right) \frac{1.2 + 0.92x}{1 + x} \quad (2.7)$$

$$\beta > \left(\frac{x}{\sqrt{x^2 + 0.938^2}} - 0.05 \right) \frac{1. + x}{0.9 + 1.06x}$$

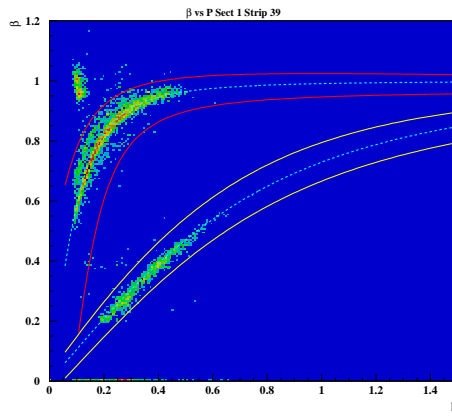


Figure 2.4: β versus momentum plot for hadrons; solid curves show the cuts used to identify pions and protons for small to medium angle scintillators; dashed curves show estimated of explicit particle mass (π^+ or proton) dependence.

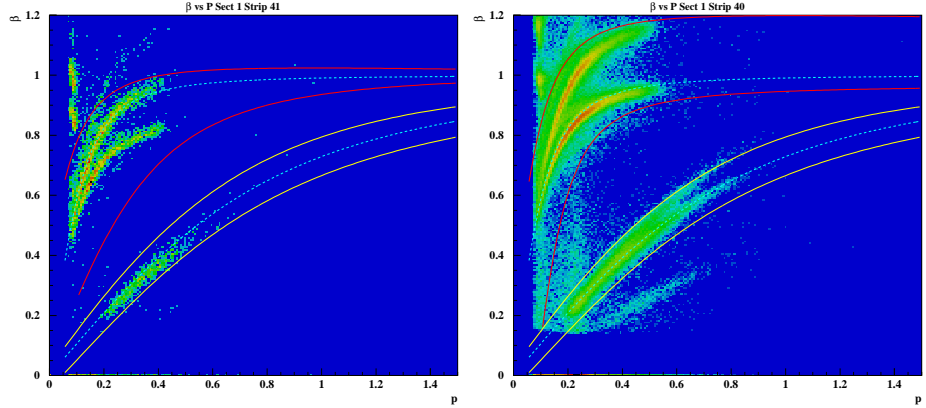


Figure 2.5: β versus momentum plot for hadrons; solid curves show the cuts used to identify pions and protons for large angle scintillators; dashed curves show estimated of explicit particle mass (π^+ or proton) dependence.

One of the problem with the Time Of Flight system was that at the backward angles the last 9 channels were actually two scintillator strips connected to a single TDC. Because the delays for these two counters were different, the time signal from these channels had two peaks, corresponding to the case in which a particle hit one or the other strip of the pair. In a case of double scintillator strips β versus momentum cuts should be broaden to select events comes from both scintillators. Fig. 2.5 shows specific cuts to select the proton and π^+ for the backward angles scintillator strips. Shifted upper cut for π^+ on the right part of Fig. 2.5 and lower cut on the left part are given by (2.8) and (2.9) respectively.

$$\beta < \frac{(205.98 - x) \left(\frac{200-x}{200+x} \right)^{0.7} (x + 0.1)}{(200.02 + x) \sqrt{(x + 0.01)^2 + 0.019}} + 0.195 \quad (2.8)$$

$$\beta > \frac{(1. + 4.5(x - 0.03))(x - 0.03)}{(1. + 5.(x - 0.03))\sqrt{(x - 0.03)^2 + 0.438^2}} + 0.1 \quad (2.9)$$

2.2 Momentum corrections

2.2.1 Electron momentum corrections

Due to possible slight misalignments in the DC position and small inaccuracies in the description of the torus magnetic field, the momentum and angle of particles may have some systematic deviation from the real value. To correct this deviation, "ad hoc" corrections to the particle momenta were introduced first by Volker Burkert. The idea is to check if some well-defined invariant quantity such as a particle mass, lies at its expected value. For instance, Fig. 2.6 (top 6 plots) shows, sector per sector, the W distributions, where elastic

peak is clearly visible. Its position however shift up to 30 MeV with respect to the nucleon mass which indicates that corrections are needed in the reconstructed electron kinematics.

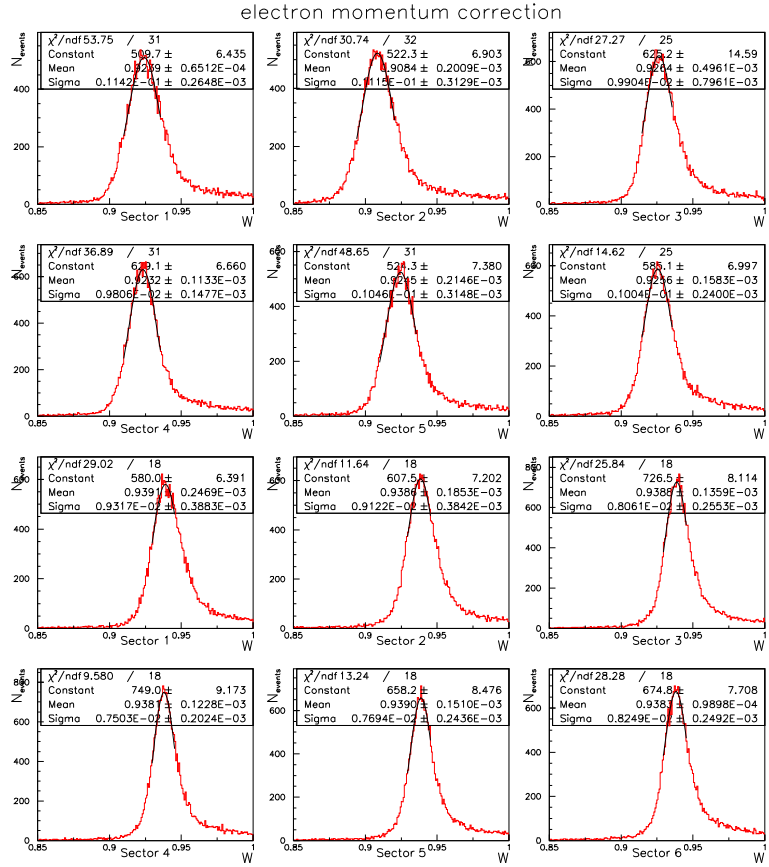


Figure 2.6: Elastic peak before (top 6 plots) and after (bottom 6 plots) electron momentum corrections.

The idea of the correction procedure is to select events with one detected electron which lies in the elastic peak and, assuming that the electron angles θ and φ are well measured, calculate its true momentum from these angles (there is a one-to-one correlation between the θ angle of the electron and its momentum). By matching the measured momentum to this true momentum, one can derive a correction function. For more detailed procedure description look [37].

Fig. 2.6 (bottom 6 plots) shows the result of such momentum correction for the elastic case. One clearly sees that now all proton peaks are relatively well centered on 0.938 GeV (maximum shifts is 1.1 MeV) and the width of peak is narrowed.

2.2.2 Proton momentum corrections (Energy loss)

In 2π reaction, the proton is a slow recoil particle. In terms of energy loss, it will therefore be very sensitive to the amount of material traversed between the target and scintillators. This obviously causes the reconstructed momentum to be lower than the initial momentum of the particle at the vertex of the reaction. This correction factor can be derived from GSIM. We generated protons corresponding to the kinematics of 2π reaction and reconstructed them using GSIM and RECSIS with switched on and off detector material. The event distributions for differences between generated and reconstructed proton momenta with material on/off are presented on Fig. 2.8 and Fig. 2.9, respectively. Various plots correspond to proton momentum range covered in our experiment. One observes that peaks position on Fig. 2.8 are systematically lower than on Fig. 2.9. The differences between peak positions with material on/off represent the correction factor for proton momentum as a function of the initial (before interaction with matter) proton momenta. We also studied the dependence of this correction factor from the angle of proton emission from the target. In Fig. 2.10 we show the dependence of correction factor as a function of proton momenta for various proton emission angles. Plots on Fig. 2.11 represent angular dependencies of correction factor for various proton momenta. Fitting 1-dimensional slices of Fig. 2.10 and Fig. 2.11 we have determined 2-dimensional interpolation function for proton momentum correction factor in an entire area of proton emission angles and momenta, accessible in our experiment. Derived in this way interpolation 2-D function for proton momentum correction factor is shown in Fig. 2.7. Analytically this function is given by following formula:

$$P_{corr} = P + 0.000425/P^3 + (0.0095 - 0.01 * P) * \cos \left(\frac{1.8(\theta - 7)}{10 * P - 1.5} + 0.95 \right) + 0.03 \quad (2.10)$$

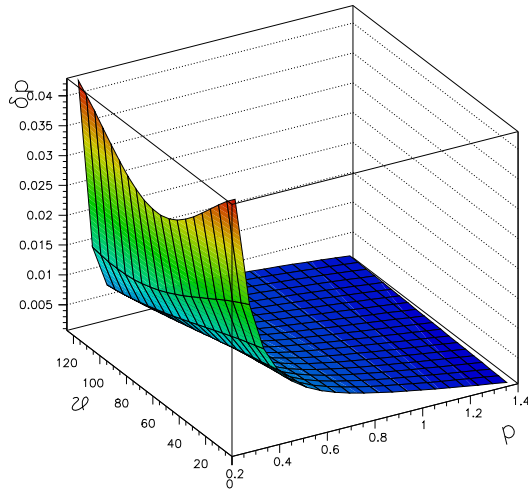


Figure 2.7: Proton momentum correction function.

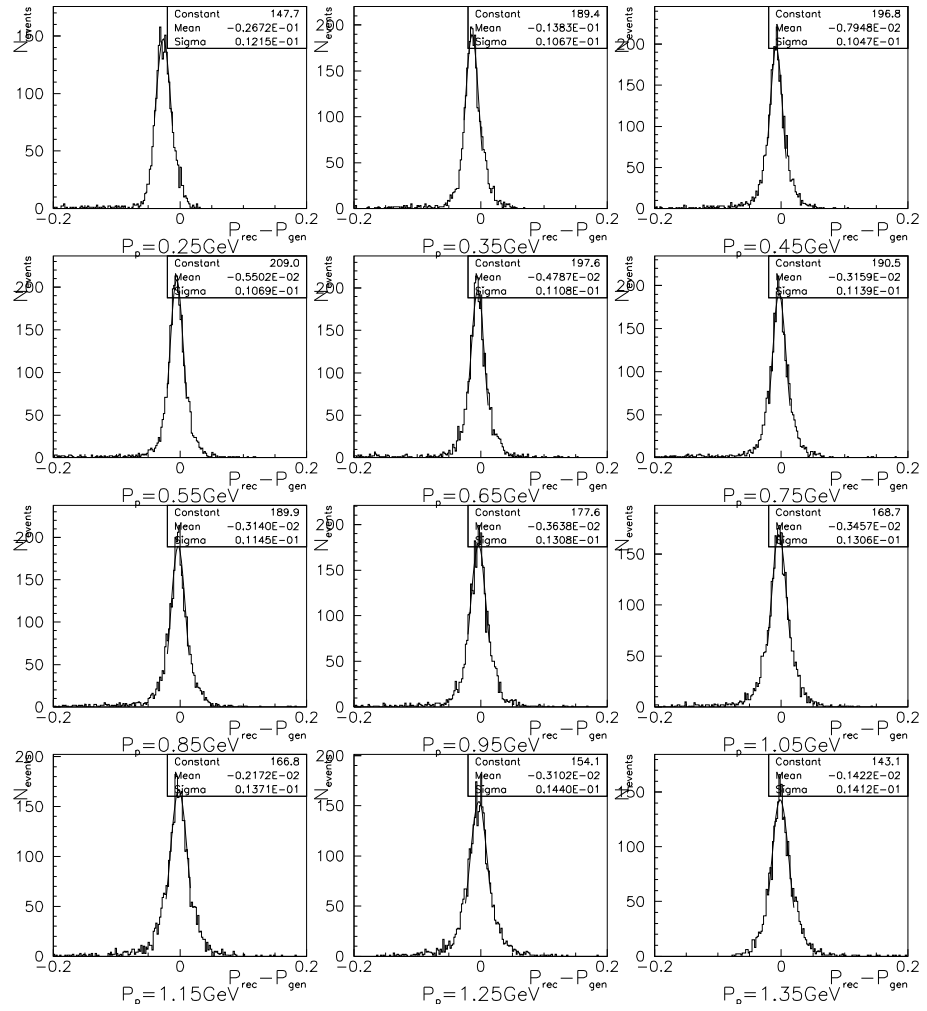


Figure 2.8: Differences between momentum of reconstructed and generated protons (detector material switched on).

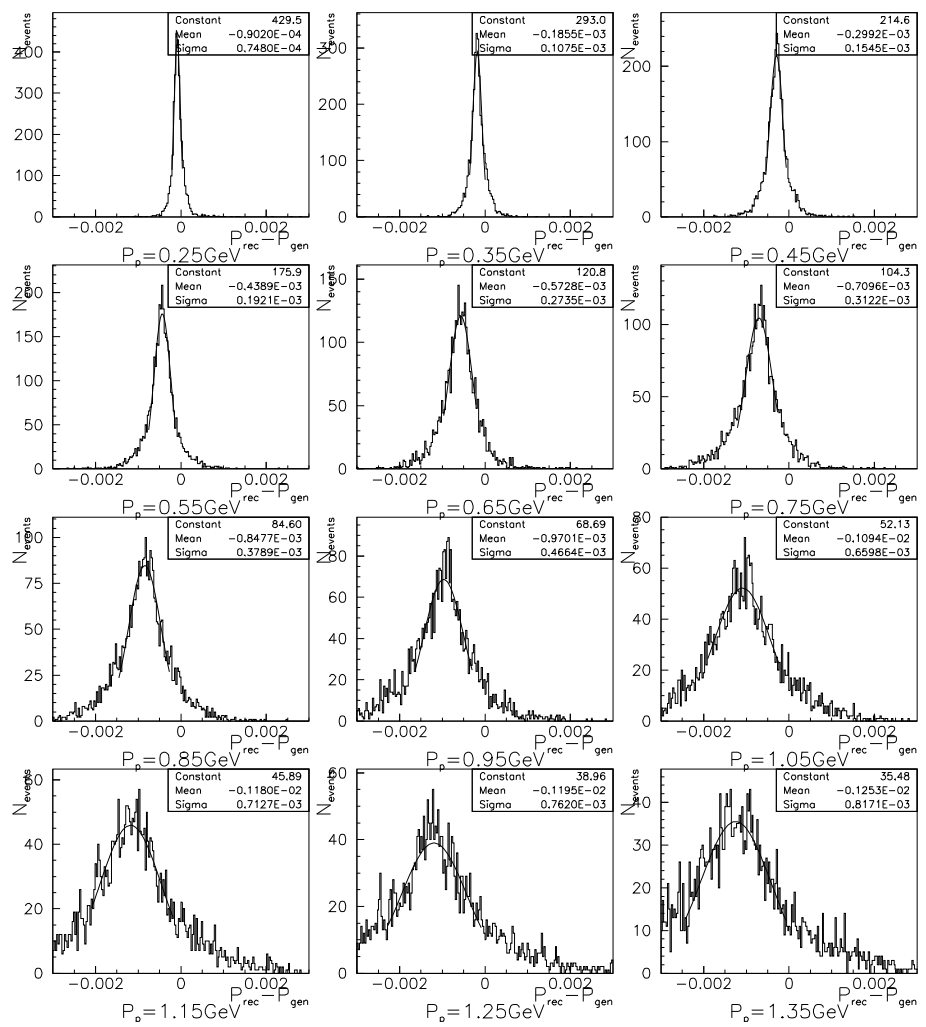


Figure 2.9: Differences between momentum of reconstructed and generated protons (detector material switched off).

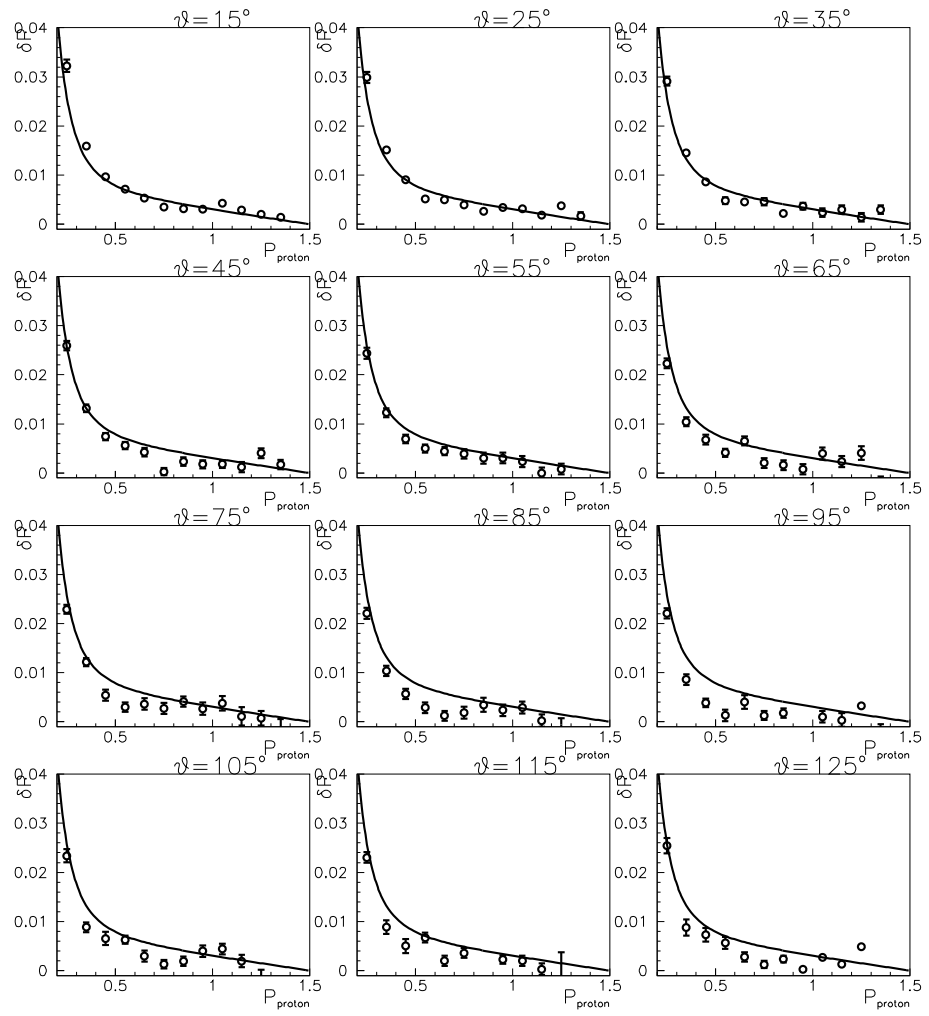


Figure 2.10: Momentum dependencies of correction factor for different angles θ .

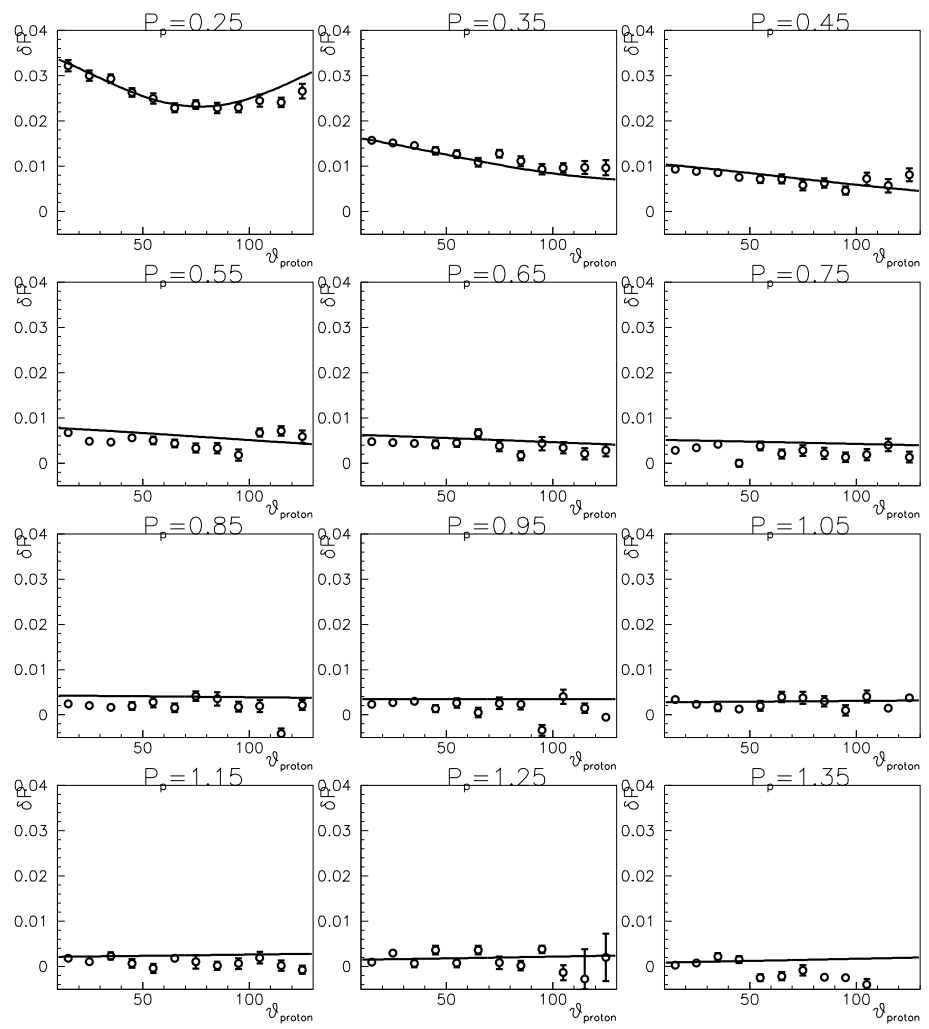


Figure 2.11: Angular dependencies of correction factor for different proton momentum p .

Chapter 3

Other cuts and corrections

3.1 Fiducial cuts

The CLAS detector has an active detection solid angle obviously smaller than 2π , being part of the space filled with the torus field coils: the angles covered by the coils are not equipped with any detection system and therefore from a "dead" area for detection. Moreover, different studies and analysis have shown that also the edges of the active area do not provide a safe region for particle reconstruction, being affected by rescattering from the coil, field distortions and similar effects. Therefore it is now common practice to accept for the analysis only events inside specific fiducial cuts, i.e. cuts on the kinematic variables (momentum and angles) of each particle, such to guarantee that the reconstructed events accepted in the analysis include only particles detected in "safe" areas of the detector, that is where the acceptance is thought to well understood. These cuts produce a reduction factor in the number of events accepted in each kinematic bin that we will call detector acceptance.

3.1.1 Electron fiducial cuts

To determine fiducial cuts for electrons we plot number of electrons versus angle φ for 6 CLAS sectors and particular angles θ and momentum interval, then we select flat regions in this distributions (green areas on Fig. 3.1). In Fig. 3.2 we report the electron fiducial cuts for all CLAS sectors in the φ versus θ plane for a particular momentum interval. The analytical shape of this cuts is given by following formulas:

$$\begin{aligned} \delta\varphi_e &= 30\sin((\theta - \theta_{min})d2r)^{\frac{(2.1-p)}{6.67}(p\frac{3375}{1500}+0.15)} \\ \theta_{max} &= 50.0^\circ; \quad \theta_{min} = 15.5 + \frac{15}{p(3375/1500)+0.15}; \quad d2r = 0.01745 \end{aligned} \tag{3.1}$$

where $\delta\varphi_e$ represents the portion of the polar angle φ_e accepted by the fiducial cut, or in other words if $\theta_{min} < \theta < \theta_{max}$ and $|\varphi| < \delta\varphi$ then the electron is accepted.

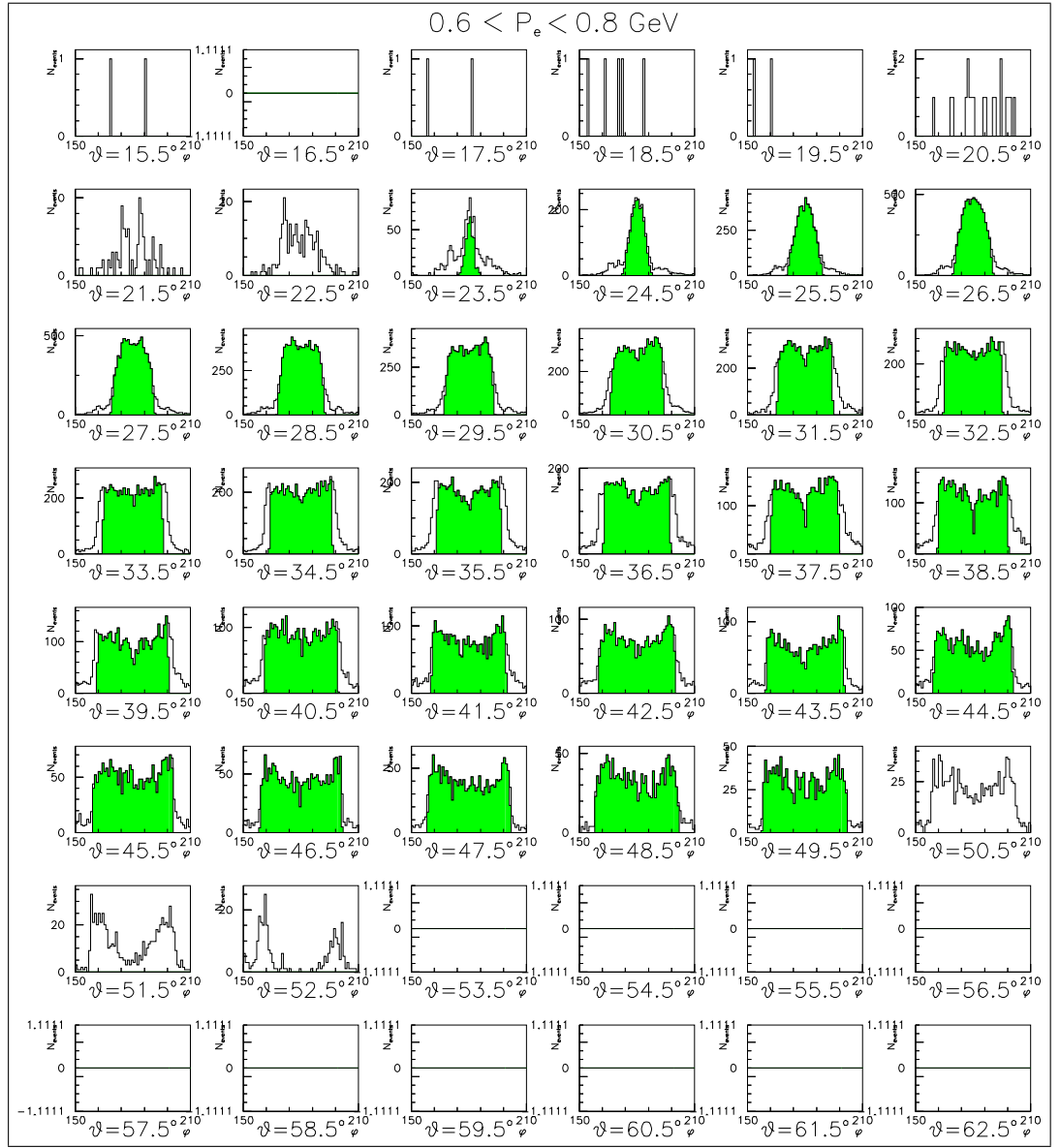


Figure 3.1: φ distributions for number of electron with momentum between 0.6 and 0.8 GeV in sector 4. Various plots represent various angles θ . Green areas represent events inside fiducial cut.

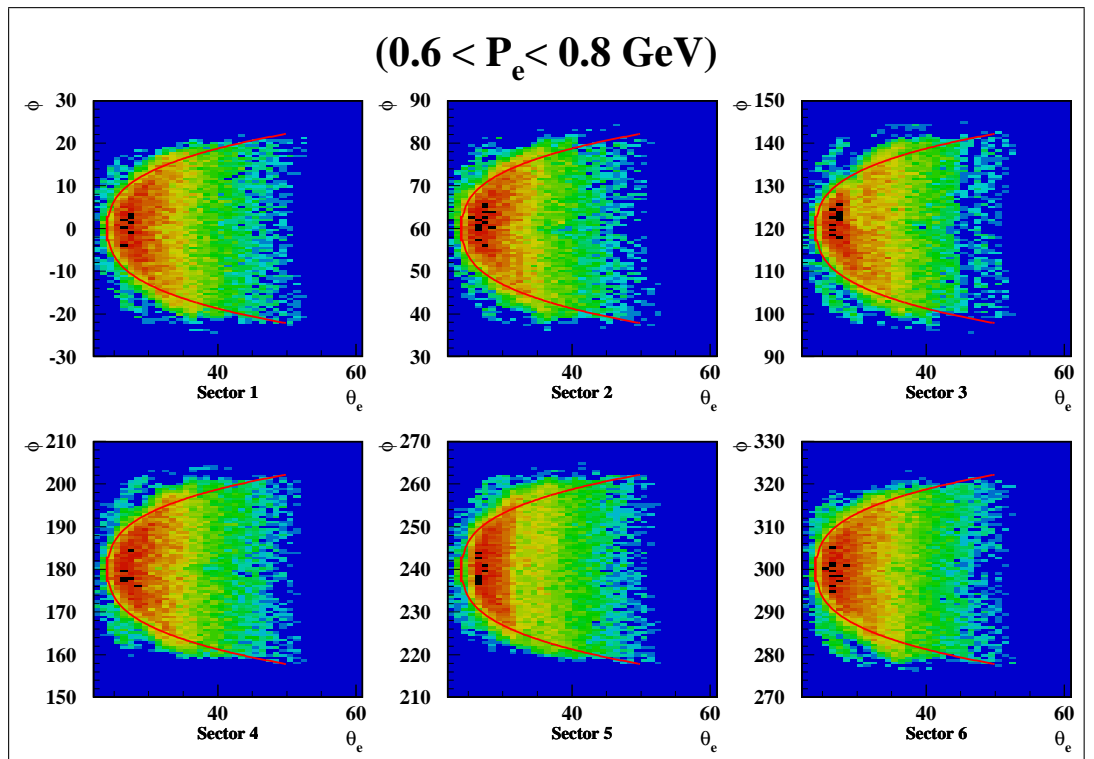


Figure 3.2: Events populated in θ & φ plane for electrons detected in 6 CLAS sectors with momentum between 0.6 and 0.8 GeV; curves show the fiducial cuts (calculated at the same average momentum).

3.1.2 Hadron fiducial cuts

Fiducial cuts for positive charged hadrons π^+ and protons (π^- were reconstructed from missing mass) were determined selecting flat areas in φ distributions. This cuts are momentum independent and given by the following formulas:

$$\begin{aligned}\delta\varphi_h^+ &= A^+(\text{sector})(1 - e^{-B^+(\text{sector})(\theta - C^+(\text{sector}))}) \\ \delta\varphi_h^- &= A^-(\text{sector})(1 - e^{-B^-(\text{sector})(\theta - C^-(\text{sector}))}) \\ \theta_{min} &= 10.0^\circ\end{aligned}\quad (3.2)$$

If $\delta\varphi^- < \varphi < \delta\varphi^+$ and $\theta > \theta_{min}$ then the positive hadron is accepted. In table 3.1 the parameters used for positive hadrons fiducial cuts are reported. In Fig. 3.3) the positive hadron fiducial cuts for all CLAS sectors in the φ versus θ plane are reported.

Table 3.1: Parameters in the fiducial cut analytic form.

Parameter	Sector 1	Sector 2	Sector 3	Sector 4	Sector 5	Sector 6
A^+	23.	23.	25.	25.	25.	23.
B^+	0.12	0.12	0.12	0.12	0.12	0.12
C^+	12.	10.	5.	2.	10.	12.
A^-	24.	24.	24.	27.	27.	25.
B^-	0.1	0.1	0.1	0.1	0.1	0.1
C^-	5.	5.	7.	9.	11.	8.

3.2 Bad scintillators removal

Some of the channels of the Time Of Flight system were dead or malfunctioning, which was manifest in the rates of events in these counters compared with the rates in the neighboring counters. For this channels we used explicit cut on the paddle number in the analysis program. In table 3.2 we report list of bad scintillators in each CLAS sector.

Table 3.2: List of bad scintillators.

	Sector 1	Sector 2	Sector 3	Sector 4	Sector 5	Sector 6
scintillator numbers	23; 38	21; 23	7; 16; 18; 23; 35; 37; 38; 42; 43; 45; 46	21; 23	2; 23; 29; 33	23; 26

To exclude some border effects we also apply fiducial cuts that excluding the events in the bad scintillators. This cuts are shown on θ versus momentum plots Fig. 3.4, Fig. 3.5 for positive hadrons and electrons respectively.

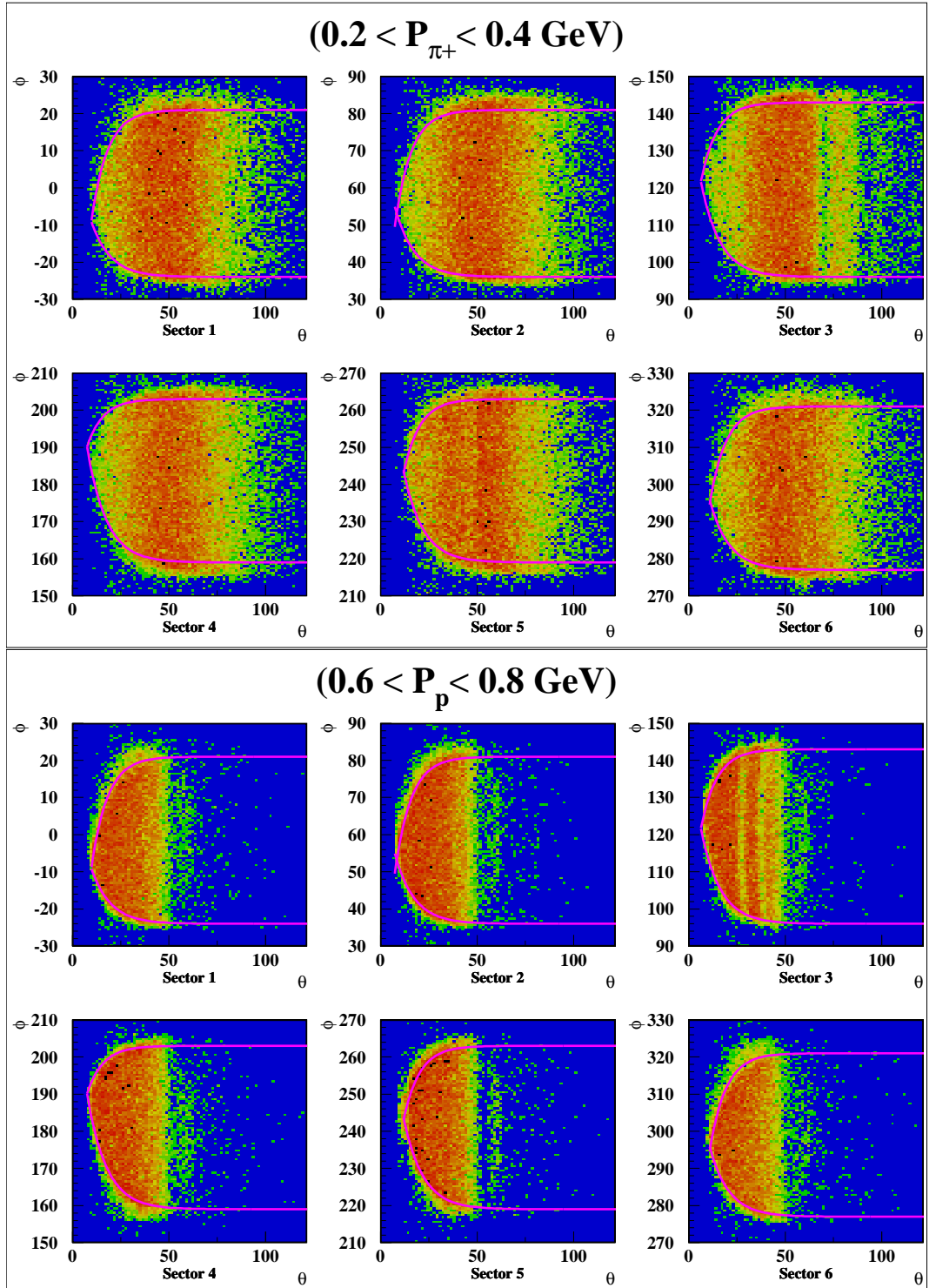


Figure 3.3: Plot of angles φ versus θ for π^+ (top) and protons (bottom) in the 6 CLAS sectors, with π^+ momentum between 0.2 and 0.4 GeV and protons momentum between 0.6 and 0.8 GeV. The curve showing the fiducial cuts is also superimposed on the plots.

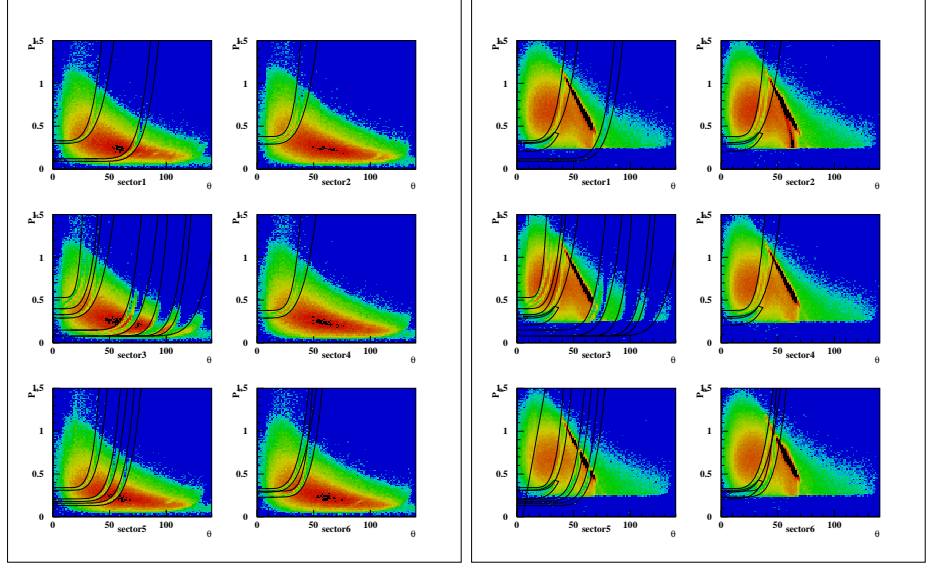


Figure 3.4: Pions (left plot) and protons (right plot) angle θ versus momentum p distributions in the 6 CLAS sectors. Pairs of curves indicate the upper and lower edges of the cuts for rejecting events in bad TOF and CC counters.

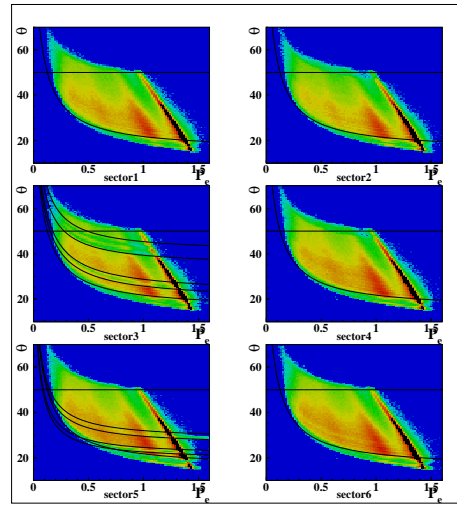


Figure 3.5: Electron angle θ versus momentum p distributions in the 6 CLAS sectors. Pairs of curves indicate the upper and lower edges of the cuts for rejecting events in bad TOF and CC counters.

3.3 Čerenkov counter efficiency

Due to shortcomings in description of Čerenkov counter in GSIM we used Alex Vlassov [38] function. Vlassov function enable us to estimate fiducial cut isolating CLAS areas with Čerenkov counter unefficiency $< 5\%$. So we collected 2π events from the CLAS areas isolated by this fiducial cut. Influence of this cut was included in overall efficiency calculations. Moreover Čerenkov counter efficiency inside fiducial area was taken from Vlassov function. On Fig. 3.6 these function shown for nine electron momentum bins in sector 1. The fiducial cuts are shown by black solid lines. Inside fiducial areas an additional requirement was applied:

$$\text{Čerenkov efficiency} > 0.95 \quad (3.3)$$

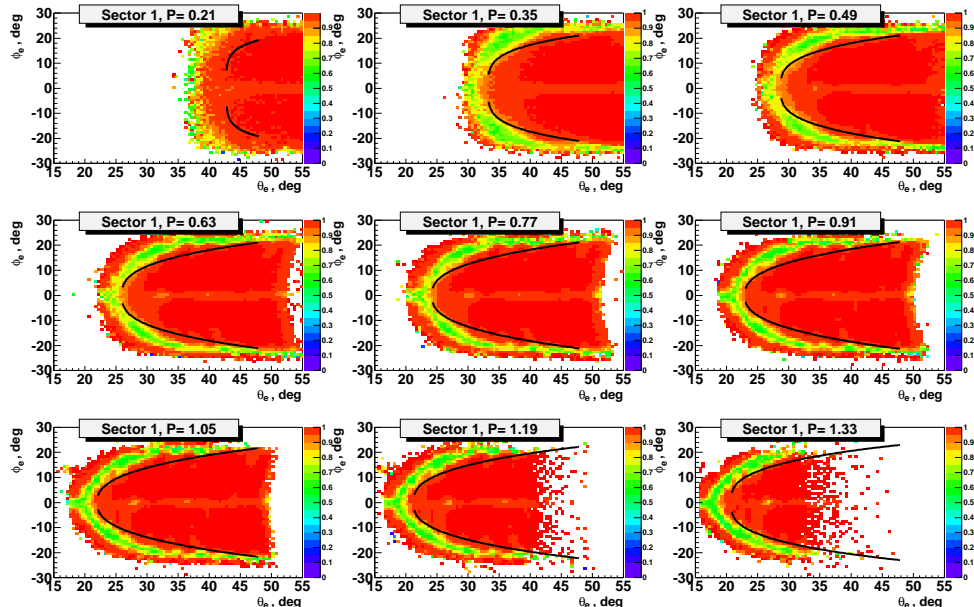


Figure 3.6: CC efficiency versus θ_e and φ_e for nine electron momentum bins in sector 1. The black curves indicate the fiducial cuts. Only regions with efficiency > 0.95 were included into analysis.

3.4 Target stability and normalization

During the 1.5 GeV portion of the e1c running period the cryogenic target was not very stable. Periodically part of the liquid hydrogen would evaporate, leaving the liquid hydrogen level below the beam position on the target, thus decreasing the effective density of the target for the run. The automatic control system recovered the liquid phase of the target within a few seconds. But these variations of the target density with time can result in errors in

the luminosity determination. For this reason, the events collected during the short time intervals, when the target density was lower than normal, were dropped from the analysis.

There are a number of ways to diagnose the problems associated with the varying target density. One of the signatures of the target getting empty is the increase of the live-time of the data acquisition system above the working range of 90% - 95%. Another is the dramatic decrease of the event rates normalized to the live-time corrected charge, measured in the Faraday cup. The live-time, 2π and the elastic scattering rates versus scaler event number are shown in Fig. 3.7. For some of the intervals between two scaler events the live-time or the event rates are outside of the imposed limits, shown by red lines. In most cases one can see correlations between such anomalies in these three plots. The events which occurred within these time intervals were ignored and the charge, corresponding to these time intervals, was subtracted from the integrated charge of the run.

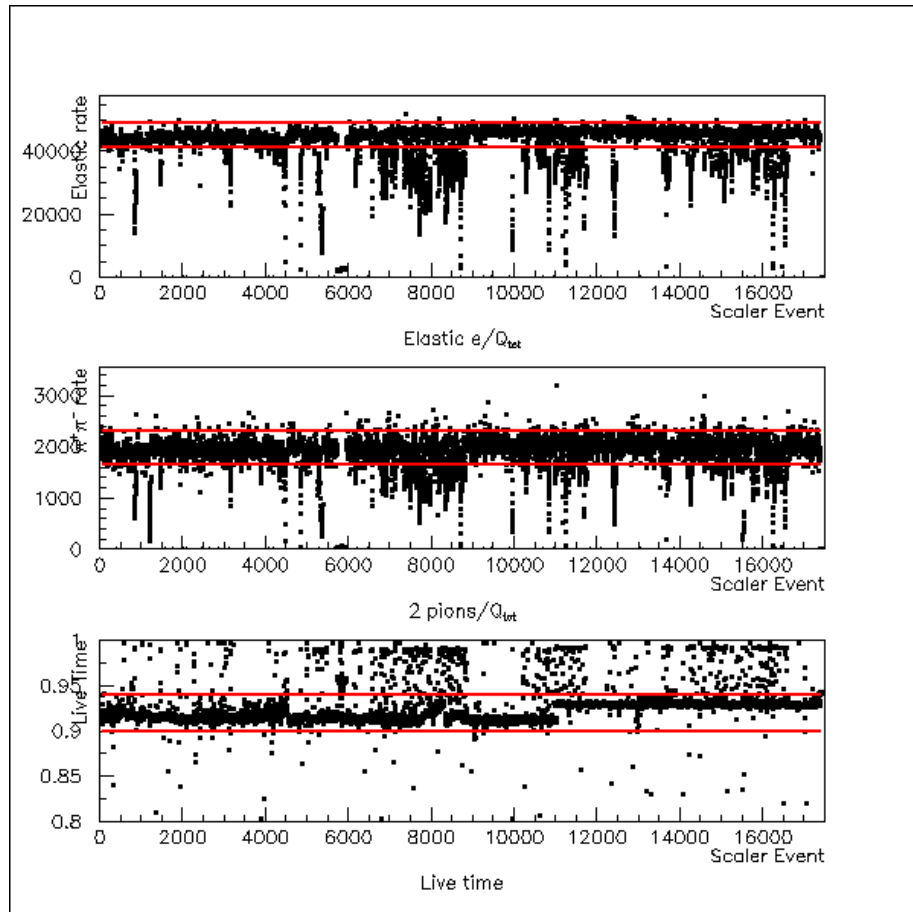


Figure 3.7: Live-time (top), the 2π rate (middle) and elastic rate (bottom), calculated using live-time corrected charge, versus scaler event number. The red horizontal lines represent the cuts used to reject the events with unstable target densities.

3.5 vertex cut

We made cuts on electron, proton and π^+ vertex reconstructions to eliminate events from target window and etc. The final cuts were chosen to be: $|z_e - z_p| < 4$ cm, $|z_e - z_{\pi^+}| < 4$ cm, $|z_p - z_{\pi^+}| < 4$ cm.

3.6 Missing energy cut

To exclude same misidentified and out of time particle we apply cut on missing energy for 2π reaction:

$$E_{beam} + m_p - E_{electron} - E_{proton} - E_{\pi^+} > 0 \quad (3.4)$$

3.7 Exclusivity cut

After the identification of the 3 particles, we ask for events with exactly electron, proton and π^+ . For these events we calculated $\pi^- X$ missing mass squared $M_{\pi^- X}^2$, which was determined as:

$$M_{\pi^- X}^2 = (P_e + P_p - P_{e'} - P_{\pi^+} - P_{p'})^2 \quad (3.5)$$

To select the exclusive process ($ep \rightarrow e' p' \pi^+ \pi^-$) we applied cut over $M_{\pi^- X}^2$ (3.6) , isolating π^- peak. This cut shown by green arrows on Fig. 3.8.

$$-0.04 < M_{\pi^- X}^2 < 0.06 \text{ GeV}^2 \quad (3.6)$$

3.8 Cuts summary

After all cuts and corrections we have around 130 000 2π events. Fig. 3.9 show Q^2 versus W distributions for eventually selected 2π events. Grid represent binning used for cross section calculation. Only full filled cells were used for analysis.

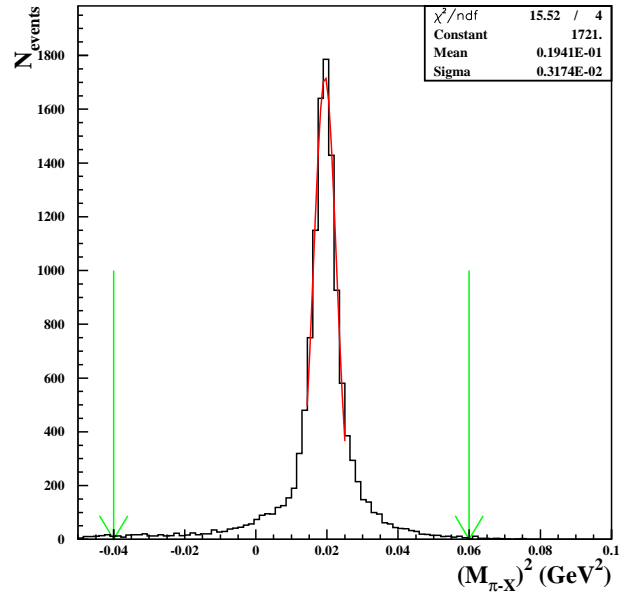


Figure 3.8: $M_{\pi-X}^2$ (GeV 2) for experimental data, green arrows show exclusivity cut.

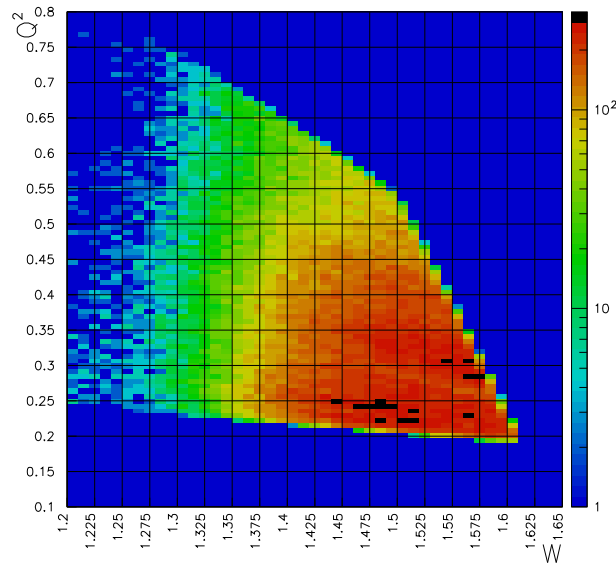


Figure 3.9: Q^2 (GeV 2) versus W (GeV) distribution for 2π events. Grid show binning used for cross section calculation.

Chapter 4

Cross section calculation

4.1 Selected 2π events and 2π cross sections

3-body final state is unambiguously determined by 5 kinematics variables. Indeed, 3 final particles could be described by $4 \times 3 = 12$ components of theirs 4-momenta. All these particles are on-shell. So, it gives us 3 restrictions $E_i^2 - P_i^2 = m_i^2$ ($i = 1, 2, 3$). Energy-momentum conservation impose 4 additional constraints for the final particle four momentum components. So, eventually we remain with 5 kinematics variables, which determined unambiguously the 3-body final state kinematics. In electron scattering process $ep \rightarrow ep'\pi^+\pi^-$ we also have variables W , Q^2 beyond the hadronic final state kinematics variables. So electron scattering cross section for double charged pion production should be 7-differential: 5 variables for the final hadrons plus W and Q^2 determined by electron scattering kinematics. Such 7-differential cross sections may be written as $\frac{d^7\sigma}{dWdQ^2d^5\tau}$, where $d^5\tau$ is 5-differential phase space, describing the final hadron kinematics.

Several sets of 5 variables for description of the final hadron kinematics may be used. We adopted the following set of variables:

- invariant mass of first pair of particles M_{12} ;
- invariant mass of the second pair of particles M_{23} ;
- first particle solid angle Ω ;
- the angle between two planes: one of them (plane A) is composed by 3-momenta of the virtual photons and first hadron, second plane (plane B) is composed by 3-momenta of two other hadrons (see Fig. 4.1).

Selected events were collected in 7-dimensional cells, corresponded to the variables: W , Q^2 , invariant mass of first pairs of particles M_{12} and second pair of particles M_{23} , solid angle for the first final particle, the angle α between two planes. The cross sections were estimated in CM frame. So, four-momenta of the final particles described above, initially measured in

lab frame, were boosted to the CM frame. We calculated cross section for various assignment for the first, second and third final hadrons:

- invariant mass of the $p\pi^+$ pair, invariant mass of the $\pi^+\pi^-$ pair, proton spherical angles θ_p and φ_p and angle $\alpha_{\pi^+\pi^-}$ between planes B (composed by momenta of $\pi^+\pi^-$ pair) and A (composed by initial and final protons);
- invariant mass of the $\pi^-\pi^+$ pair, invariant mass of the π^+p pair, π^- spherical angles θ_{π^-} and φ_{π^-} and angle $\alpha_{p\pi^+}$ between planes B (composed by momenta of $p\pi^+$ pair) and A (composed by initial proton and π^-);
- invariant mass of the $\pi^+\pi^-$ pair, invariant mass of the π^-p pair, π^+ spherical angles θ_{π^+} and φ_{π^+} and angle $\alpha_{p\pi^-}$ between planes B (composed by momenta of $p\pi^-$ pair) and A (composed by initial proton and π^+).

The final particle emission angles for second set of variables is shown on Fig. 4.1. Cross sections calculated in these variables were used in physics analysis. The variables $(M_{\pi^+\pi^-}, M_{\pi^+p}, \theta_{\pi^-}, \varphi_{\pi^-}, \alpha_{\pi^+p})$ were calculated from 3-momenta of the final particles \vec{P}_{π^-} , \vec{P}_{π^+} , \vec{P}_p in the following way. Since all observables are determined in lab frame, first we transfer 3-momenta of the final particles in c.m. frame. All 3-momenta used below, if not specified otherwise, are defined in c.m. frame. $M_{\pi^+\pi^-}$, M_{π^+p} and M_{π^-p} masses were estimated as:

$$\begin{aligned} M_{\pi^+\pi^-} &= \sqrt{(P_{\pi^+} + P_{\pi^-})^2} \\ M_{\pi^+p} &= \sqrt{(P_{\pi^+} + P_p)^2} \\ M_{\pi^-p} &= \sqrt{(P_{\pi^-} + P_{p'})^2}, \end{aligned} \quad (4.1)$$

where P_i stand for the final particle four-momentum.

The angle θ_{π^-} between 3-momentum of the initial photon and final π^- in c.m. frame was calculated as:

$$\theta_{\pi^-} = \arccos \left(\frac{(\vec{P}_{\pi^-} \cdot \vec{P}_\gamma)}{|\vec{P}_{\pi^-}| |\vec{P}_\gamma|} \right) \quad (4.2)$$

φ_{π^-} angle is determined as:

$$\varphi_{\pi^-} = \arctg \left(\frac{P_{y\pi^-}}{P_{x\pi^-}} \right); \quad P_{x\pi^-} > 0; P_{y\pi^-} > 0 \quad (4.3)$$

$$\varphi_{\pi^-} = \arctg \left(\frac{P_{y\pi^-}}{P_{x\pi^-}} \right) + 2\pi; \quad P_{x\pi^-} > 0; P_{y\pi^-} < 0 \quad (4.4)$$

$$\varphi_{\pi^-} = \arctg \left(\frac{P_{y\pi^-}}{P_{x\pi^-}} \right) + \pi; \quad P_{x\pi^-} < 0; P_{y\pi^-} < 0 \quad (4.5)$$

$$\varphi_{\pi^-} = \arctg \left(\frac{P_{y\pi^-}}{P_{x\pi^-}} \right) + \pi; \quad P_{x\pi^-} < 0; P_{y\pi^-} > 0 \quad (4.6)$$

$$\varphi_{\pi^-} = \pi/2; \quad P_{x\pi^-} = 0; P_{y\pi^-} > 0 \quad (4.7)$$

$$\varphi_{\pi^-} = 3\pi/2; \quad P_{x\pi^-} = 0; P_{y\pi^-} < 0 \quad (4.8)$$

The calculation of angle $\alpha_{\pi^+ p}$, between two planes A and B (see Fig. 4.1), is more complicated. First we determine two auxiliary vectors $\vec{\gamma}$ and $\vec{\beta}$. The vector $\vec{\gamma}$ is unit vector perpendicular to the 3-momentum \vec{P}_{π^-} , directed toward vector $-\vec{n}_z$ and situated in the plane composed by virtual photon 3-momentum and 3-momentum \vec{P}_{π^-} (see Fig. 4.1). \vec{n}_z is unity vector directed along z -axis (see Fig. 4.1). The vector $\vec{\beta}$ is unit vector perpendicular to 3-momentum of π^- , directed toward 3-momentum \vec{P}_{π^+} and situated in the plane composed by π^+ and p' 3-momenta. Note that 3-momenta of π^+ , π^- , p' are in the same plane, since in CM their total 3-momentum should be equal zero. Then angle between two planes $\alpha_{\pi^+ p}$ is:

$$\alpha_{\pi^+ p} = \arccos(\vec{\gamma} \cdot \vec{\beta}) \quad (4.9)$$

\arccos function is running between zero and π . From the other hand angle between planes A and B may very between zero and 2π . To determine α angle in a range between π and 2π we looking at relative direction of the vector \vec{P}_{π^-} and vector product $\vec{\delta}$ for mentioned above auxiliary vectors $\vec{\gamma}$ and $\vec{\beta}$:

$$\vec{\delta} = \vec{\gamma} \times \vec{\beta} \quad (4.10)$$

If vector $\vec{\delta}$ was colinear to \vec{P}_{π^-} , $\alpha_{\pi^+ p}$ angle was determine from (4.9). In a case of anti collinear vectors $\vec{\delta}$ and \vec{P}_{π^-} :

$$\alpha_{\pi^+ p} = 2\pi - \arccos(\vec{\gamma} \cdot \vec{\beta}) \quad (4.11)$$

Defined above vector $\vec{\gamma}$ may be expressed through the particle 3-momenta as:

$$\begin{aligned} \vec{\gamma} &= a_\alpha(-\vec{n}_z) + b_\alpha \vec{n}_{P_{\pi^-}} \\ a_\alpha &= \sqrt{\frac{1}{1 - (\vec{n}_{P_{\pi^-}} \cdot (-\vec{n}_z))^2}} \\ b_\alpha &= -(\vec{n}_{P_{\pi^-}} \cdot (-\vec{n}_z))a_\alpha , \end{aligned} \quad (4.12)$$

where $\vec{n}_{P_{\pi^-}}$ is unit vector directed along \vec{P}_{π^-} 3-momentum (see Fig. 4.1). Taking scalar products $(\vec{\gamma} \vec{n}_{P_{\pi^-}})$ and $(\vec{\gamma} \vec{\gamma})$, it is straightforward to verify, that $\vec{\gamma}$ is unity vector perpendicular to \vec{P}_{π^-} .

Vector $\vec{\beta}$ may be obtained as:

$$\begin{aligned} \vec{\beta} &= a_\beta \vec{n}_{P_{\pi^+}} + b_\beta \vec{n}_{P_{\pi^-}} \\ a_\beta &= \sqrt{\frac{1}{1 - (\vec{n}_{P_{\pi^+}} \cdot \vec{n}_{P_{\pi^-}})^2}} \\ b_\beta &= -(\vec{n}_{P_{\pi^+}} \cdot \vec{n}_{P_{\pi^-}})a_\beta , \end{aligned} \quad (4.13)$$

where $\vec{n}_{P_{\pi^+}}$ is unit vector directed along \vec{P}_{π^+} 3-momentum. Again taking scalar products $(\vec{\beta} \vec{n}_{P_{\pi^-}})$ and $(\vec{\beta} \vec{\beta})$, it is straightforward to see, that $\vec{\beta}$ is unity vector perpendicular to π^- 3-momentum. Angle $\alpha_{\pi^+ p}$ coincides with angles between vectors $\vec{\gamma}$ and $\vec{\beta}$. So, scalar product $(\vec{\gamma} \vec{\beta})$ allows to determine angle $\alpha_{\pi^+ p}$ (4.9). The kinematics variables for other hadron

assignment for the first, second and third final particle described above, were evaluated in similar way.

For second set of kinematics variables 7-differential cross section may be written as $\frac{d\sigma}{dW dQ^2 dM_{p\pi^+} dM_{\pi^+\pi^-} d\Omega d\alpha_{p\pi^+}}$. These cross sections were calculated from the quantity of selected events collected in respective 7-differential cell and using estimated values of efficiency F as:

$$\frac{d\sigma}{dW dQ^2 dM_{p\pi^+} dM_{\pi^+\pi^-} d\Omega d\alpha_{p\pi^+}} = \frac{1}{F \cdot F_{\text{cherenkov}} \cdot R} \frac{\left(\frac{\Delta N_{full}}{Q_{tot}} - \frac{\Delta N_{empty}}{Q_{tot,empty}} \right)}{\Delta W \Delta Q^2 \Delta \tau \left(\frac{l_t D_t N_A}{q_e M_H} \right)}, \quad (4.14)$$

where ΔN_{full} and ΔN_{empty} are the numbers of events inside the 7-dimensional bin for run with hydrogen and empty target respectively, F is efficiency coming from the Monte Carlo simulations. Note, that detector blind zones and applied cuts on phase space were included to efficiency calculations. So our efficiency incorporates acceptance also. $F_{\text{cherenkov}}$ is the factor accounted for Čherenkov counter efficiency described above. Since Čherenkov efficiency was not included in Monte Carlo simulation, we estimated it separately. R is the radiative correction factor, Q_{tot} and $Q_{tot,empty}$ are the integrated Faraday Cup charges for run with hydrogen and empty target respectively, q_e is the elementary charge ($q_e = 1.610^{-19}\text{C}$), D_t is the density of hydrogen ($D_t = 0.073 \text{ gr/cm}^3$), l_t is the length of the target ($l_t = 5 \text{ cm}$), M_H is the molar density of hydrogen ($M_H = 1 \text{ gr/mol}$), N_A is Avogadro's number ($N_A = 6.0210^{23} \text{ mol}^{-1}$), ΔW and ΔQ^2 are determined by electron scattering kinematics, were bins and $\Delta\tau$ is element of the hadronic 7-dimensional phase space:

$$\Delta\tau = \Delta M_{p\pi^+} \Delta M_{\pi^+\pi^-} \Delta \cos(\theta_{\pi^-}) \Delta \varphi_{\pi^-} \Delta \alpha_{p\pi^+} \quad (4.15)$$

In single photon exchange approximation, electron scattering cross section is related to hadronic cross section $\frac{d\sigma}{dM_{p\pi^+} dM_{\pi^+\pi^-} d\Omega_{\pi^-} d\alpha_{p\pi^+}}$ as:

$$\frac{d\sigma}{dM_{p\pi^+} dM_{\pi^+\pi^-} d\Omega_{\pi^-} d\alpha_{p\pi^+}} = \frac{1}{\Gamma_v} \frac{d\sigma}{dW dQ^2 dM_{p\pi^+} dM_{\pi^+\pi^-} d\Omega_{\pi^-} d\alpha_{p\pi^+}}, \quad (4.16)$$

where Γ_v is virtual photon flux, given by

$$\Gamma_v = \frac{\alpha}{4\pi} \frac{1}{E_{beam}^2 M_p^2} \frac{W(W^2 - M_p^2)}{(1 - \varepsilon)Q^2}, \quad (4.17)$$

where α is the fine structure constant ($1/137$), M_p is the proton mass and ε is the virtual photon transverse polarization, given by

$$\varepsilon = \left(1 + 2 \left(1 + \frac{\omega^2}{Q^2} \right) \tan^2 \left(\frac{\theta_e}{2} \right) \right)^{-1}, \quad (4.18)$$

were $\omega = E_{beam} - E_{scattered \text{ electron}}$, θ_e is electron scattering angle in lab frame. W , Q^2 and θ_e were taken in the center of bin.

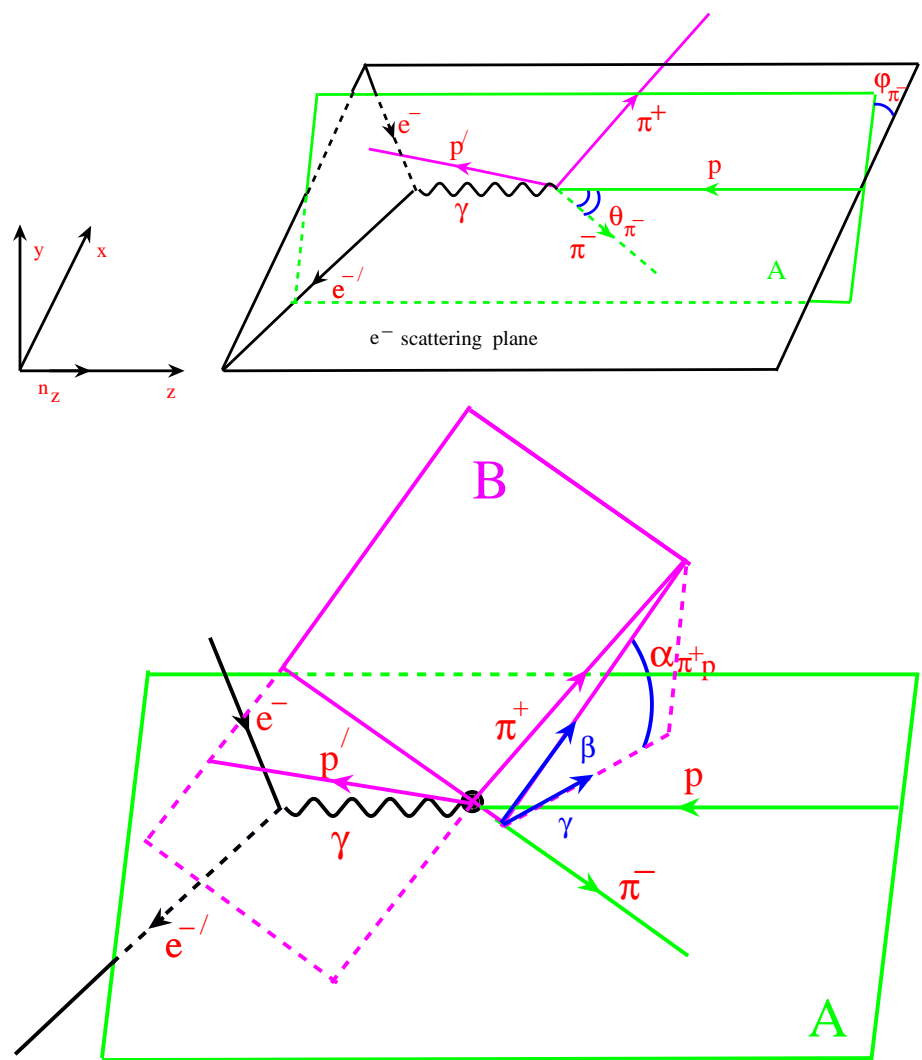


Figure 4.1: Kinematic variables for $ep \rightarrow e'p'\pi^+\pi^-$. Top plot show π^- spherical angles θ_{π^-} and φ_{π^-} while bottom plot show angle α_{π^+p} of the $p\pi^+$ pair with respect to the plane composed by initial proton and π^- .

Limited statistics (just 130,000 eventually selected $\pi^+\pi^-p$ events) does not allow as to estimate 5-differential cross section with reasonable accuracy. So, we analyzed set of single differential cross sections, obtained after integration of 5-differential cross sections over 4 variables. We obtained the following set of 1-differential 2π cross sections:

$$\begin{aligned} \frac{d\sigma}{dM_{\pi^+\pi^-}} &= \int \frac{d^5\sigma}{d^5\tau} d\tau_{\pi^+\pi^-}; & d\tau_{\pi^+\pi^-} &= dM_{\pi^-p} d\Omega_{\pi^-} d\alpha_{p\pi^+} \\ \frac{d\sigma}{dM_{\pi^+p}} &= \int \frac{d^5\sigma}{d^5\tau} d\tau_{\pi^+p}; & d\tau_{\pi^+p} &= dM_{\pi^+\pi^-} d\Omega_{\pi^+} d\alpha_{p\pi^+} \\ \frac{d\sigma}{d(-\cos\theta_{\pi^-})} &= \int \frac{d^5\sigma}{d^5\tau} d\tau_{\pi^-}; & d\tau_{\pi^-} &= dM_{\pi^+\pi^-} dM_{\pi^+p} d\varphi_{\pi^-} d\alpha_{p\pi^+} \\ \frac{d\sigma}{dM_{\pi^-p}} &= \int \frac{d^5\sigma}{d^5\tau'} d\tau_{\pi^-p}; & d\tau_{\pi^-p} &= dM_{\pi^+\pi^-} d\Omega_{\pi^+} d\alpha_{p\pi^-} \\ d^5\tau' &= dM_{\pi^-p} dM_{\pi^+\pi^-} d\Omega_{\pi^+} d\alpha_{p\pi^-} \end{aligned} \quad (4.19)$$

In actual cross section calculations the integrals in (4.19) were substituted by respective sums over 5-dimensional kinematics grid for hadronic cross sections.

The adopted hadronic binning (for variables of set 2) varied with W and Q^2 from 5 to 8 cells over single variable for invariant masses and the primary particle polar angle (for instance θ_{π^-}), from 4 to 5 for azimuthal angle φ (for instance φ_{π^-}), from 3 to 5 for angle between two planes (for instance $\alpha_{p\pi^+}$). To evaluate absolute statistical error of 5-differential hadronic cross sections we used error propagation approach:

$$\delta_{stat}(M_{p\pi^+}, M_{\pi^+\pi^-}, \theta_{\pi^-}, \varphi_{\pi^-}, \alpha_{p\pi^+}) = \frac{1}{F \cdot F_{cherenkov} \cdot R} \frac{1}{\Gamma_v} \frac{1}{\Delta W \Delta Q^2 \Delta \tau} \sqrt{\left(\frac{\Delta N_{full}}{Q_{tot}^2} + \frac{\Delta N_{empty}}{Q_{tot,empty}^2} \right)} \quad (4.20)$$

Another source of statistical fluctuations is connected to the limited statistics in the Monte Carlo: from formula (4.14), it is clear that the error in the knowledge of the efficiency F is affecting the cross section value. Here we have to spend a few words about the statistical error in the simulation; the definition of efficiency factor F is simple:

$$F = \frac{N_{rec}}{N_{gen}} \quad (4.21)$$

It turns out [39] that the absolute statistical error on F is given by

$$\delta(F) = \sqrt{\frac{N_{rec}(N_{gen} - N_{rec})}{N_{gen}^3}} \quad (4.22)$$

The error on the cross section due to the limited Monte Carlo statistic is given by

$$\delta_{stat,MC} = \frac{d\sigma}{dM_{p\pi^+} dM_{\pi^+\pi^-} d\Omega d\alpha_{p\pi^+}} \left(\frac{\delta(F)}{F} \right) \quad (4.23)$$

Finally we combined quadratically the two statistical errors coming from fluctuation in the data and from the Monte Carlo, so total absolute statistical error is given by

$$\delta_{stat,tot} = \sqrt{\delta_{stat,MC}^2 + \delta_{stat}^2} \quad (4.24)$$

4.2 Efficiency evaluation

We use the Monte Carlo event generator of Genova group (M. Ripani, E. Golovach et al.). This event generator is capable to simulate event distribution for major meson photo and electro production channels in N^* excitation region. To calculate efficiency for detection of $\pi^+\pi^-p$ final state we simulated 2π and 3π electroproduction processes. The final states with more than 2 pions were needed to account for multi pion background in selection of 2π events. In simulation we apply the similar cuts to isolate 2π events as for the data. So, in this way we account in calculated efficiency for contamination of selected data sample by events with number of pions more than 2. We described $\pi^+\pi^-p$ final state in event generator as incoherent sum of $\pi^-\Delta^{++}$, $\pi^+\Delta^0$ isobar channels, while remaining mechanisms were parametrized as 3-body phase space. Other 2π production mechanisms at $W < 1.6$ GeV have small contributions and were taken out. Photoproduction cross sections for various mechanisms contributed to the $\pi^+\pi^-p$ final state were taken from [44]. Q^2 evolution for all cross sections in event generator was described by dipole fit. The calculated event distributions were further radiated, using Mo and Tsai approach to simulate radiative effects [40].

To reproduce measured event distributions at $W < 1.4$ GeV we substitute isobar channel and 3-body phase space cross sections of Genova event generator by cross sections evaluated within the framework of isobar model JM03 [41–43].

Generated events have gone through the fiducial cuts, GSIM, GPP, RECSIS and the analysis cuts (except cuts on number of photoelectrons, Čerenkov counter efficiency were calculated separately as described above). Around 4 millions events were reconstructed (40 times more than data events). Quality of data description you can see from Fig. 4.2 and Fig. 4.3. Left plot of Fig. 4.2 represent W distribution, while right plot Q^2 distribution. Fig. 4.3 show distributions hadronic variables distributions for $W = 1.4125$ GeV, $Q^2 = 0.525$ GeV 2 . Red curves on both figures represent Monte Carlo, black - data.

We have reasonable description for measured W and Q^2 event distributions. In event distributions over the final hadronic state kinematics variables we succeeded to describe $\pi^+\pi^-$ mass distributions, φ_{π^-} angular distributions (see Fig. 4.3). As it will be shown at the end of this section these are the final state hadronic variables for which we have most rapid variation of efficiency. So, successful simulation of event distributions over these variables is critical for reliable efficiency evaluation.

As it follows from Fig. 4.3 we still have some discrepancies in description of π^+p mass distributions and π^- angular distribution. However relatively smoother variations of efficiency as a function of these variables in the areas corresponded to discrepancies (Fig. 4.4 bottom row), make affordable to use achieved description of distribution for efficiency evaluation.

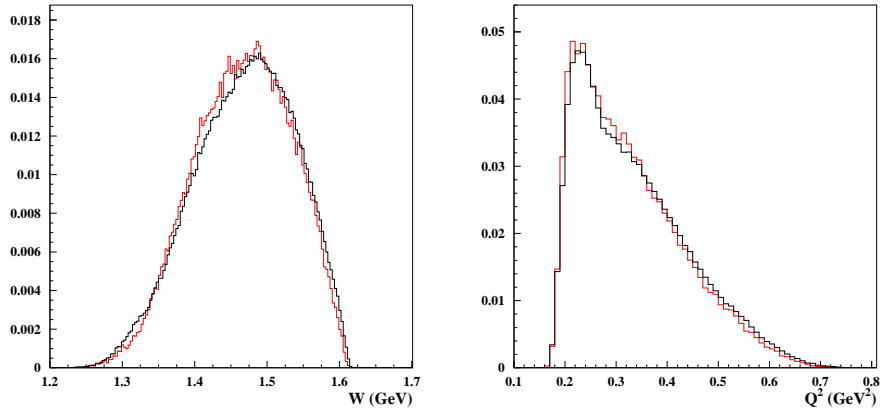


Figure 4.2: W (left plot) and Q^2 (right plot) distributions. Black curves represents data, red curves simulation.

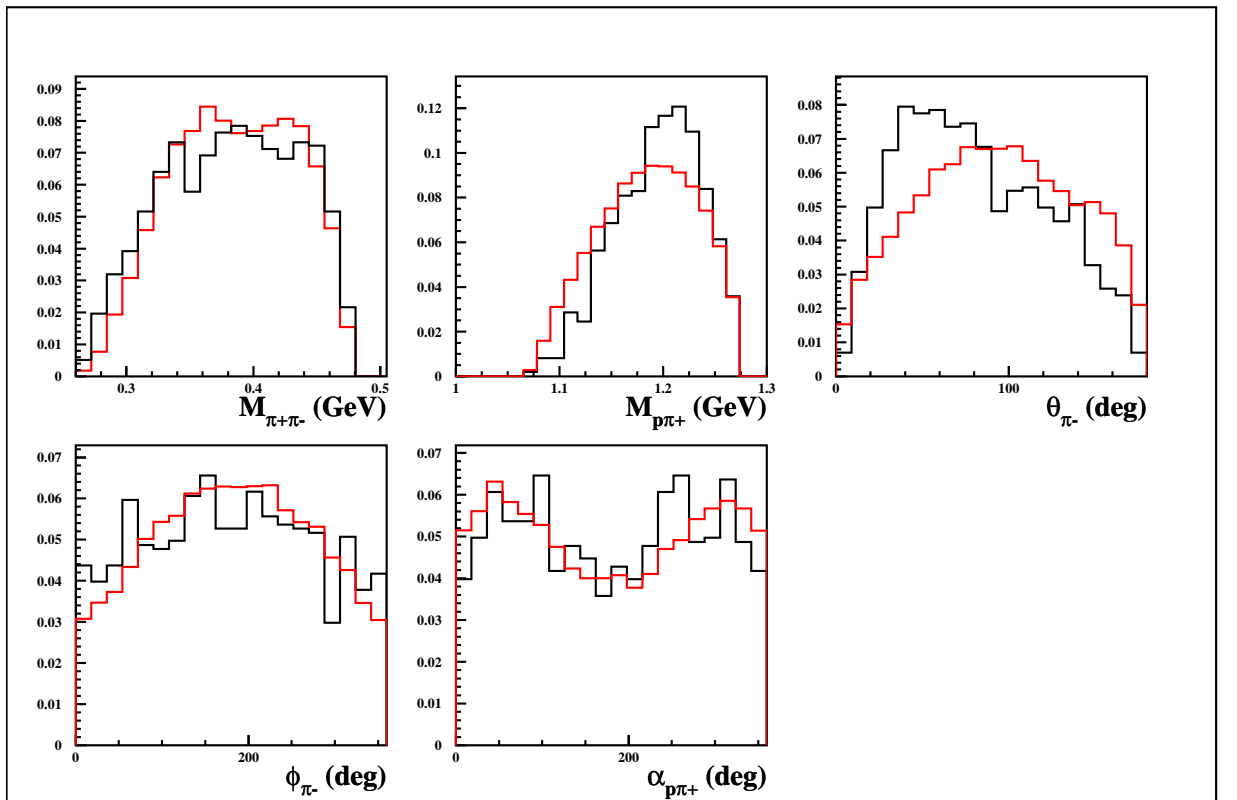


Figure 4.3: Comparison between measured and simulated event distributions for various final state variables. Black curves represents data, red curves simulation. ($W = 1.4125 \text{ GeV}$, $Q^2 = 0.525 \text{ GeV}^2$).

Probability for $\pi^+\pi^-p$ events to be detected by CLAS actually depend from 4-momenta and type of all final particles. So, we estimated efficiency separately in each 7-differential cell composed by variables ΔW , ΔQ^2 , ΔM_{π^+p} , $\Delta M_{\pi^+\pi^-}$, $\Delta\theta_{\pi^-}$, $\Delta\varphi_{\pi^-}$, $\Delta\alpha_{\pi^+p}$. To determine efficiency first we generated events with multi pion emission (number of the final pions > 1) using event generator, described in section 4.2. Generated events have gone through the fiducial cuts, GSIM, GPP, RECSIS and the analysis cuts (except cuts on number of photoelectrons, Čerenkov counter efficiency were calculated separately as described above). Selected in this way generated $\pi^+\pi^-p$ events will be referred as reconstructed 2π events.

In each 7-D cell we calculate efficiency as number of reconstructed events divided to number of generated events. In Fig. 4.4 we show distributions over all hadronic variables, used for description of the final hadronic state, for generated events (top row), reconstructed events (middle row) and dependencies of CLAS efficiency from these variable. Efficiencies and event distributions we integrated over all other variables. Efficiency exhibit strong dependence from $M_{\pi^+\pi^-}$, M_{π^+p} invariant masses and α_{π^+p} angle. So, we required most realistic description by event generator for invariant masses and α_{π^+p} angular distributions. Requirement for description of other variables by event generator were less demanded.

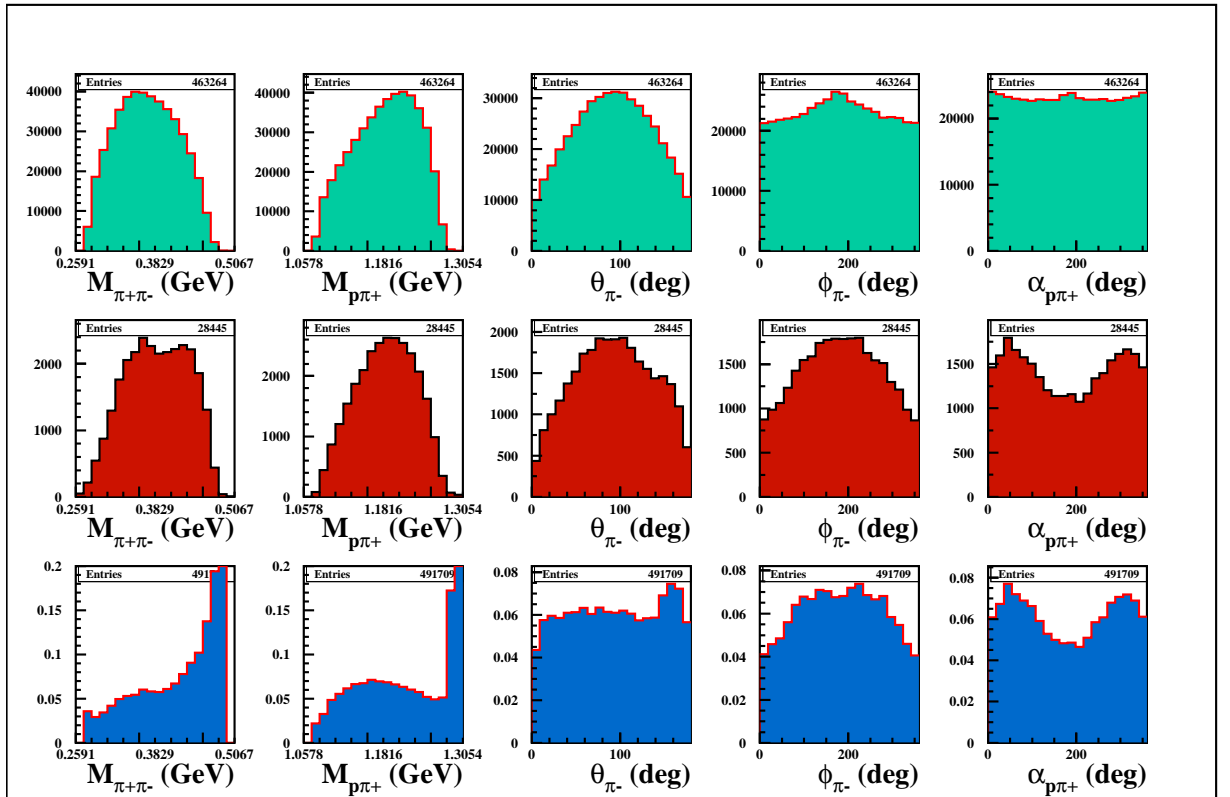


Figure 4.4: Generated events (top green plots), reconstructed events (middle red plots) and efficiency (bottom blue plots) as function of 5 hadronic variables. W and Q^2 were fixed at $Q^2 = 0.525$ GeV 2 , $W = 1.4125$ GeV.

4.3 Interpolation of cross sections to the kinematics areas corresponded to zero efficiency.

In data analysis we found kinematics areas for which we have simulated events, while quantity of accepted events was equal to zero. Such situation represent an indication for zero CLAS detector acceptance in these kinematics regions. We need to account for contribution of such blinded area to the integrals (4.19) for single differential cross sections.

To estimate the contributions to the cross sections from CLAS blinded areas we used two step procedure. First we evaluated such contributions based on cross section description in modified Genova event generator, described in section 4.2. To get 5-differential virtual photon cross sections in blind areas $\frac{d\sigma}{dM_{p\pi^+}dM_{\pi^+\pi^-}d\Omega_{\pi^-}d\alpha_{p\pi^+}}$, we used as input: number of measured events in current (W, Q^2) bin integrated over all hadronic variables for the $\pi^+\pi^-p$ final state $N_{data,int}$; the number of these events estimated from event generator $N_{generated,int}$; number of generated events in 7-D cell $(W, Q^2, M_{p\pi^+}, \Omega_{\pi^-}, \alpha_{\pi^+,p})$ $N_{generated}^{7D}$. Using event generator as a guide, we estimated quantity of events in blinded cell as $\frac{N_{data,int}}{N_{generated,int}} N_{generated}^{7D}$. So, 5-differential cross sections in blinded area were calculated as:

$$\frac{d\sigma}{dM_{p\pi^+}dM_{\pi^+\pi^-}d\Omega d\alpha_{p\pi^+}} = \frac{1}{R\Gamma_v} \frac{\left(\frac{1}{eff_{int}} \frac{N_{data,int}}{N_{generated,int}} N_{generated}^{7D}\right) / Q_{tot}}{\Delta W \Delta Q^2 \Delta \tau \left(\frac{l_t D_t N_A}{q_e M_H}\right)}, \quad (4.25)$$

where eff_{int} is integral efficiency inside 5-D bin, Q_{tot} is the integrated Faraday Cup charge. Other variables described in (4.14).

After integration of measured (4.14) and interpolated into the blinded areas (4.25) 5-differential cross sections we got single differential cross sections (4.19). Obtained single differential cross sections were fitted within the framework of recent version of isobar model, developed in collaboration between JLAB and MSU (JM05) [45], for description of $\pi^+\pi^-p$ exclusive channel. In each (W, Q^2) bin covered by measurements we analyzed $\pi^+\pi^-$, π^+p , π^-p invariant masses and π^- angular distributions. Phenomenological parameters of JM05 were extracted from the data fit. Achieved quality of data description may be seen on Appendix A. Reasonable description of all observables measured in our experiment within the framework of JM05 allow us to use this model for more realistic interpolation of measured cross sections into blinded zones.

Rotational invariance of reaction amplitudes requires the following dependence of 5-differential cross sections from the angle φ_{π^-} :

$$\frac{d^5\sigma}{d^5\tau} = A + B \cos 2\varphi_{\pi^-} + C \cos \varphi_{\pi^-} \quad (4.26)$$

in the case of unpolarized beam and target. So in the limit 100% detector efficiency we may get 4-differential cross section summing up events over φ_{π^-} angle

$$\frac{d^4\sigma}{d^4\tau} = \sum_{j_{\pi^-}} \frac{1}{\Gamma_v} \frac{d\sigma}{dW dQ^2 dM_{p\pi^+} dM_{\pi^+\pi^-} d\Omega_{\pi^-} d\alpha_{p\pi^+}} \Delta\varphi_{\pi_j^-} = A \cdot 2\pi, \quad (4.27)$$

where A is φ -independent part of 5-differential cross section is determined by (4.14). Further integrating $A \cdot 2\pi$ over 4-variables, we get 1-differential cross sections (4.19).

However, we have areas with zero CLAS detector efficiencies. We take into account contributions from such areas to the cross section in the following way. 5-differential cross sections in blinded areas were calculated from the data on cross sections in the populated 5-differential cell, assuming (4.26) for φ_{π^-} dependence. The ratio $B/A = R_1$ and $C/A = R_2$ were taken from JM05 [45]. Coefficient A were determined from the measured values of integrated over φ_{π^-} angle 5-differential cross sections:

$$\begin{aligned} \sum_{\Delta\varphi_{\pi^-}} \frac{d\sigma_{measured}}{dM_{p\pi^+} dM_{\pi^+\pi^-} d\Omega d\alpha_{p\pi^+}} \Delta\varphi = \\ A(2\pi - \Delta\tilde{\varphi}) - R_1 A \int_{\Delta\tilde{\varphi}} \cos(2\varphi_{\pi^-}) d\varphi_{\pi^-} \\ - R_2 A \int_{\Delta\tilde{\varphi}} \cos(\varphi_{\pi^-}) d\varphi_{\pi^-}, \end{aligned} \quad (4.28)$$

where $\Delta\tilde{\varphi}$ are area over φ_{π^-} angle with zero efficiency. Using determined in this way values of A , B and C in (4.26) we interpolated measured 5-differential cross sections in to the cells with zero acceptance.

Developed approach allowed us to calculate cross sections in any populated 4-differential cell composed by variables ($M_{\pi^+\pi^-}$, M_{π^+p} , θ_{π^-} , α_{π^+p}). The comparison between single differential 2π cross sections (4.19), obtained interpolating cross section into blinded area with event generator and using JM05 [45] are shown on Fig. 4.5. The difference between two ways to account for contribution from blinded areas to cross section does not expires 3%. We considered this difference as systematic uncertainty of cross section, coming from interpolation of cross sections into blind areas.

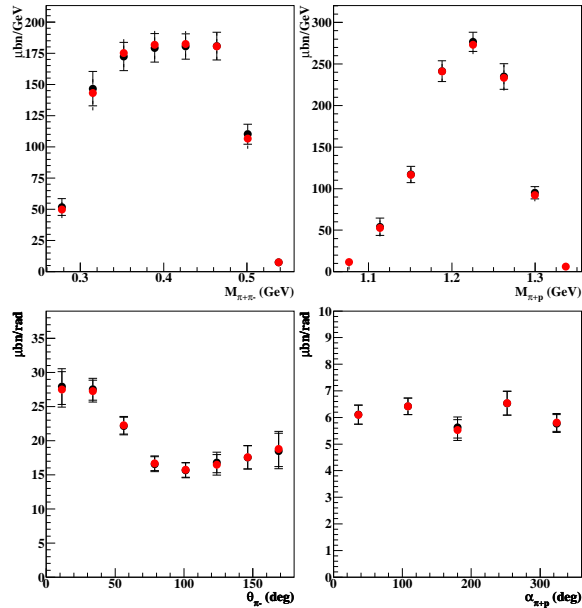


Figure 4.5: Comparison between single differential cross sections, obtained interpolating cross sections into blinded area with event generator (red points) and using JM05 [45] (black points). ($W = 1.4625$ GeV, $Q^2 = 0.275$ GeV 2).

Chapter 5

Radiative corrections

To estimate influence of radiative correction effects we simulated 2π events using Genova event generator with included and excluded radiative effects. Radiative correction factor R in (4.14) was determined as:

$$R = \frac{N_{rad}^{2D}}{N_{norad}^{2D}}, \quad (5.1)$$

where N_{rad}^{2D} and N_{norad}^{2D} are numbers of generated events in each (W, Q^2) bin with on/off radiative effects. In each (W, Q^2) bin covered by measurements we generated by events with switched on/off radiative effects. We assume the factor R is independent from final hadron kinematics variables. This factor is plotted as function of W on Fig. 5.1, various curves on this plot represent various Q^2 bins. In [47] for simulation of radiative effects in double pion electroproduction well known Mo and Tsai procedure [40] is used. In this approach soft part is evaluated explicitly, while hard part calculation in any possible approach inevitably rely on knowledge of hadronic tensor for studied exclusive channel [48]. Genova event generator used Mo and Tsai procedure, which assume "inclusive" hadronic tensor for hard radiative part. Applicability of such approximation for hard part of radiative effects was subject of special attention.

For $ep \rightarrow e'p'\pi^+\pi^-\gamma$ event we apply cut over π^- missing mass, discussed in section 3.7. In this way we restricted hardness of emitted photons. Then we evaluated the contribution of soft and hard effects to radiative factor R within the framework of Mo and Tsai approach. We found the contribution from hard part is varied from 30% to 50%. Therefore even assuming 100% error in evaluation of the hard part for radiative correction, we end-up with few % of uncertainty of 2π cross section for the values of radiative factor R shown on Fig. 5.1.

2π cross sections (4.19) used for analysis represent integrated over 4 variables 5-differential cross section. This integration considerably reduced influence of the final hadron kinematics variables on radiative correction factors for analyzed single differential cross sections. So, "inclusive" Mo and Tsai procedure looks more applicable to partially integrated 1-differential cross section than in a case of non-integrated cross section for instance single pion data.

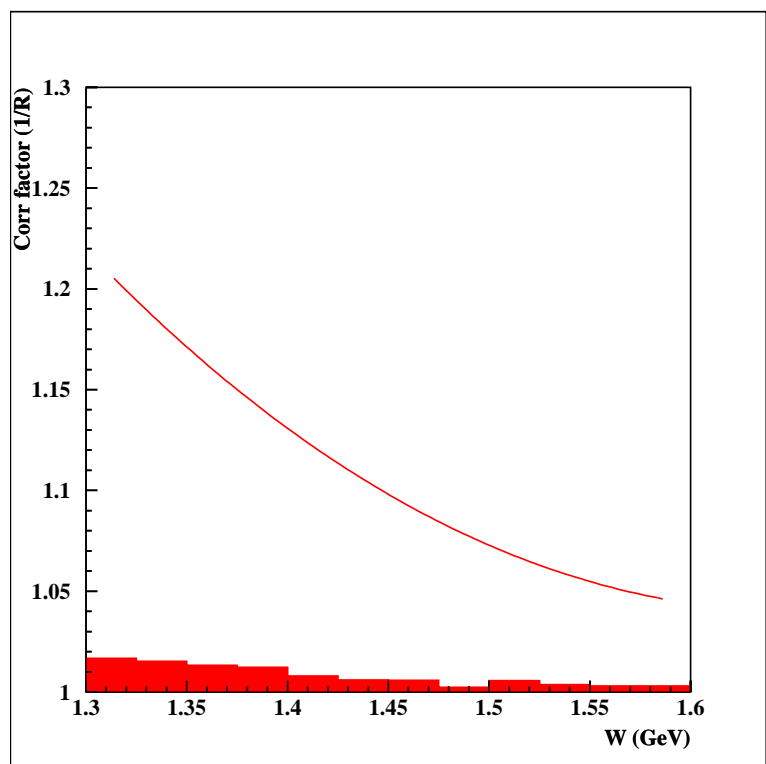


Figure 5.1: Radiative correction factor as function of W , various curves represent various Q^2 bins.

Chapter 6

Correction for binning effects

Due to the finite size of data bins the obtained values for the cross section can be distorted due to the fact that the measured value is the weighed average of the cross sections over the whole bin. For instance, if there is a sharp peak in the middle of a bin, then the average value of the cross section in that bin will always be less (or equal) than the value at the peak. Any non-linear behavior of the cross section will likely result in an offset of the measured value. There are two ways to deal with this issue. Either one corrects the value for the kinematic quantities associated with the bin, rather than using the central value; or one calculates the correction to the cross section in the center of the bin. In this analysis the second method was chosen, because the first one does not resolve the case with the sharp peak in the center of the bin which was mentioned above. The ratio of the value at the center of the bin to the average value was considered as a multiplicative correction factor, and the corrected cross section was found as:

$$\sigma_{corr} = \sigma_{uncorr} \times C_{bin}, \quad (6.1)$$

$$C_{bin} = \frac{\sigma_{model,cntr}}{\sigma_{model,avg}}, \quad (6.2)$$

where σ_{uncorr} is the experimental cross section value before binning corrections, $\sigma_{model,cntr}$ is the cross section from the model in the center of the data bin, and $\sigma_{model,avg}$ is the cross section from the model averaged over data bin. Model cross section were calculated using quadratic extrapolation of experimental data.

In the first step the correction factors were calculated for all single differential cross sections. Then the corrected cross sections were integrated and corrected to W dependence inside the bins. Finally we take in to account Q^2 dependences of cross section. Fig. 6.1 show Q^2 and W distributions of the final correction factor.

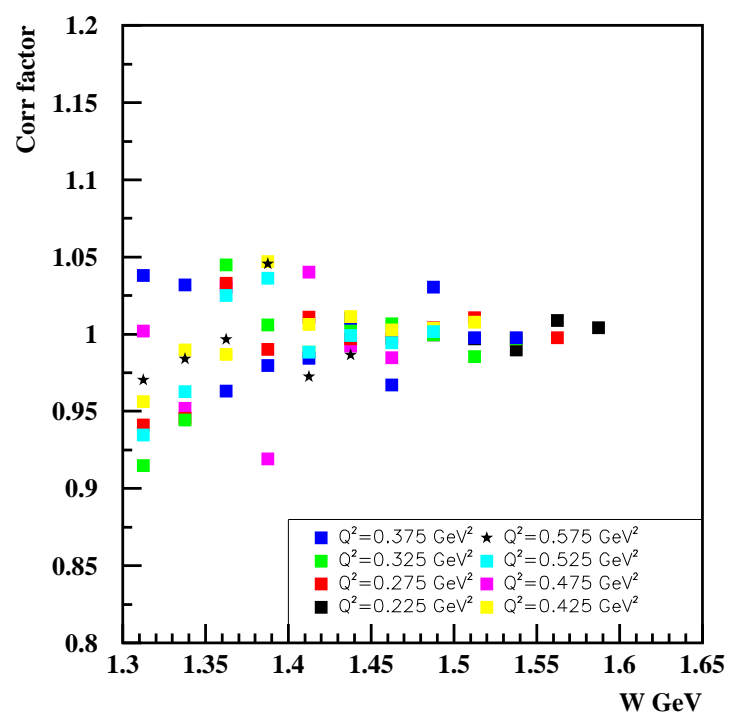


Figure 6.1: Binning correcton factor as function of W .

Chapter 7

Systematic errors

7.1 Integration

To estimate the systematic error due to the integration of finite bins, we performed the analysis using three different sets of hadronic variables previously discussed. We calculated completely integrated 2π cross sections integrating over 3 kinematic grids. In ideal case we should have the same values of integrated 2π cross sections for all 3 grids. Therefore difference between integrated cross sections we treated as systematic uncertainty due to integration procedure. This systematic effect is typically of the order of 5%. This systematic error was computed and tabulated for each W and Q^2 bin.

7.2 Fiducial cuts

To estimate the systematic error due to the various set of hadron (π^+ and proton) fiducial cuts, we performed analysis using the shifted cuts, shown by yellow curves on Fig. 7.1. Difference between cross sections obtained with these hadron fiducial cuts, was used to evaluated systematic uncertainty due to choice of fiducial cut.

7.3 Missing mass cut

We used a missing mass cut around the π^- peak to select double pion events. This cut causes loss of some events. Uncertainties due to such losses were estimated by using "radiated events in the Monte Carlo simulations for the acceptance calculations. The error associated with the missing mass cut was estimated by calculating the difference in the cross sections with two different missing mass cut applied both on the real data and Monte Carlo data sample.

Although the standard missing mass cut in the data is $-0.02 < M_{\pi^-X}^2 < 0.06 \text{ GeV}^2$, we used other cut to estimate the systematic uncertainty due to missing mass cut. These cut was more narrow than the standard cut $0.0 < M_{\pi^-X}^2 < 0.04 \text{ GeV}^2$. The absolute value of the difference between the cross sections calculated with two cuts at fixed Q^2 and W was

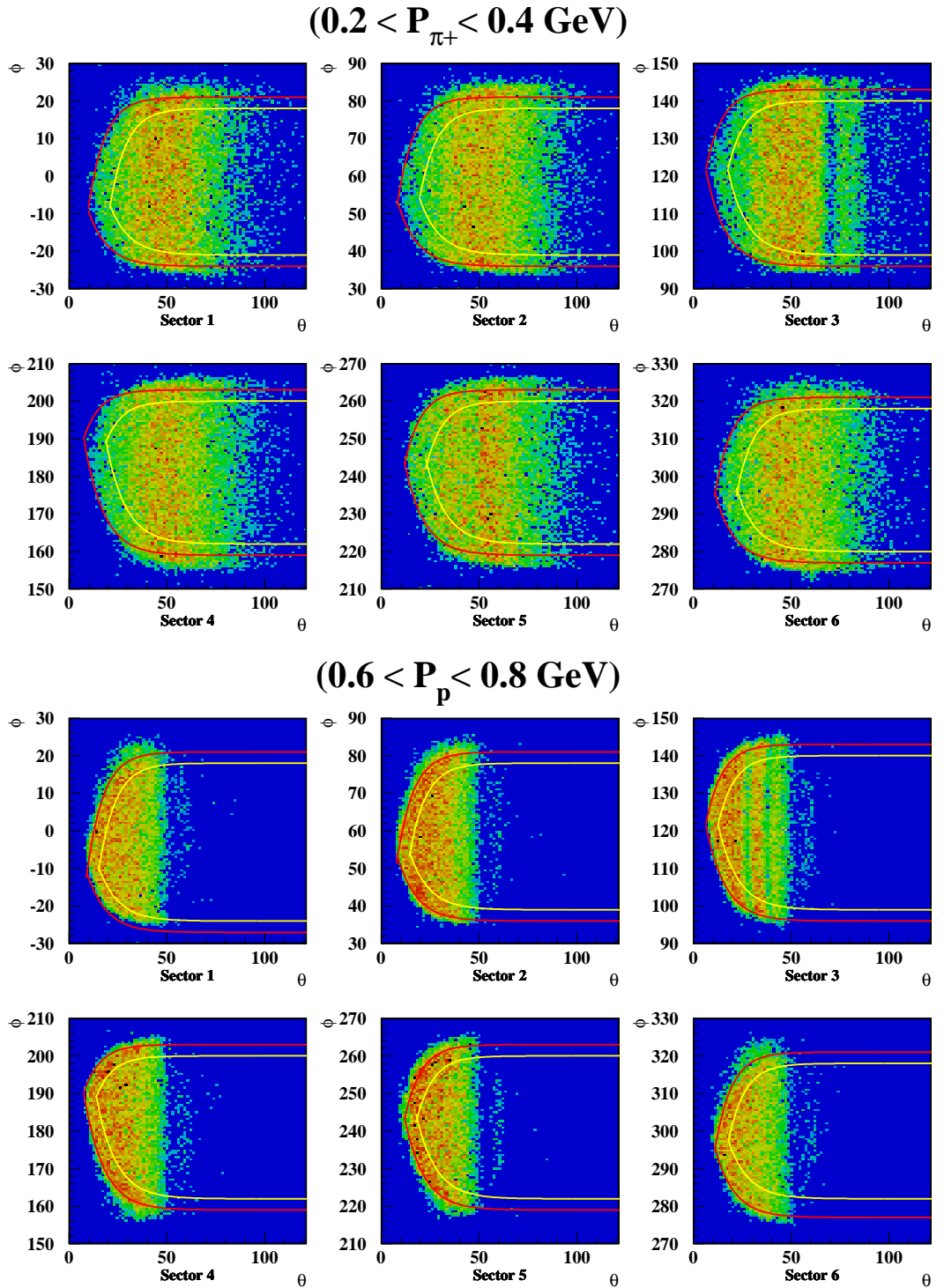


Figure 7.1: Plot of angles φ versus θ for π^+ (top) and protons (bottom) in the 6 CLAS sectors, with π^+ momentum between 0.2 and 0.4 GeV and protons momentum between 0.6 and 0.8 GeV. The red curves are applied fiducial cuts used for cross section calculation, while yellow curves are shifted fiducial cuts for systematic uncertainty evaluation.

considered as the systematic uncertainty. The errors due to missing mass cuts are about 2% - 3% of the measured cross sections.

7.4 Errors due to normalization, electron identification and electron detection efficiency

One of the main source of systematic errors in this experiment is the uncertainty in the normalization. This can arise from miscalibrations of the Faraday cup, target density instabilities, and errors in determining the target length and its temperature, DAQ live-time and other factors. However, the presence of the elastic events in the data set allows us to check the normalization of the cross sections by comparing the elastic cross sections to the world data. This way we can combine the normalization, electron detection, electron tracking and electron identification errors into one global uncertainty factor. In Fig. 7.2 the ratio of the elastic cross section to the Bosted parametrization [46] of the elastic cross sections is shown. The parametrization cross section are also "radiated", while the elastic cross sections from the CLAS data are not corrected for radiative effects. One can see most of all the points positioned within the blue lines, indicating 5% offsets. This procedure allows us to assign a 4% global uncertainty due to the normalization, electron identification and electron efficiency.

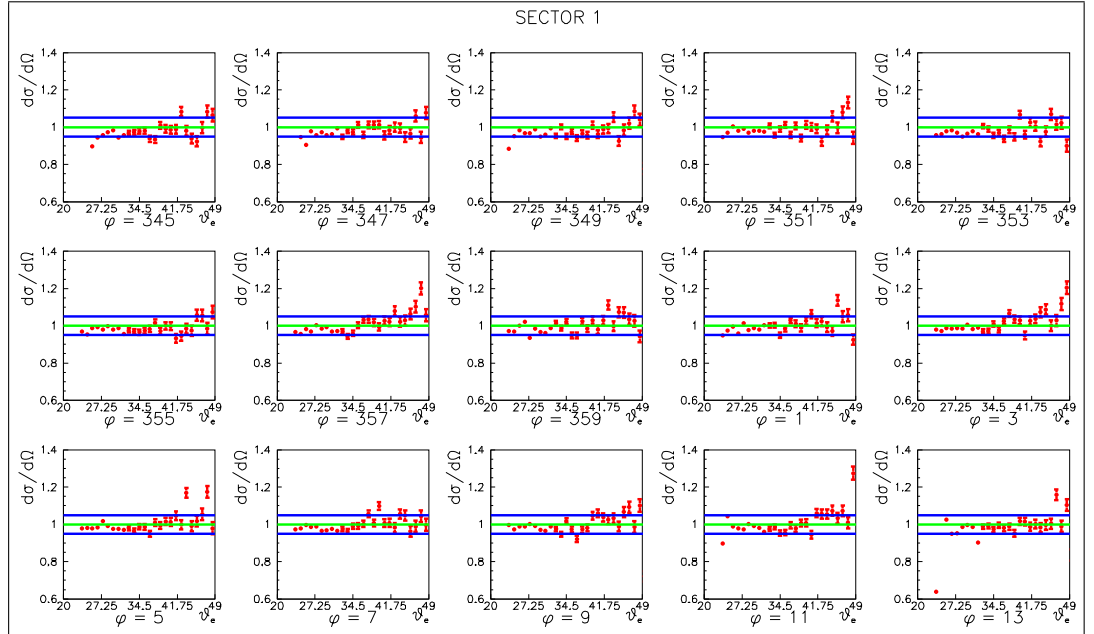


Figure 7.2: Ratio of the elastic cross section to the Bosted parametrization [46], plotted versus θ_e angle of the electron for sector 1. Various plots represent various electron angles φ_e . Green lines correspond to unity, blue lines indicate a 5% deviation from the parametrization.

7.5 Systematic errors summary

From our studies, it turns out that the biggest sources of systematic error in particular W and Q^2 bins are integration over hadronic variables, normalization, electron identification and electron detection efficiency. Although some of the systematic errors discussed may be partly correlated and therefore our final estimate is likely to be a conservative one, we summed up all the errors above reported in quadrature to obtain the total systematic error: this quantity is reported as shadowed area in the total cross section plots Fig. 7.3.

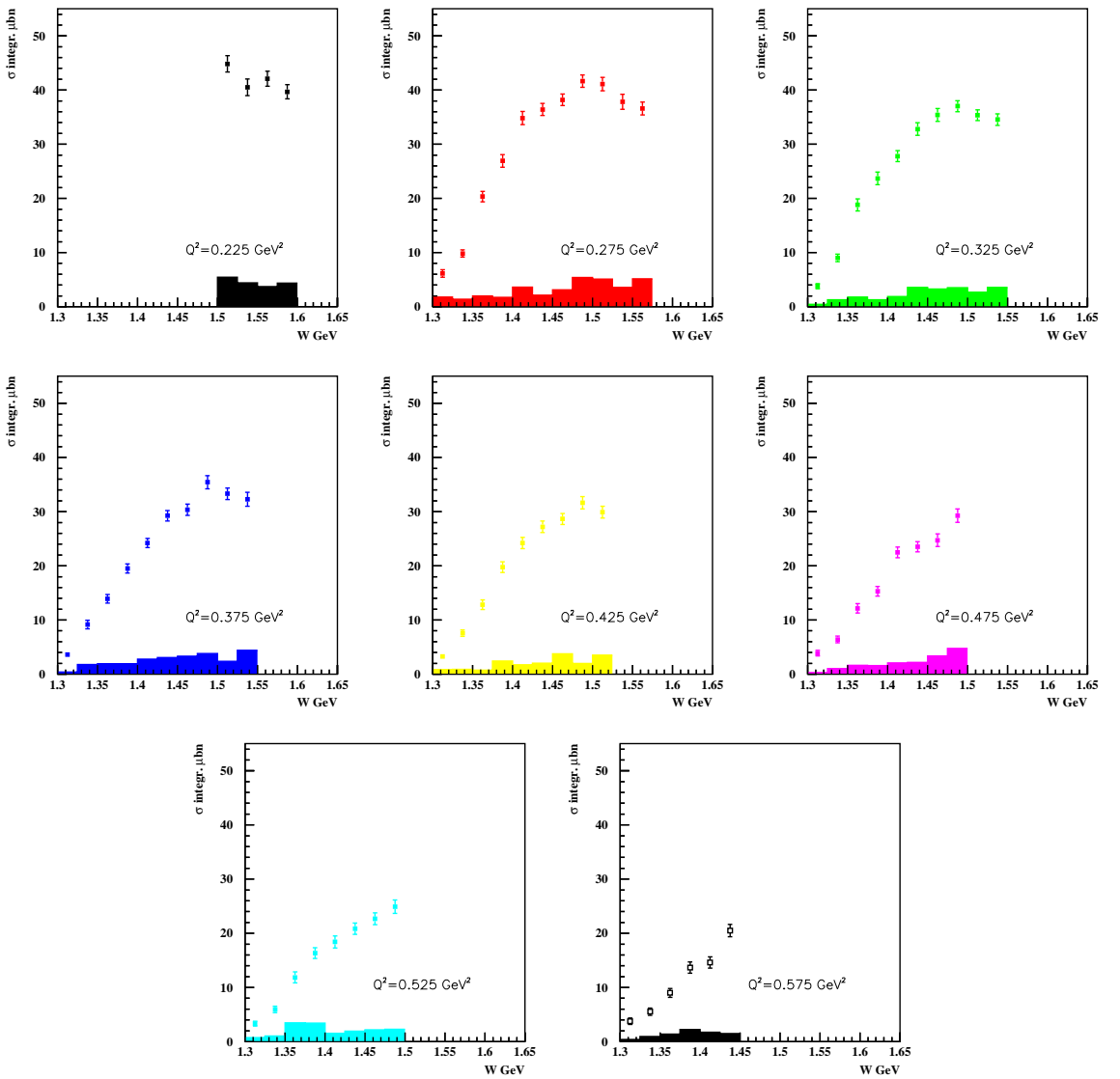


Figure 7.3: W dependence of 2π cross section for various Q^2 . Shadowed areas represent systematical uncertainties.

Chapter 8

Conclusions

- Complete set of single differential $\gamma_v p \rightarrow p\pi^+\pi^-$ cross sections was determined from CLAS data. The data set consist of $\pi^+\pi^-$, π^+p , π^-p mass and π^-, π^+ , proton angular distributions collected in each (W, Q^2) -bin covered by measurements. Cross sections were determined in W area from 1.3 GeV to 1.6 GeV and for photon virtualities from 0.2 GeV^2 to 0.6 GeV^2 . Bin size for W was 25 MeV and 0.05 GeV^2 for Q^2 .
- Special procedure developed to fill areas of zero efficiency in 5-differential phase space corresponded to $p\pi^+\pi^-$ final state. This procedure used general φ -dependence of production amplitudes based on rotational invariance, while specific dynamical features were accounted by ratio of coefficients in front of $\cos(2\varphi)$ and $\cos(\varphi)$ over coefficient in φ -independent part, estimated within the framework of JM05 isobar model.
- Evaluation of systematic uncertainties showed that the biggest source of systematic error are integration over hadronic variables, normalization, electron identification and electron detection efficiency.
- Reasonable description of all measured $\gamma_v p \rightarrow p\pi^+\pi^-$ single differential cross sections was achieved within the framework of JM05 model in entire kinematics range, covered by reported measurements. Our data confirmed sizable contribution from direct 2π production mechanisms, previously observed in analysis of the 2π data at $Q^2 > 0.5 \text{ GeV}^2$. We observed manifestation of the FSI effect through possible π^-p rescattering at $W < 1.45 \text{ GeV}$, which disappear at higher W . The data obtained open up promising opportunity to study Q^2 -evolution of $P_{11}(1440)$ and $D_{13}(1520)$ electro-coupling at low Q^2 , particularly sensitive to the meson cloud contributions as well as access axial $\pi p \Delta$ transition form factor.

Appendix A: Measured cross section and fit within a framework of JM05

$$Q^2 = 0.225 \text{ GeV}^2, W = 1.5125 \text{ GeV}$$

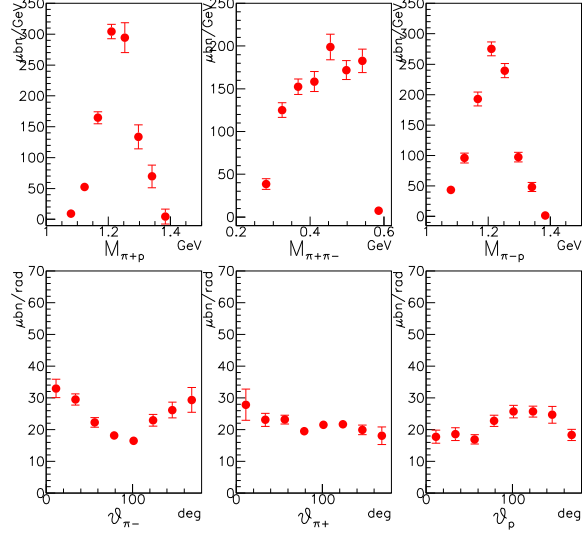


Figure A.1: 2π cross sections as function of hadronic variables.

$$Q^2 = 0.225 \text{ GeV}^2, W = 1.5375 \text{ GeV}$$

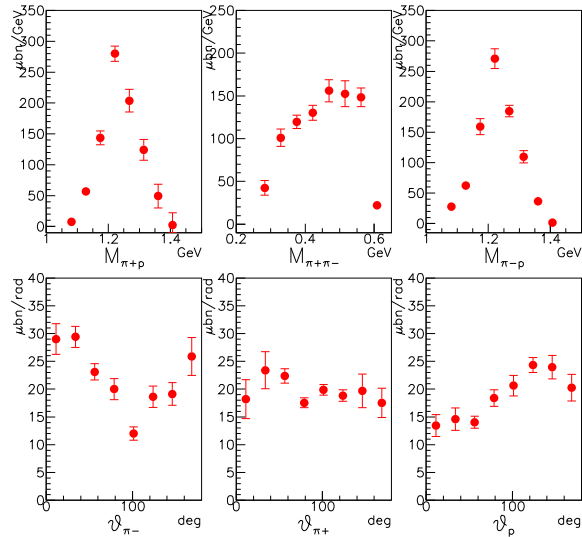


Figure A.2: 2π cross sections as function of hadronic variables.

$$Q^2 = 0.225 \text{ GeV}^2, W = 1.5625 \text{ GeV}$$

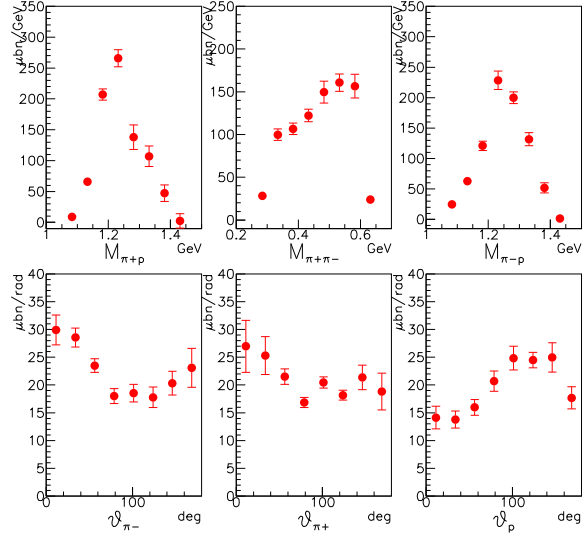


Figure A.3: 2π cross sections as function of hadronic variables.

$$Q^2 = 0.225 \text{ GeV}^2, W = 1.5875 \text{ GeV}$$

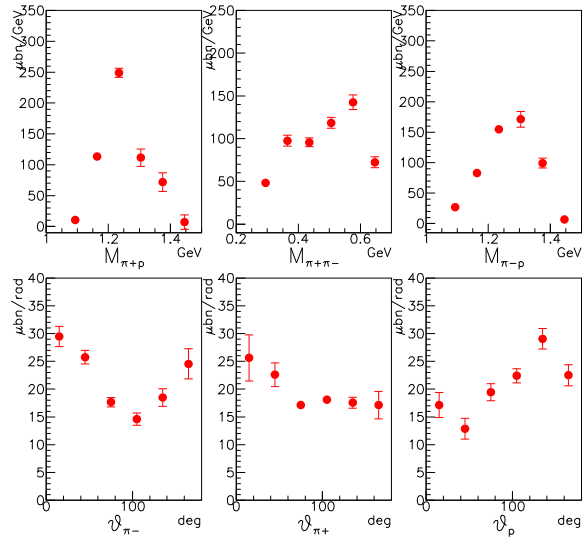


Figure A.4: 2π cross sections as function of hadronic variables.

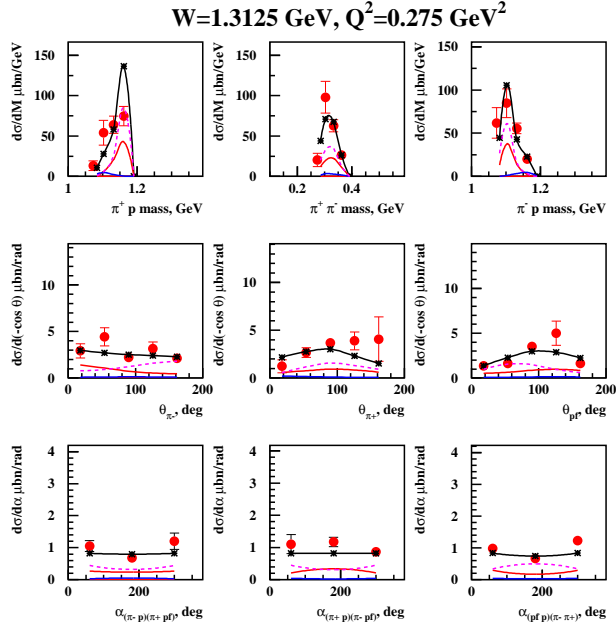


Figure A.5: 2π cross sections as function of hadronic variables fitted within a framework of JM05: black curve - total 2π cross section, red - $\pi^- \Delta^{++}$ channel, blue - $\pi^+ \Delta^0$, dashed magenta - direct 2π production.

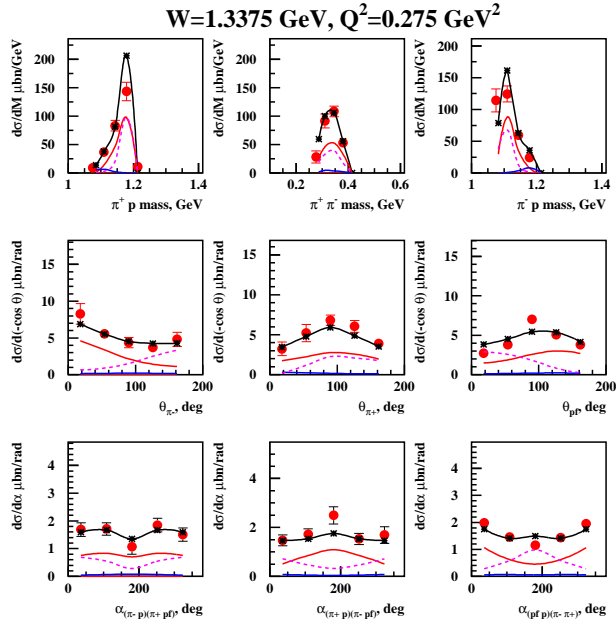


Figure A.6: 2π cross sections as function of hadronic variables fitted within a framework of JM05: black curve - total 2π cross section, red - $\pi^- \Delta^{++}$ channel, blue - $\pi^+ \Delta^0$, dashed magenta - direct 2π production.

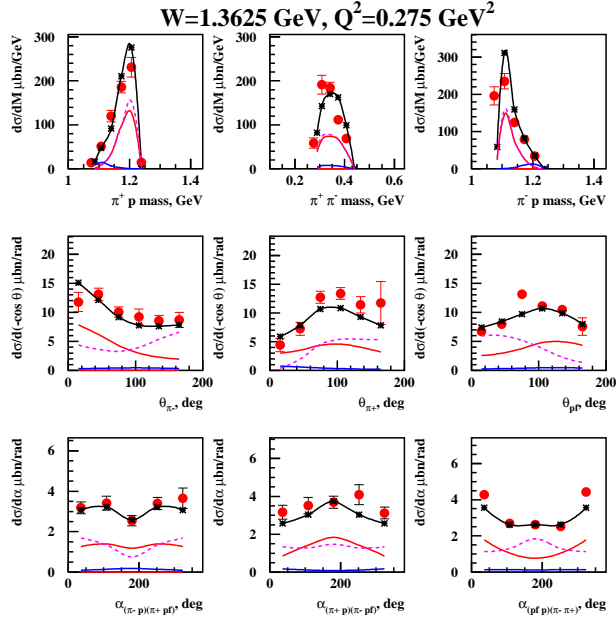


Figure A.7: 2π cross sections as function of hadronic variables fitted within a framework of JM05: black curve - total 2π cross section, red - $\pi^-\Delta^{++}$ channel, blue - $\pi^+\Delta^0$, dashed magenta - direct 2π production.

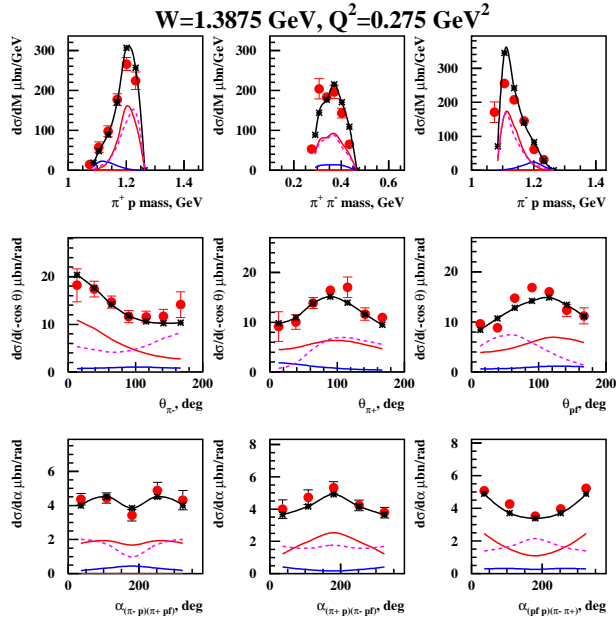


Figure A.8: 2π cross sections as function of hadronic variables fitted within a framework of JM05: black curve - total 2π cross section, red - $\pi^-\Delta^{++}$ channel, blue - $\pi^+\Delta^0$, dashed magenta - direct 2π production.

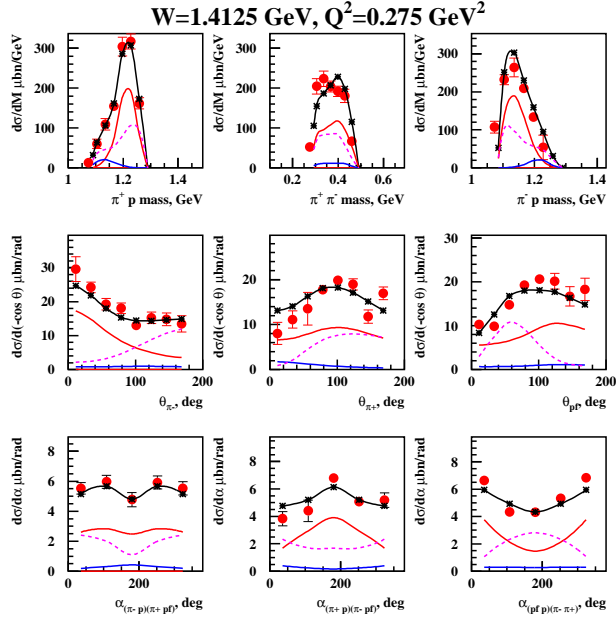


Figure A.9: 2π cross sections as function of hadronic variables fitted within a framework of JM05: black curve - total 2π cross section, red - $\pi^- \Delta^{++}$ channel, blue - $\pi^+ \Delta^0$, dashed magenta - direct 2π production.

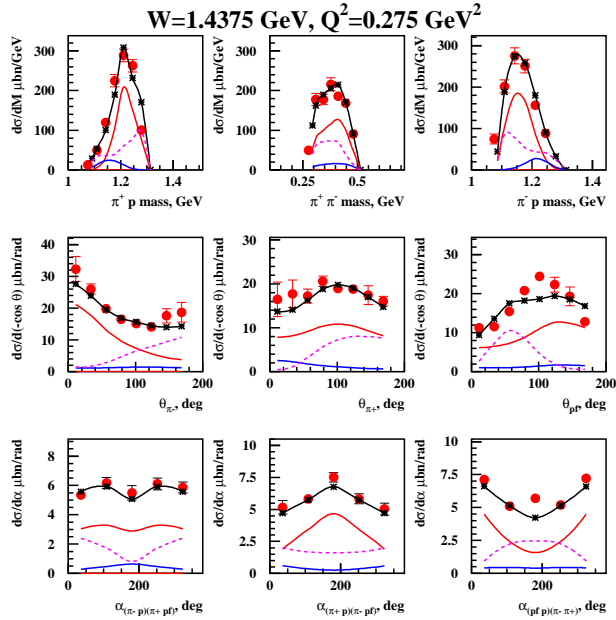


Figure A.10: 2π cross sections as function of hadronic variables fitted within a framework of JM05: black curve - total 2π cross section, red - $\pi^- \Delta^{++}$ channel, blue - $\pi^+ \Delta^0$, dashed magenta - direct 2π production.

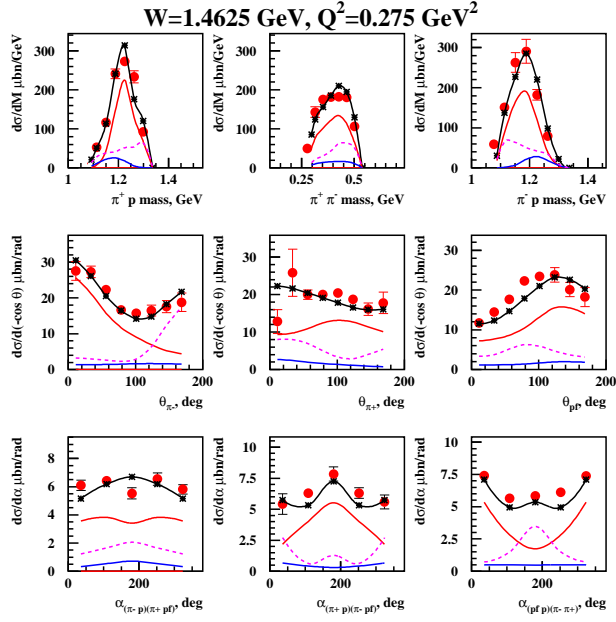


Figure A.11: 2π cross sections as function of hadronic variables fitted within a framework of JM05: black curve - total 2π cross section, red - $\pi^- \Delta^{++}$ channel, blue - $\pi^+ \Delta^0$, dashed magenta - direct 2π production.

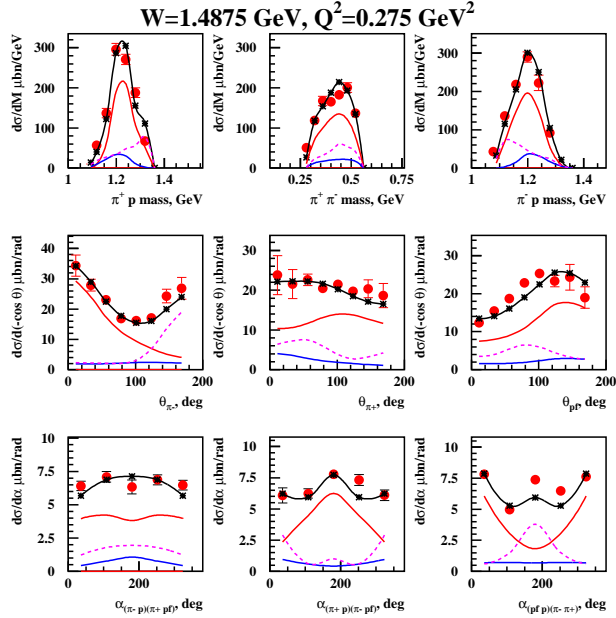


Figure A.12: 2π cross sections as function of hadronic variables fitted within a framework of JM05: black curve - total 2π cross section, red - $\pi^- \Delta^{++}$ channel, blue - $\pi^+ \Delta^0$, dashed magenta - direct 2π production.

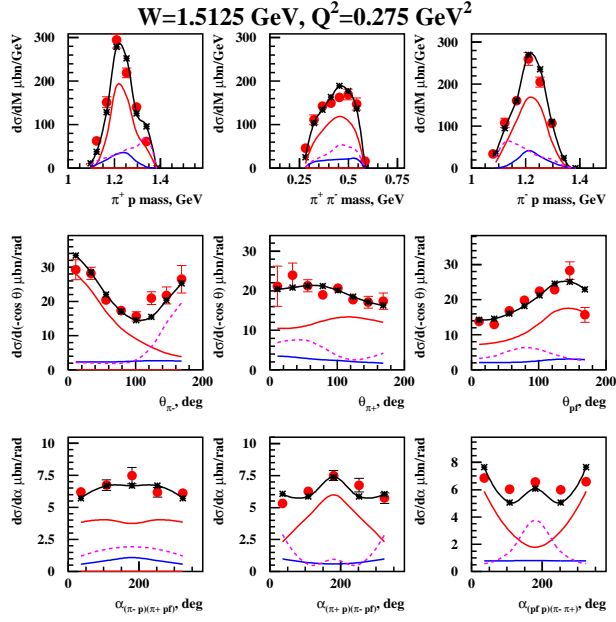


Figure A.13: 2π cross sections as function of hadronic variables fitted within a framework of JM05: black curve - total 2π cross section, red - $\pi^- \Delta^{++}$ channel, blue - $\pi^+ \Delta^0$, dashed magenta - direct 2π production.

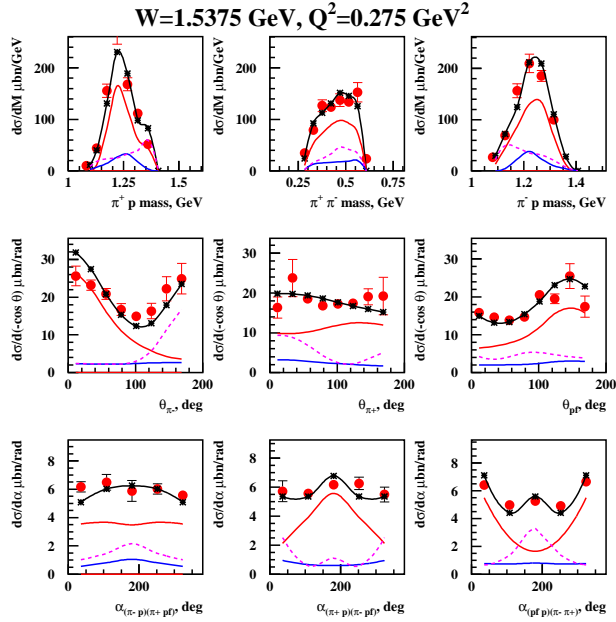


Figure A.14: 2π cross sections as function of hadronic variables fitted within a framework of JM05: black curve - total 2π cross section, red - $\pi^- \Delta^{++}$ channel, blue - $\pi^+ \Delta^0$, dashed magenta - direct 2π production.

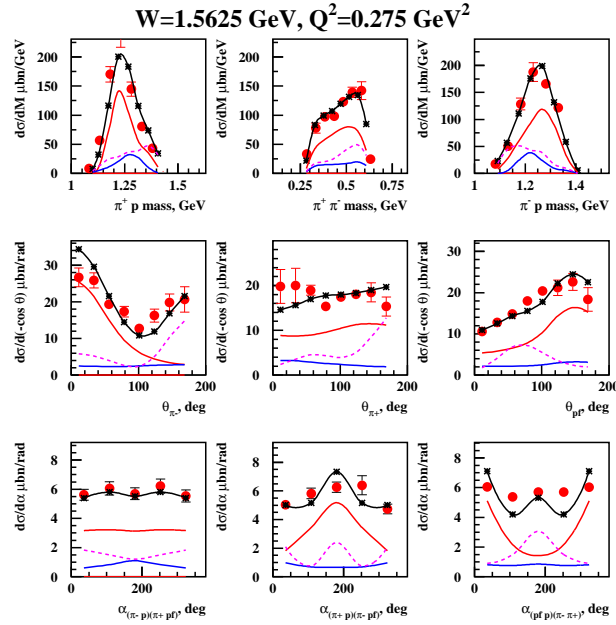


Figure A.15: 2π cross sections as function of hadronic variables fitted within a framework of JM05: black curve - total 2π cross section, red - $\pi^- \Delta^{++}$ channel, blue - $\pi^+ \Delta^0$, dashed magenta - direct 2π production.

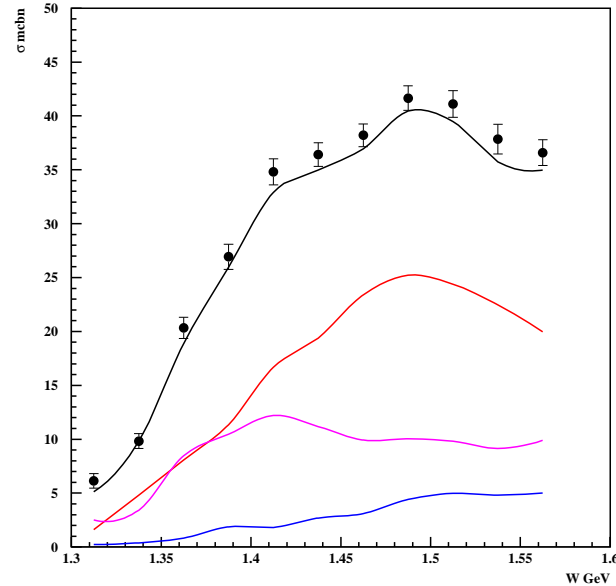


Figure A.16: W dependence of integrated 2π cross section for $Q^2 = 0.275$ GeV 2 . Black curve - total 2π cross section, red - $\pi^- \Delta^{++}$ channel, blue - $\pi^+ \Delta^0$, magenta - direct 2π production.

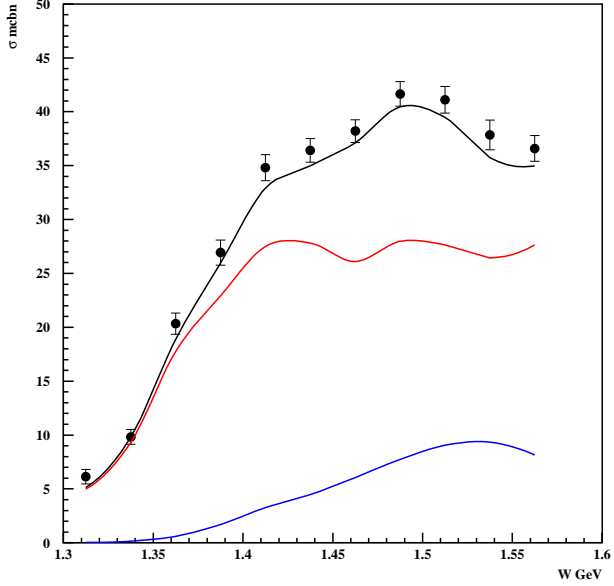


Figure A.17: W dependence of integrated 2π cross section for $Q^2 = 0.275 \text{ GeV}^2$. Black curve - total 2π cross section, red - non-resonant mechanisms, blue - N^* contribution.

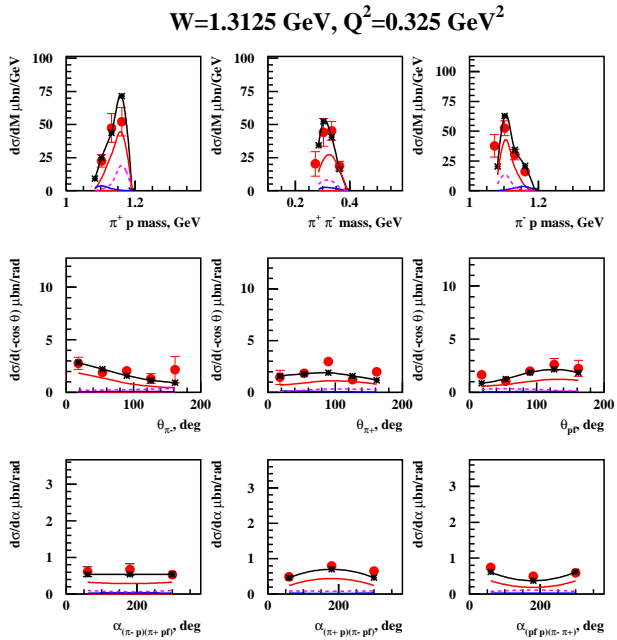


Figure A.18: 2π cross sections as function of hadronic variables fitted within a framework of JM05: black curve - total 2π cross section, red - $\pi^- \Delta^{++}$ channel, blue - $\pi^+ \Delta^0$, dashed magenta - direct 2π production.

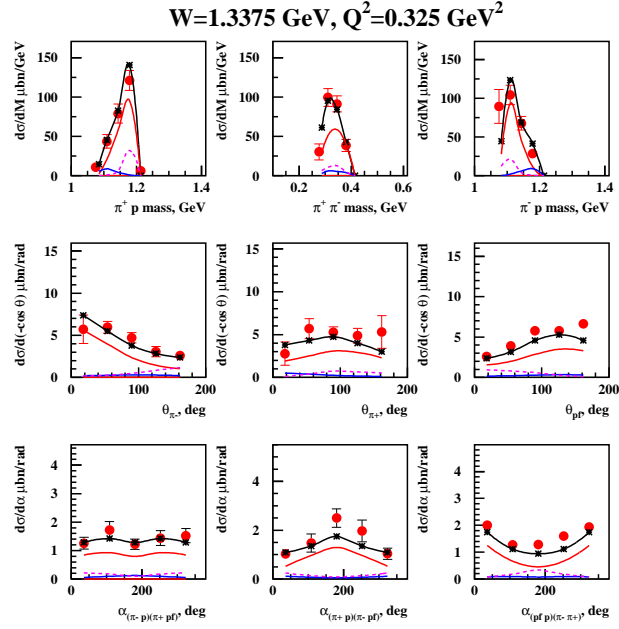


Figure A.19: 2π cross sections as function of hadronic variables fitted within a framework of JM05: black curve - total 2π cross section, red - $\pi^- \Delta^{++}$ channel, blue - $\pi^+ \Delta^0$, dashed magenta - direct 2π production.

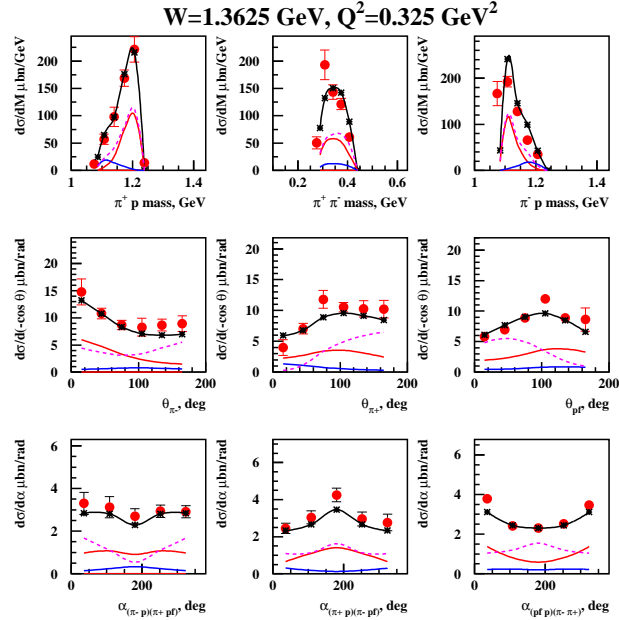


Figure A.20: 2π cross sections as function of hadronic variables fitted within a framework of JM05: black curve - total 2π cross section, red - $\pi^- \Delta^{++}$ channel, blue - $\pi^+ \Delta^0$, dashed magenta - direct 2π production.

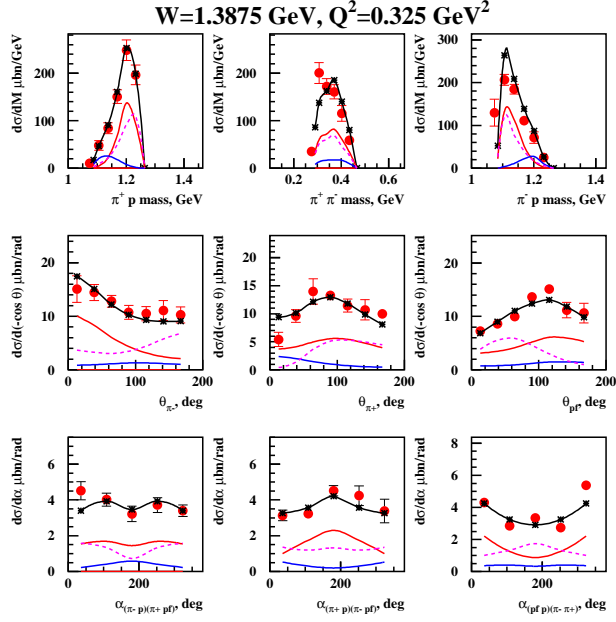


Figure A.21: 2π cross sections as function of hadronic variables fitted within a framework of JM05: black curve - total 2π cross section, red - $\pi^- \Delta^{++}$ channel, blue - $\pi^+ \Delta^0$, dashed magenta - direct 2π production.

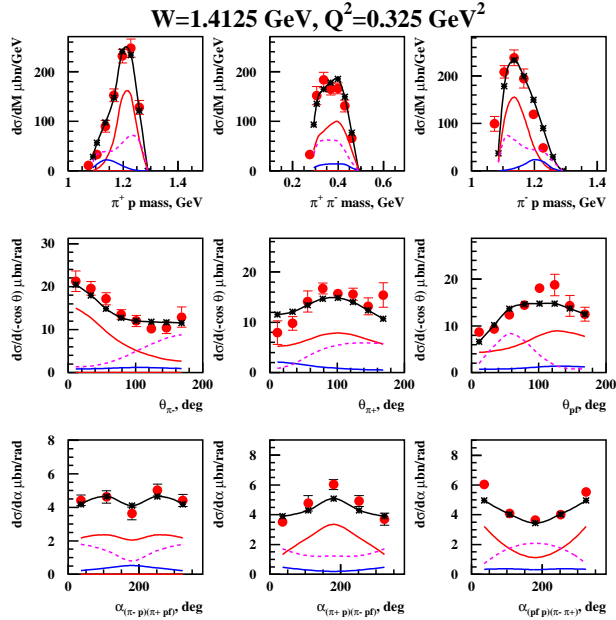


Figure A.22: 2π cross sections as function of hadronic variables fitted within a framework of JM05: black curve - total 2π cross section, red - $\pi^- \Delta^{++}$ channel, blue - $\pi^+ \Delta^0$, dashed magenta - direct 2π production.

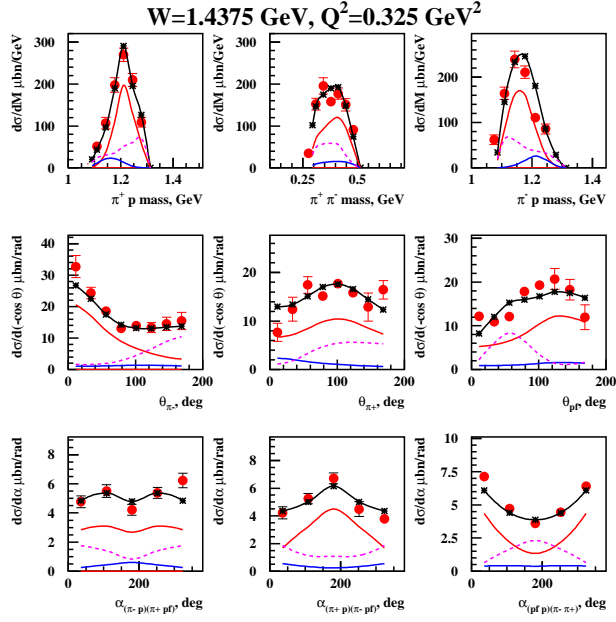


Figure A.23: 2π cross sections as function of hadronic variables fitted within a framework of JM05: black curve - total 2π cross section, red - $\pi^- \Delta^{++}$ channel, blue - $\pi^+ \Delta^0$, dashed magenta - direct 2π production.

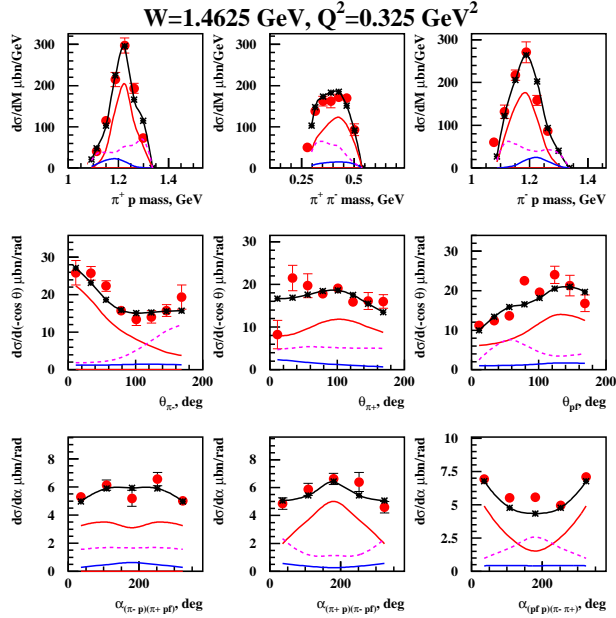


Figure A.24: 2π cross sections as function of hadronic variables fitted within a framework of JM05: black curve - total 2π cross section, red - $\pi^- \Delta^{++}$ channel, blue - $\pi^+ \Delta^0$, dashed magenta - direct 2π production.

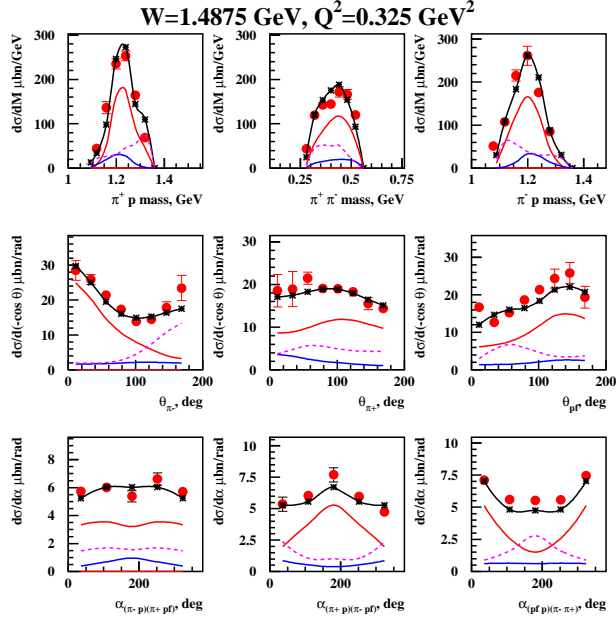


Figure A.25: 2π cross sections as function of hadronic variables fitted within a framework of JM05: black curve - total 2π cross section, red - $\pi^- \Delta^{++}$ channel, blue - $\pi^+ \Delta^0$, dashed magenta - direct 2π production.

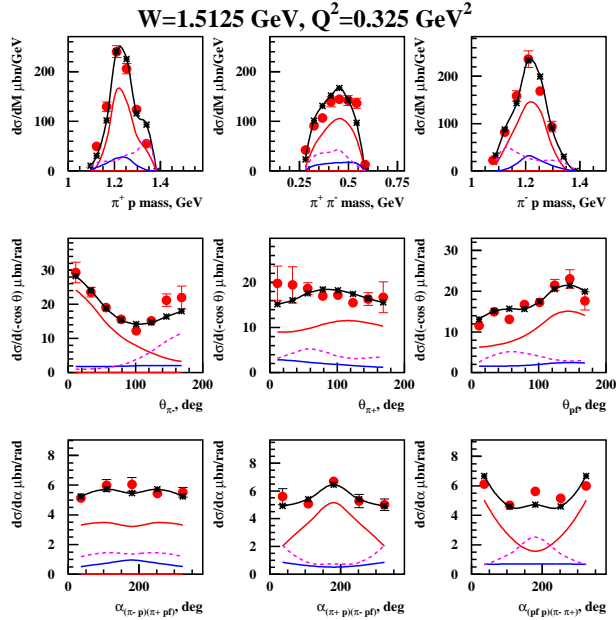


Figure A.26: 2π cross sections as function of hadronic variables fitted within a framework of JM05: black curve - total 2π cross section, red - $\pi^- \Delta^{++}$ channel, blue - $\pi^+ \Delta^0$, dashed magenta - direct 2π production.

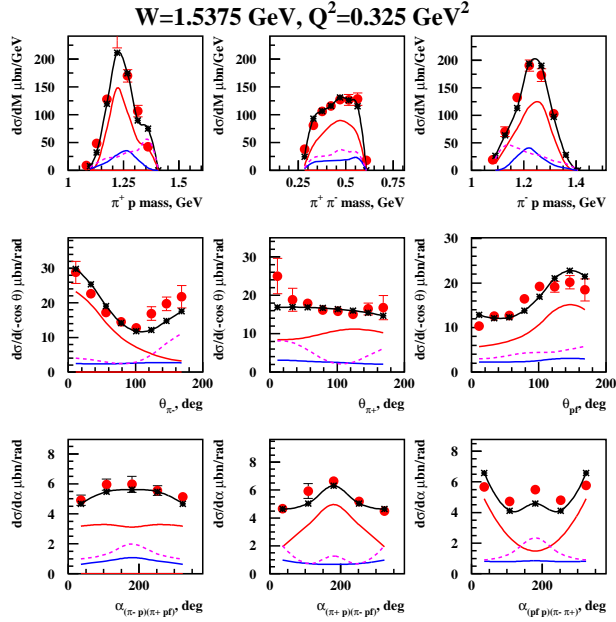


Figure A.27: 2π cross sections as function of hadronic variables fitted within a framework of JM05: black curve - total 2π cross section, red - $\pi^- \Delta^{++}$ channel, blue - $\pi^+ \Delta^0$, dashed magenta - direct 2π production.

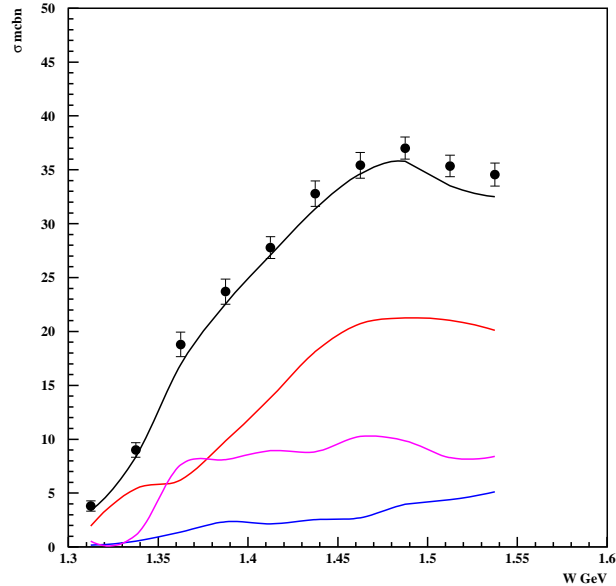


Figure A.28: W dependence of integrated 2π cross section for $Q^2 = 0.325 \text{ GeV}^2$. Black curve - total 2π cross section, red - $\pi^- \Delta^{++}$ channel, blue - $\pi^+ \Delta^0$, magenta - direct 2π production.

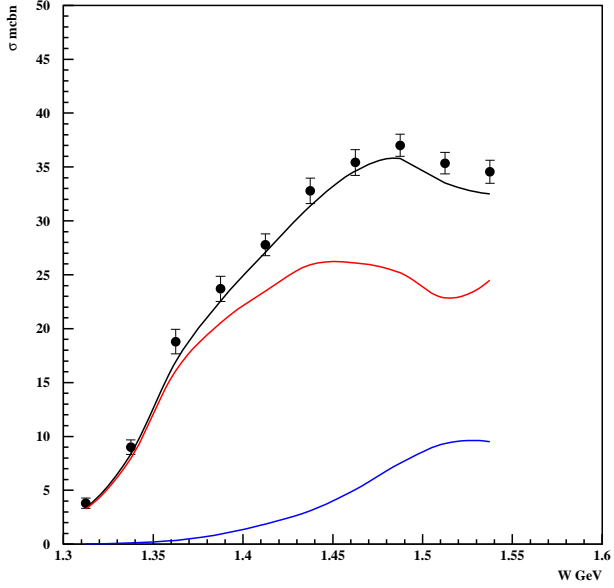


Figure A.29: W dependence of integrated 2π cross section for $Q^2 = 0.325 \text{ GeV}^2$. Black curve - total 2π cross section, red - non-resonant mechanisms, blue - N^* contribution.

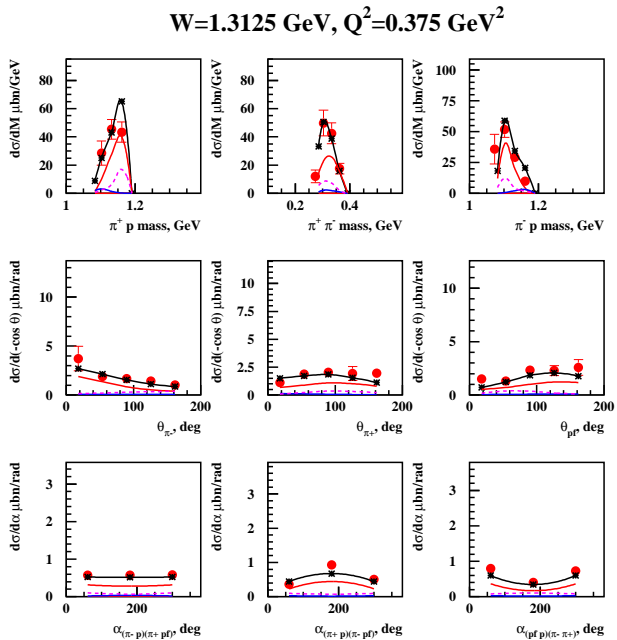


Figure A.30: 2π cross sections as function of hadronic variables fitted within a framework of JM05: black curve - total 2π cross section, red - $\pi^- \Delta^{++}$ channel, blue - $\pi^+ \Delta^0$, dashed magenta - direct 2π production.

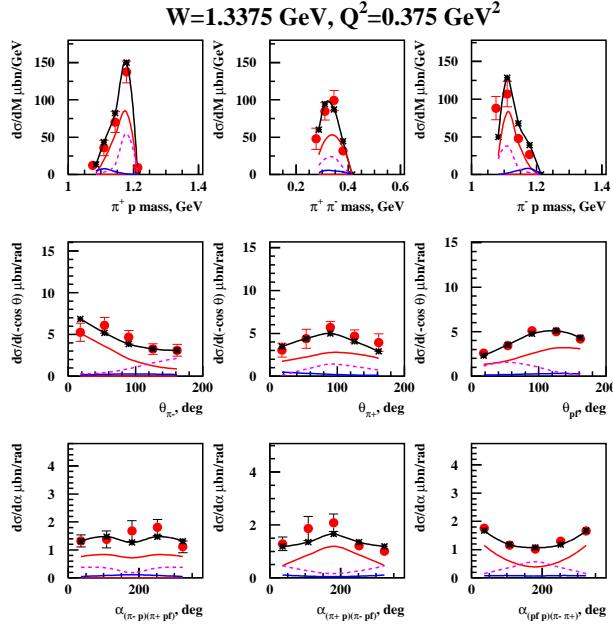


Figure A.31: 2π cross sections as function of hadronic variables fitted within a framework of JM05: black curve - total 2π cross section, red - $\pi^- \Delta^{++}$ channel, blue - $\pi^+ \Delta^0$, dashed magenta - direct 2π production.

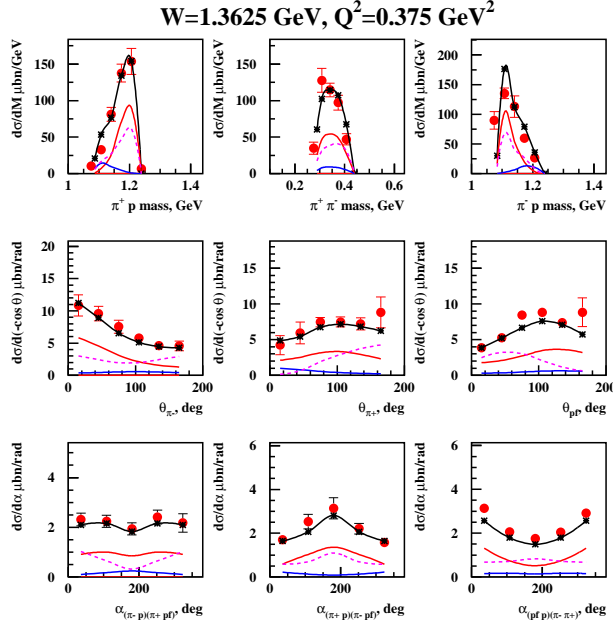


Figure A.32: 2π cross sections as function of hadronic variables fitted within a framework of JM05: black curve - total 2π cross section, red - $\pi^- \Delta^{++}$ channel, blue - $\pi^+ \Delta^0$, dashed magenta - direct 2π production.

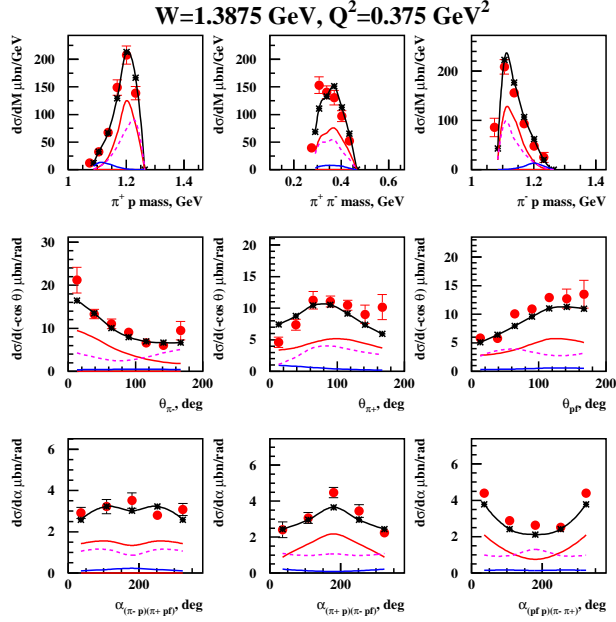


Figure A.33: 2π cross sections as function of hadronic variables fitted within a framework of JM05: black curve - total 2π cross section, red - $\pi^- \Delta^{++}$ channel, blue - $\pi^+ \Delta^0$, dashed magenta - direct 2π production.

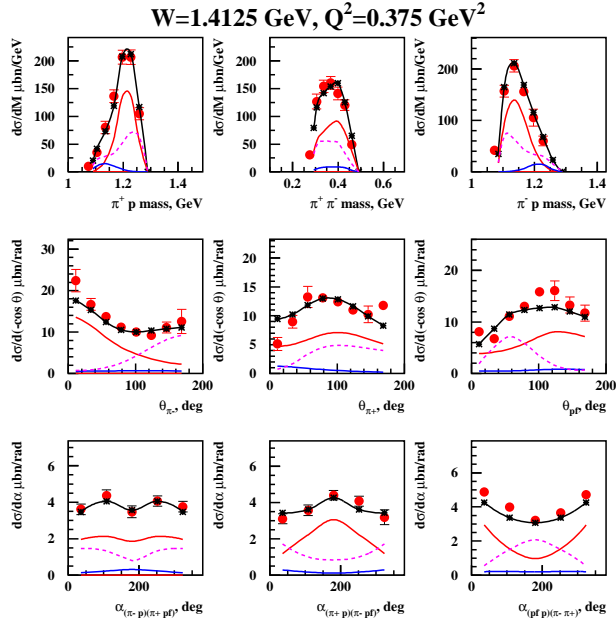


Figure A.34: 2π cross sections as function of hadronic variables fitted within a framework of JM05: black curve - total 2π cross section, red - $\pi^- \Delta^{++}$ channel, blue - $\pi^+ \Delta^0$, dashed magenta - direct 2π production.

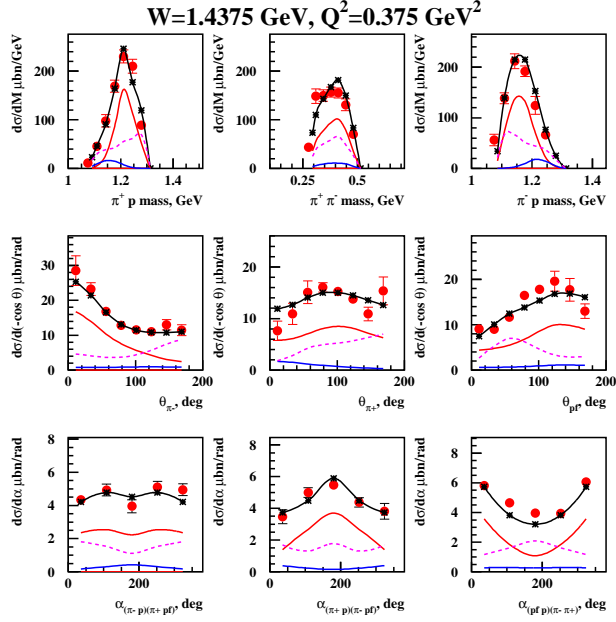


Figure A.35: 2π cross sections as function of hadronic variables fitted within a framework of JM05: black curve - total 2π cross section, red - $\pi^- \Delta^{++}$ channel, blue - $\pi^+ \Delta^0$, dashed magenta - direct 2π production.

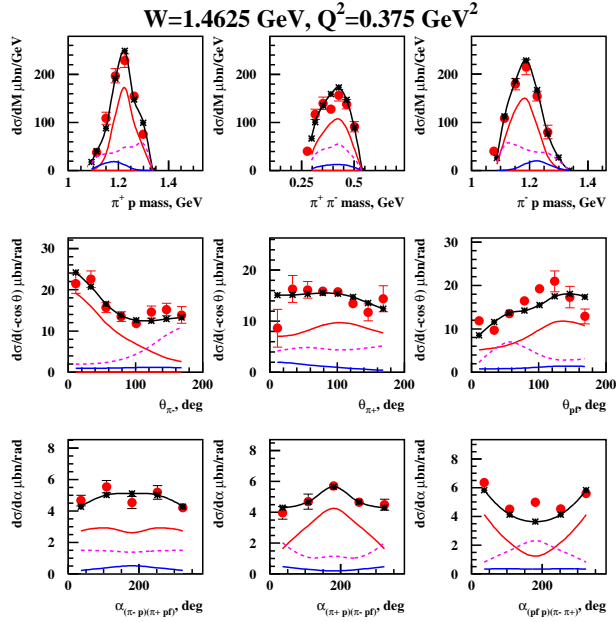


Figure A.36: 2π cross sections as function of hadronic variables fitted within a framework of JM05: black curve - total 2π cross section, red - $\pi^- \Delta^{++}$ channel, blue - $\pi^+ \Delta^0$, dashed magenta - direct 2π production.

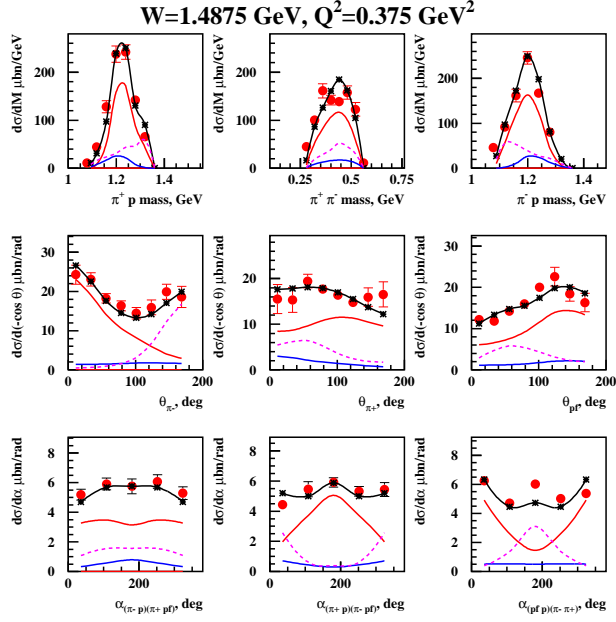


Figure A.37: 2π cross sections as function of hadronic variables fitted within a framework of JM05: black curve - total 2π cross section, red - $\pi^- \Delta^{++}$ channel, blue - $\pi^+ \Delta^0$, dashed magenta - direct 2π production.

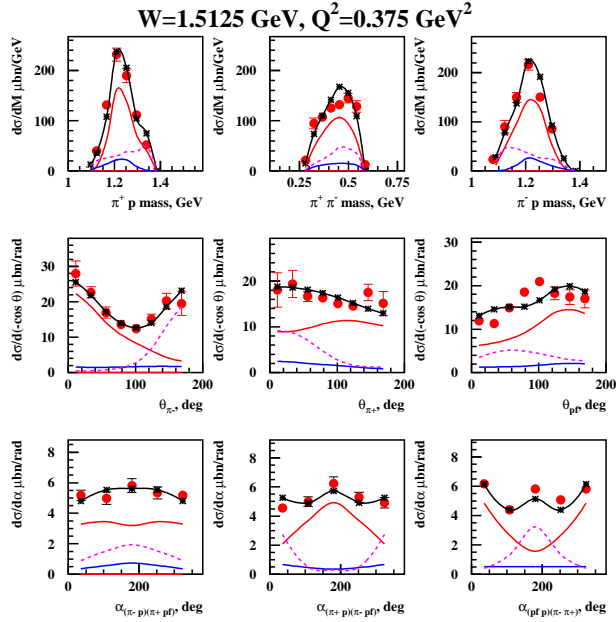


Figure A.38: 2π cross sections as function of hadronic variables fitted within a framework of JM05: black curve - total 2π cross section, red - $\pi^- \Delta^{++}$ channel, blue - $\pi^+ \Delta^0$, dashed magenta - direct 2π production.

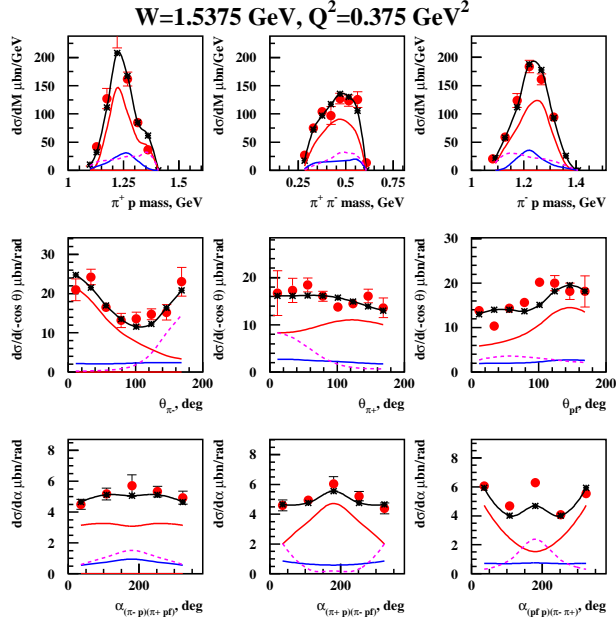


Figure A.39: 2π cross sections as function of hadronic variables fitted within a framework of JM05: black curve - total 2π cross section, red - $\pi^- \Delta^{++}$ channel, blue - $\pi^+ \Delta^0$, dashed magenta - direct 2π production.

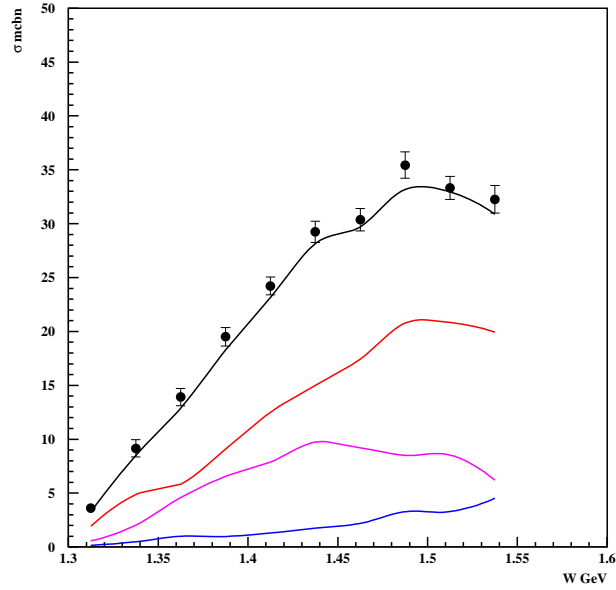


Figure A.40: W dependence of integrated 2π cross section for $Q^2 = 0.375 \text{ GeV}^2$. Black curve - total 2π cross section, red - $\pi^- \Delta^{++}$ channel, blue - $\pi^+ \Delta^0$, magenta - direct 2π production.

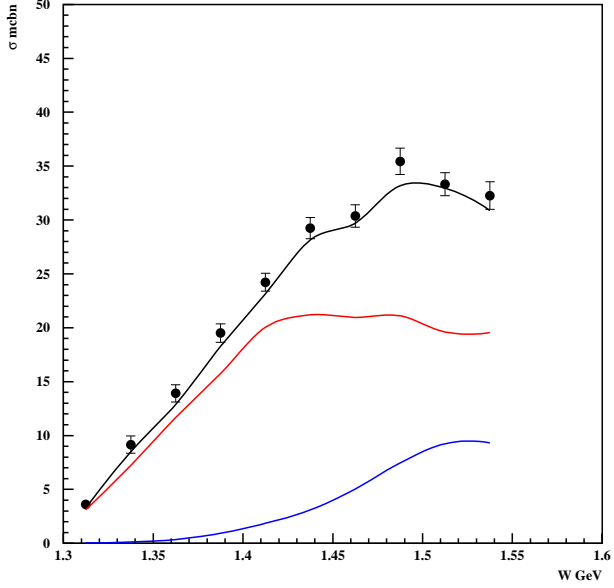


Figure A.41: W dependence of integrated 2π cross section for $Q^2 = 0.375 \text{ GeV}^2$. Black curve - total 2π cross section, red - non-resonant mechanisms, blue - N^* contribution.

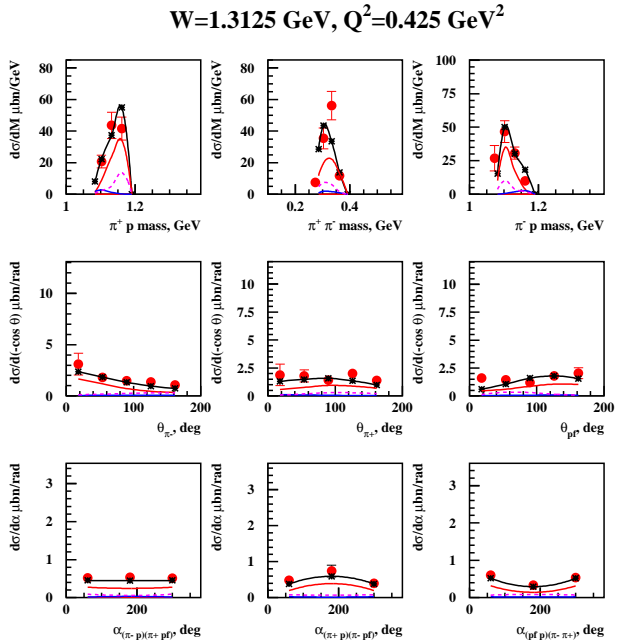


Figure A.42: 2π cross sections as function of hadronic variables fitted within a framework of JM05: black curve - total 2π cross section, red - $\pi^- \Delta^{++}$ channel, blue - $\pi^+ \Delta^0$, dashed magenta - direct 2π production.

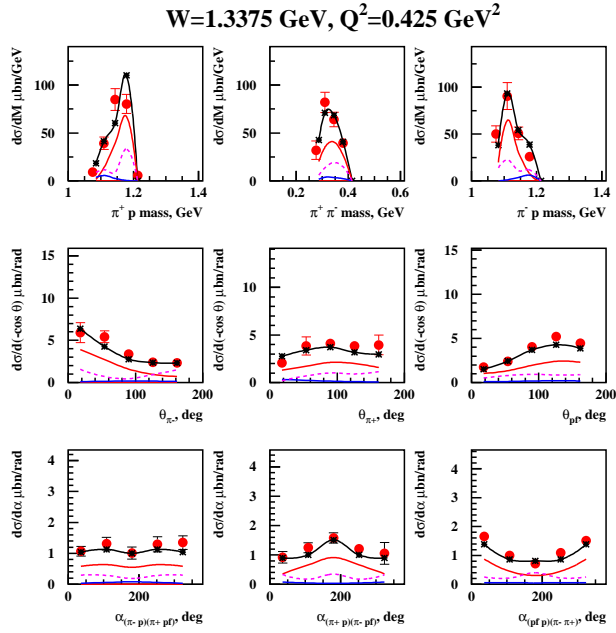


Figure A.43: 2π cross sections as function of hadronic variables fitted within a framework of JM05: black curve - total 2π cross section, red - $\pi^- \Delta^{++}$ channel, blue - $\pi^+ \Delta^0$, dashed magenta - direct 2π production.

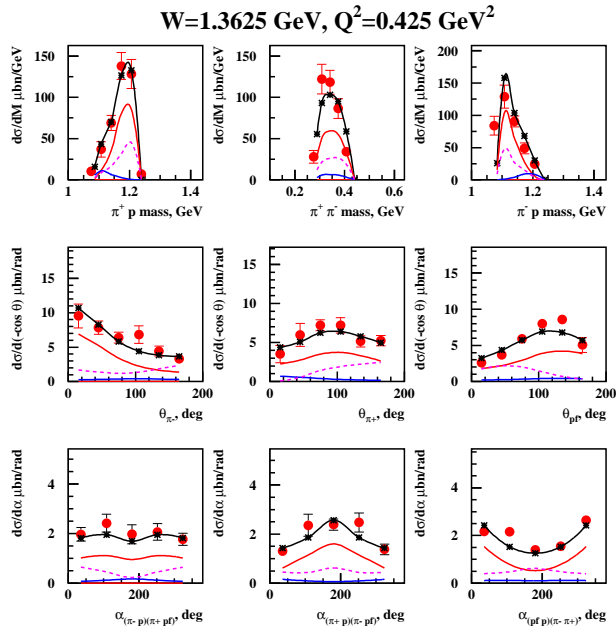


Figure A.44: 2π cross sections as function of hadronic variables fitted within a framework of JM05: black curve - total 2π cross section, red - $\pi^- \Delta^{++}$ channel, blue - $\pi^+ \Delta^0$, dashed magenta - direct 2π production.

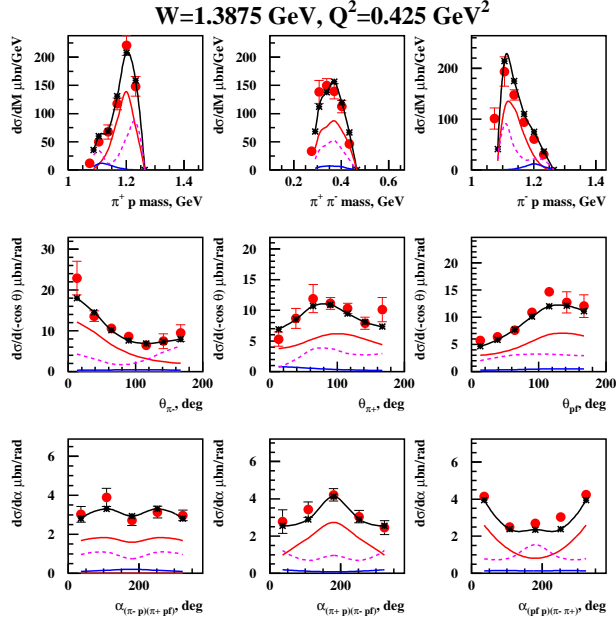


Figure A.45: 2π cross sections as function of hadronic variables fitted within a framework of JM05: black curve - total 2π cross section, red - $\pi^-\Delta^{++}$ channel, blue - $\pi^+\Delta^0$, dashed magenta - direct 2π production.

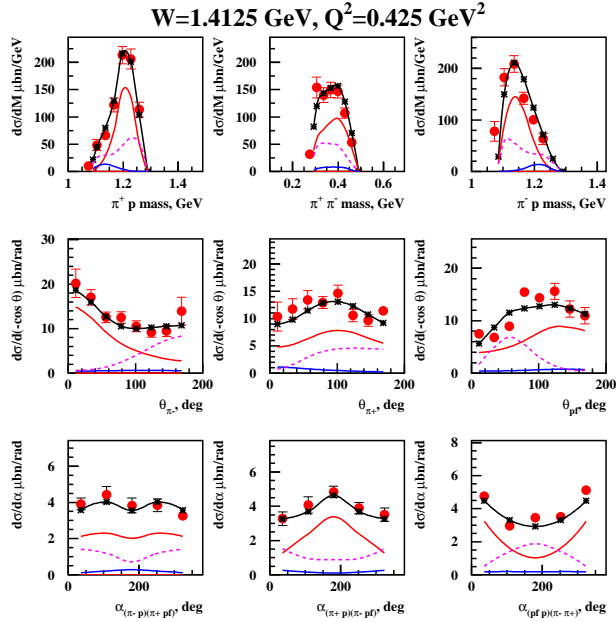


Figure A.46: 2π cross sections as function of hadronic variables fitted within a framework of JM05: black curve - total 2π cross section, red - $\pi^-\Delta^{++}$ channel, blue - $\pi^+\Delta^0$, dashed magenta - direct 2π production.

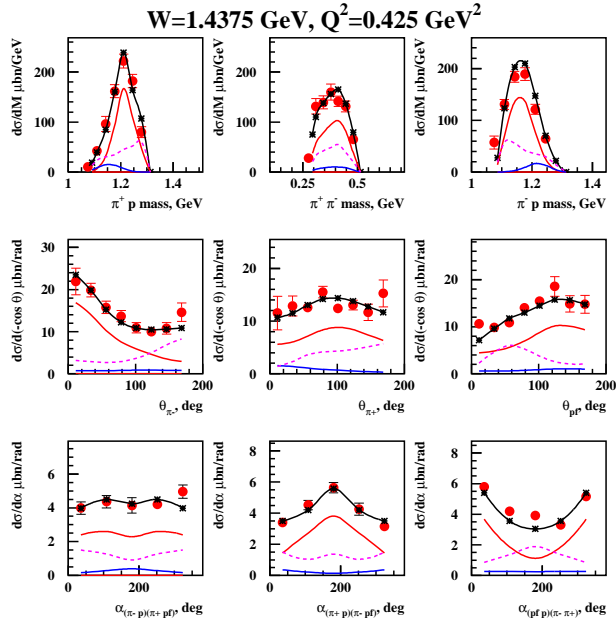


Figure A.47: 2π cross sections as function of hadronic variables fitted within a framework of JM05: black curve - total 2π cross section, red - $\pi^- \Delta^{++}$ channel, blue - $\pi^+ \Delta^0$, dashed magenta - direct 2π production.

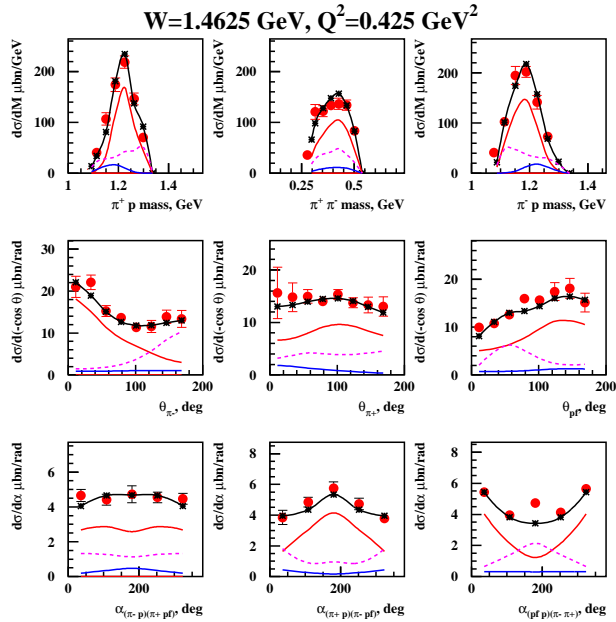


Figure A.48: 2π cross sections as function of hadronic variables fitted within a framework of JM05: black curve - total 2π cross section, red - $\pi^- \Delta^{++}$ channel, blue - $\pi^+ \Delta^0$, dashed magenta - direct 2π production.

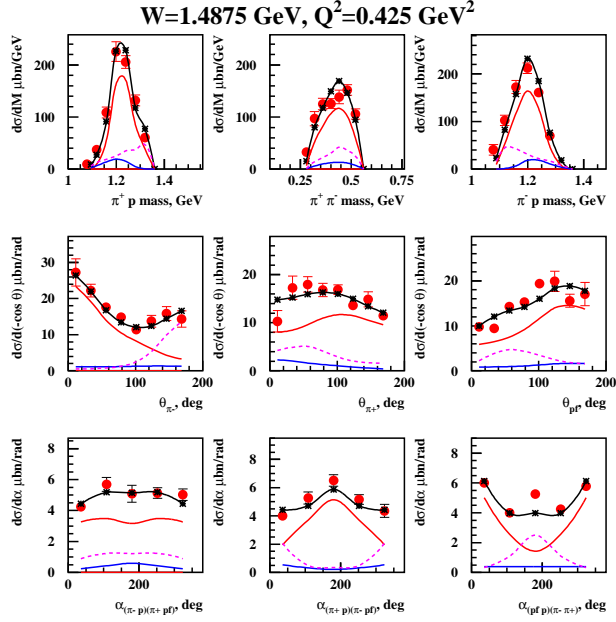


Figure A.49: 2π cross sections as function of hadronic variables fitted within a framework of JM05: black curve - total 2π cross section, red - $\pi^- \Delta^{++}$ channel, blue - $\pi^+ \Delta^0$, dashed magenta - direct 2π production.

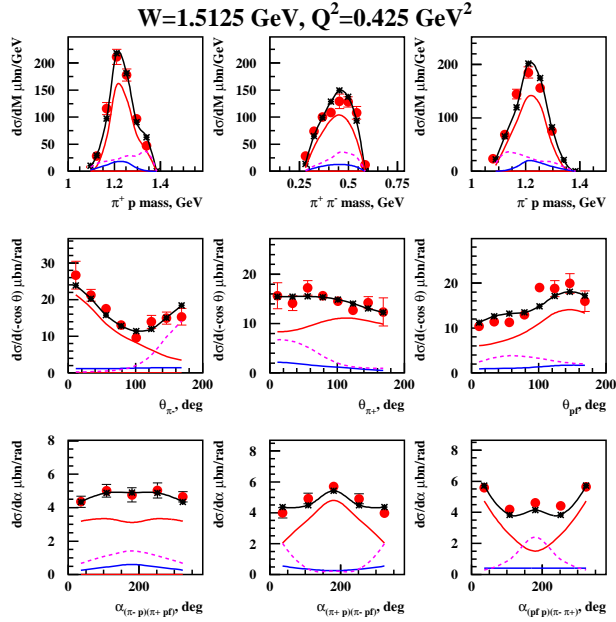


Figure A.50: 2π cross sections as function of hadronic variables fitted within a framework of JM05: black curve - total 2π cross section, red - $\pi^- \Delta^{++}$ channel, blue - $\pi^+ \Delta^0$, dashed magenta - direct 2π production.

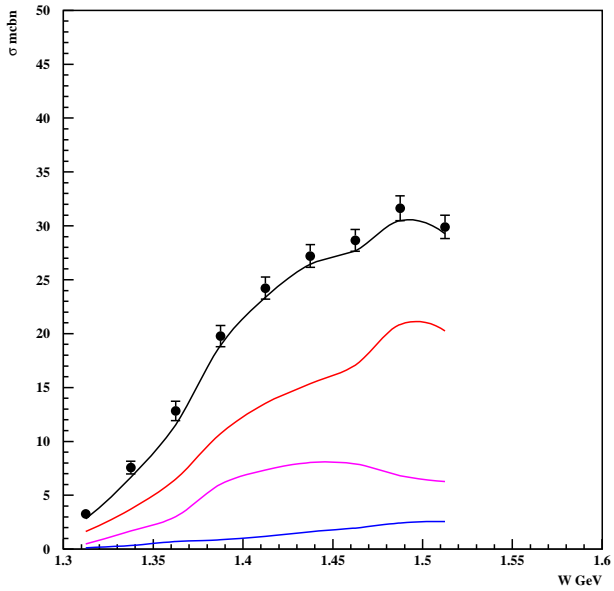


Figure A.51: W dependence of integrated 2π cross section for $Q^2 = 0.425 \text{ GeV}^2$. Black curve - total 2π cross section, red - $\pi^- \Delta^{++}$ channel, blue - $\pi^+ \Delta^0$, magenta - direct 2π production.

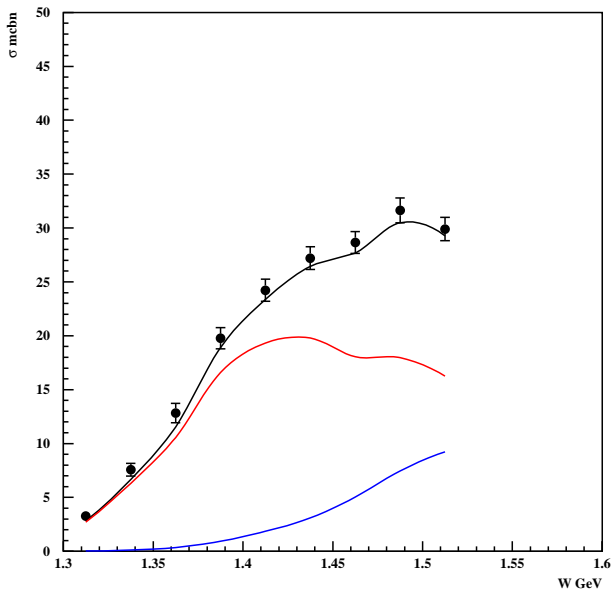


Figure A.52: W dependence of integrated 2π cross section for $Q^2 = 0.425 \text{ GeV}^2$. Black curve - total 2π cross section, red - non-resonant mechanisms, blue - N^* contribution.

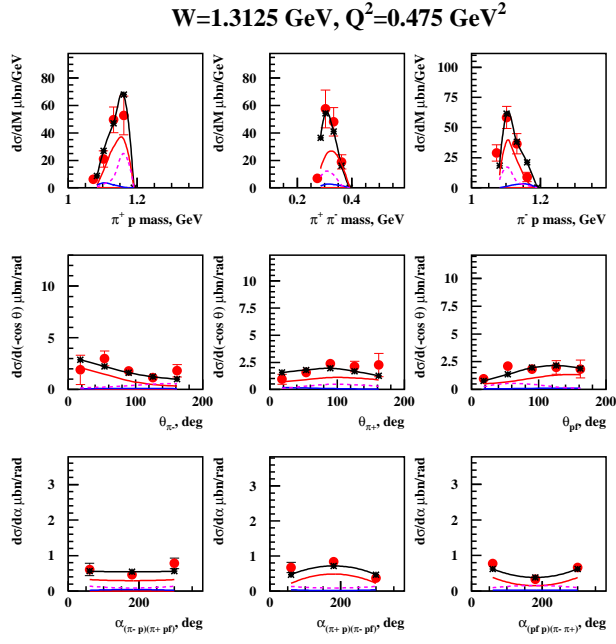


Figure A.53: 2π cross sections as function of hadronic variables fitted within a framework of JM05: black curve - total 2π cross section, red - $\pi^- \Delta^{++}$ channel, blue - $\pi^+ \Delta^0$, dashed magenta - direct 2π production.

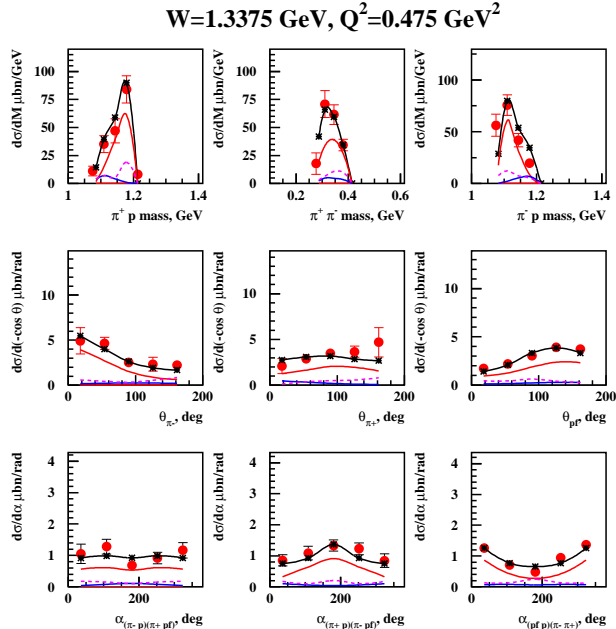


Figure A.54: 2π cross sections as function of hadronic variables fitted within a framework of JM05: black curve - total 2π cross section, red - $\pi^- \Delta^{++}$ channel, blue - $\pi^+ \Delta^0$, dashed magenta - direct 2π production.

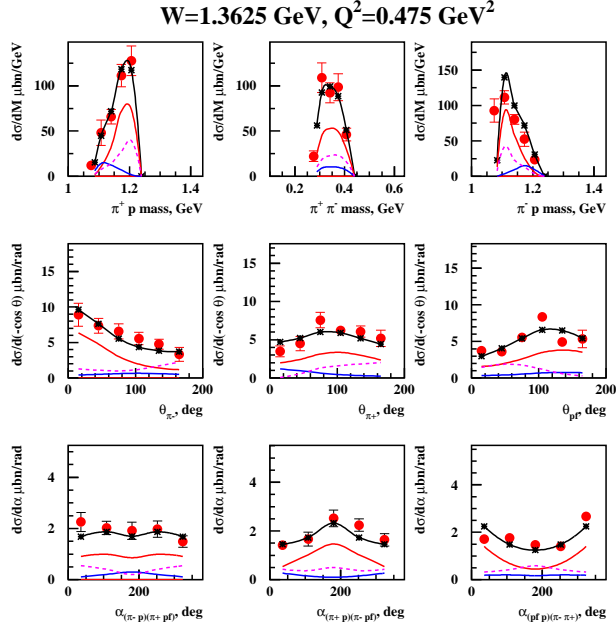


Figure A.55: 2π cross sections as function of hadronic variables fitted within a framework of JM05: black curve - total 2π cross section, red - $\pi^- \Delta^{++}$ channel, blue - $\pi^+ \Delta^0$, dashed magenta - direct 2π production.

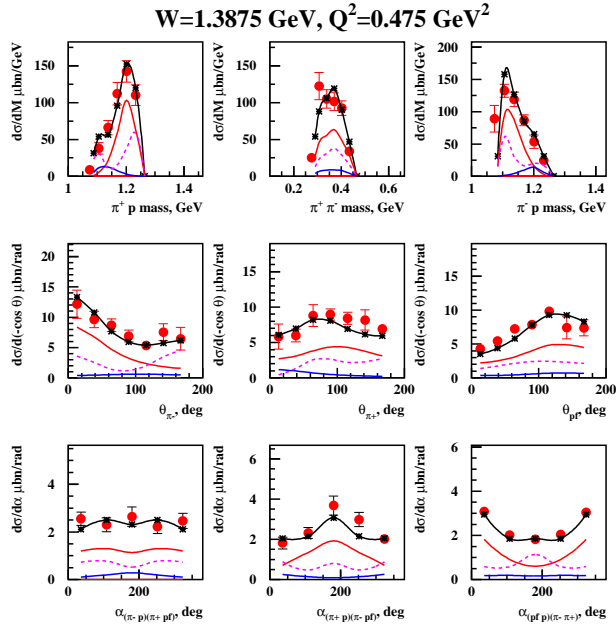


Figure A.56: 2π cross sections as function of hadronic variables fitted within a framework of JM05: black curve - total 2π cross section, red - $\pi^- \Delta^{++}$ channel, blue - $\pi^+ \Delta^0$, dashed magenta - direct 2π production.

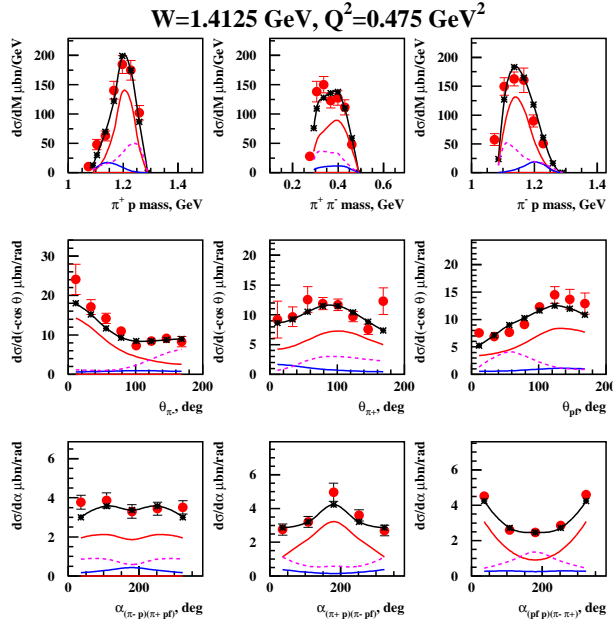


Figure A.57: 2π cross sections as function of hadronic variables fitted within a framework of JM05: black curve - total 2π cross section, red - $\pi^-\Delta^{++}$ channel, blue - $\pi^+\Delta^0$, dashed magenta - direct 2π production.

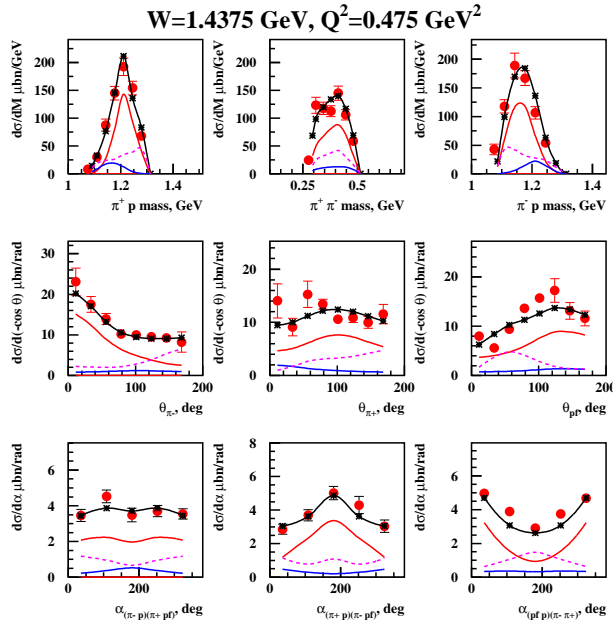


Figure A.58: 2π cross sections as function of hadronic variables fitted within a framework of JM05: black curve - total 2π cross section, red - $\pi^-\Delta^{++}$ channel, blue - $\pi^+\Delta^0$, dashed magenta - direct 2π production.

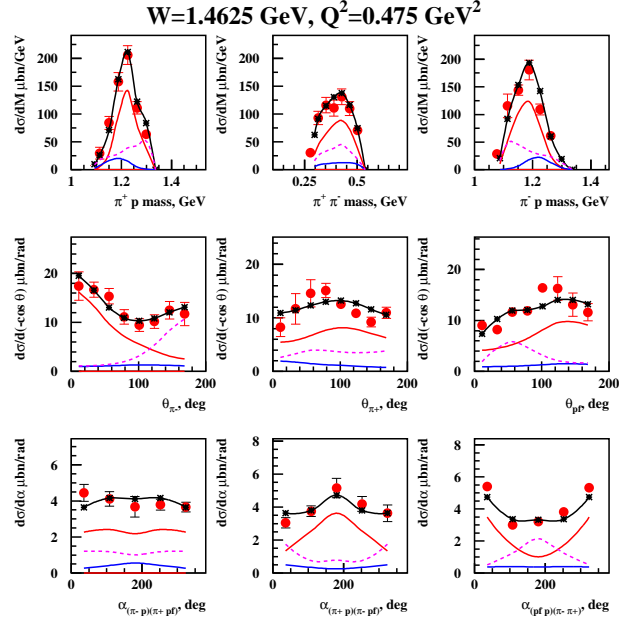


Figure A.59: 2π cross sections as function of hadronic variables fitted within a framework of JM05: black curve - total 2π cross section, red - $\pi^- \Delta^{++}$ channel, blue - $\pi^+ \Delta^0$, dashed magenta - direct 2π production.

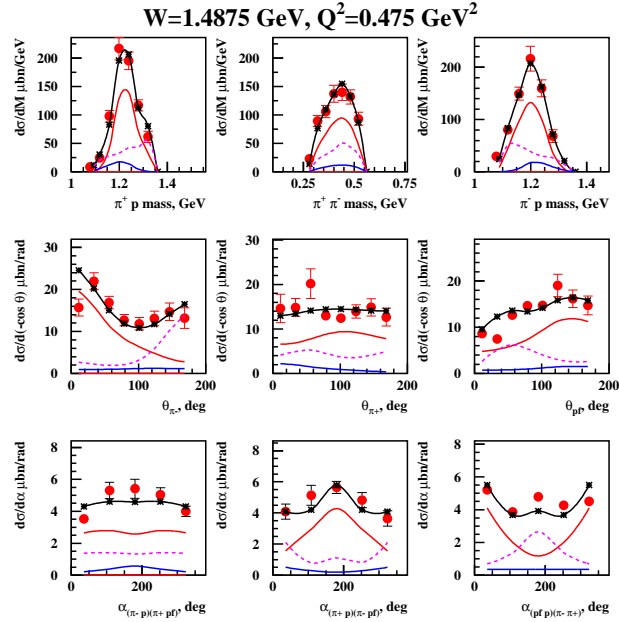


Figure A.60: 2π cross sections as function of hadronic variables fitted within a framework of JM05: black curve - total 2π cross section, red - $\pi^- \Delta^{++}$ channel, blue - $\pi^+ \Delta^0$, dashed magenta - direct 2π production.

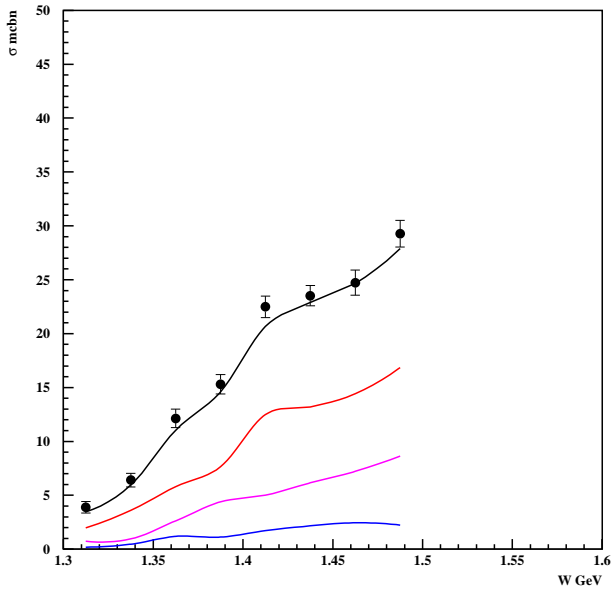


Figure A.61: W dependence of integrated 2π cross section for $Q^2 = 0.475 \text{ GeV}^2$. Black curve - total 2π cross section, red - $\pi^- \Delta^{++}$ channel, blue - $\pi^+ \Delta^0$, magenta - direct 2π production.

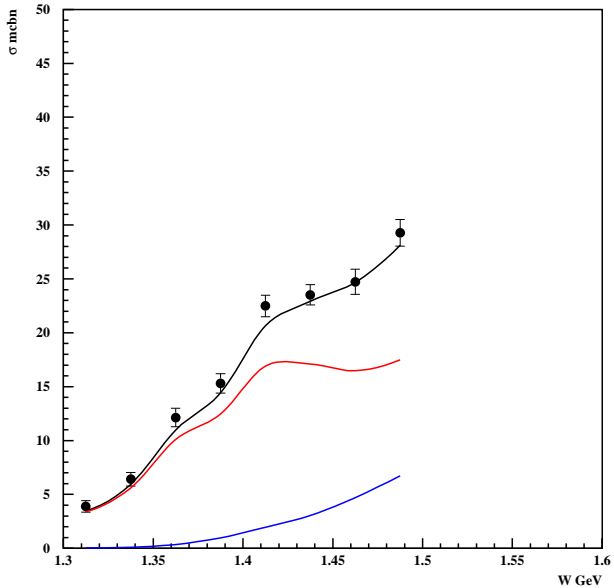


Figure A.62: W dependence of integrated 2π cross section for $Q^2 = 0.475 \text{ GeV}^2$. Black curve - total 2π cross section, red - non-resonant mechanisms, blue - N^* contribution.

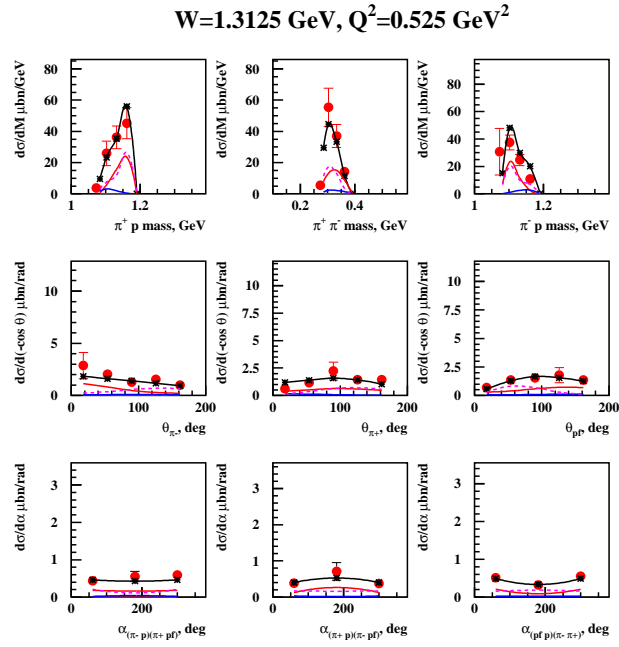


Figure A.63: 2π cross sections as function of hadronic variables fitted within a framework of JM05: black curve - total 2π cross section, red - $\pi^- \Delta^{++}$ channel, blue - $\pi^+ \Delta^0$, dashed magenta - direct 2π production.

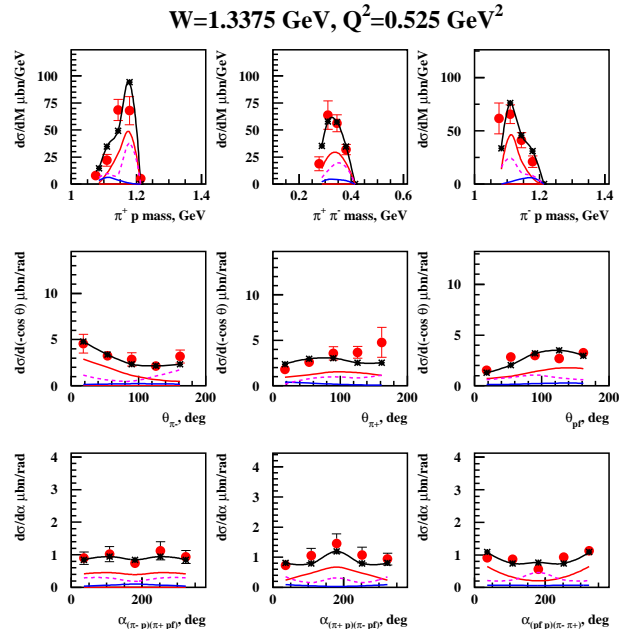


Figure A.64: 2π cross sections as function of hadronic variables fitted within a framework of JM05: black curve - total 2π cross section, red - $\pi^- \Delta^{++}$ channel, blue - $\pi^+ \Delta^0$, dashed magenta - direct 2π production.

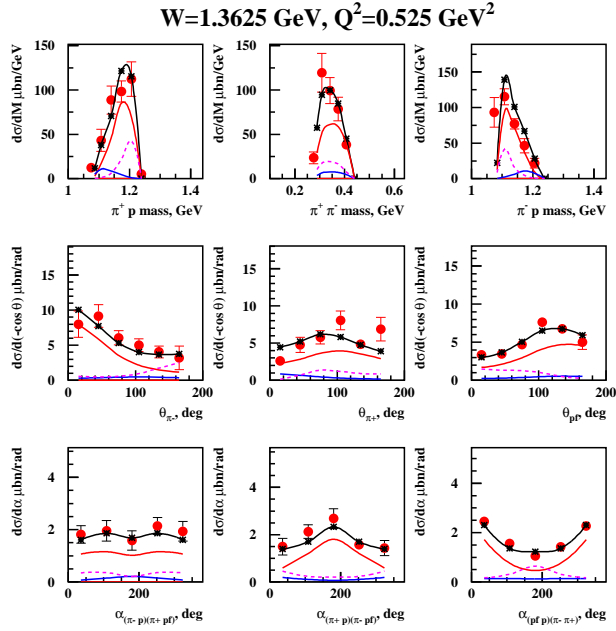


Figure A.65: 2π cross sections as function of hadronic variables fitted within a framework of JM05: black curve - total 2π cross section, red - $\pi^- \Delta^{++}$ channel, blue - $\pi^+ \Delta^0$, dashed magenta - direct 2π production.

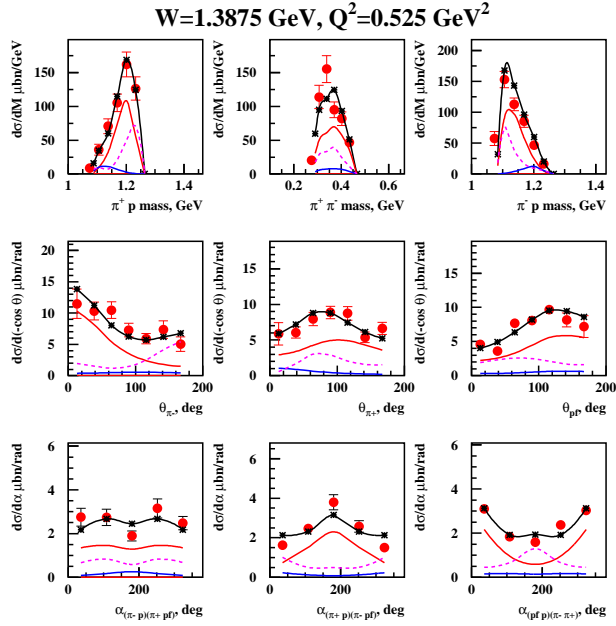


Figure A.66: 2π cross sections as function of hadronic variables fitted within a framework of JM05: black curve - total 2π cross section, red - $\pi^- \Delta^{++}$ channel, blue - $\pi^+ \Delta^0$, dashed magenta - direct 2π production.

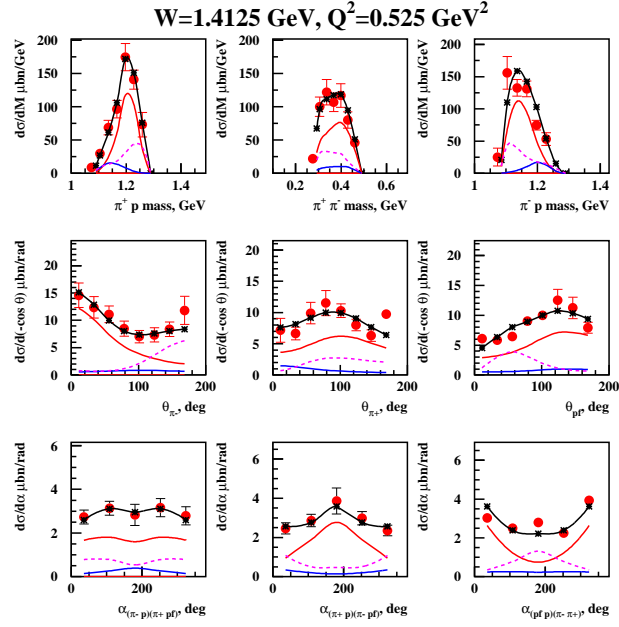


Figure A.67: 2π cross sections as function of hadronic variables fitted within a framework of JM05: black curve - total 2π cross section, red - $\pi^- \Delta^{++}$ channel, blue - $\pi^+ \Delta^0$, dashed magenta - direct 2π production.

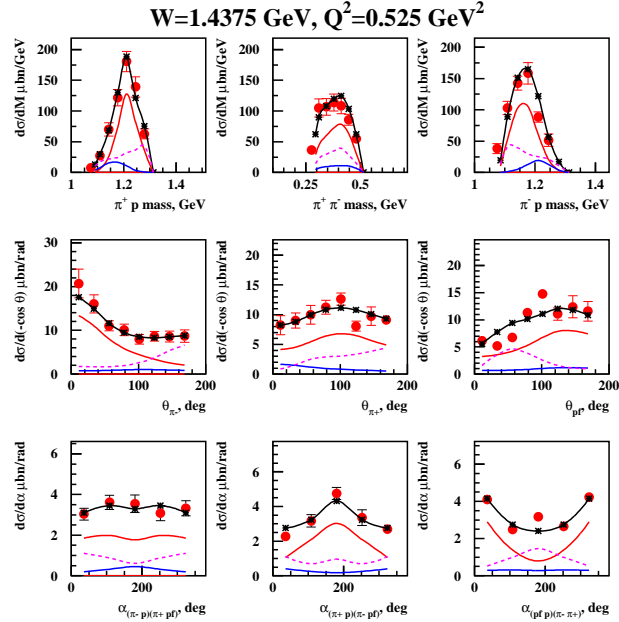


Figure A.68: 2π cross sections as function of hadronic variables fitted within a framework of JM05: black curve - total 2π cross section, red - $\pi^- \Delta^{++}$ channel, blue - $\pi^+ \Delta^0$, dashed magenta - direct 2π production.

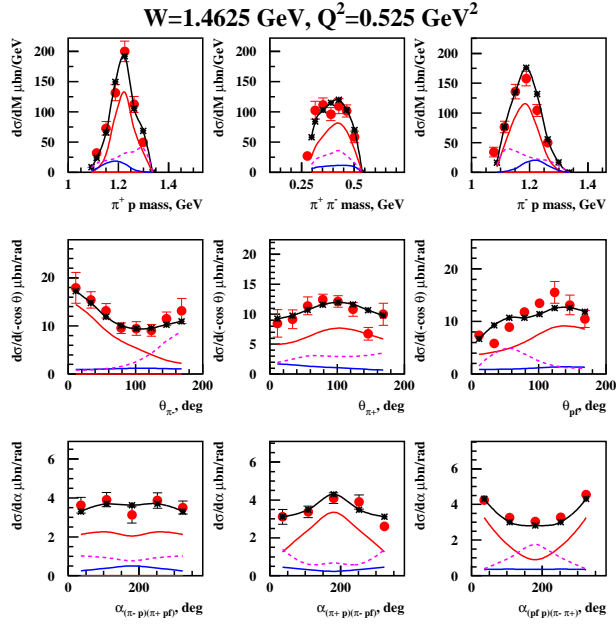


Figure A.69: 2π cross sections as function of hadronic variables fitted within a framework of JM05: black curve - total 2π cross section, red - $\pi^- \Delta^{++}$ channel, blue - $\pi^+ \Delta^0$, dashed magenta - direct 2π production.

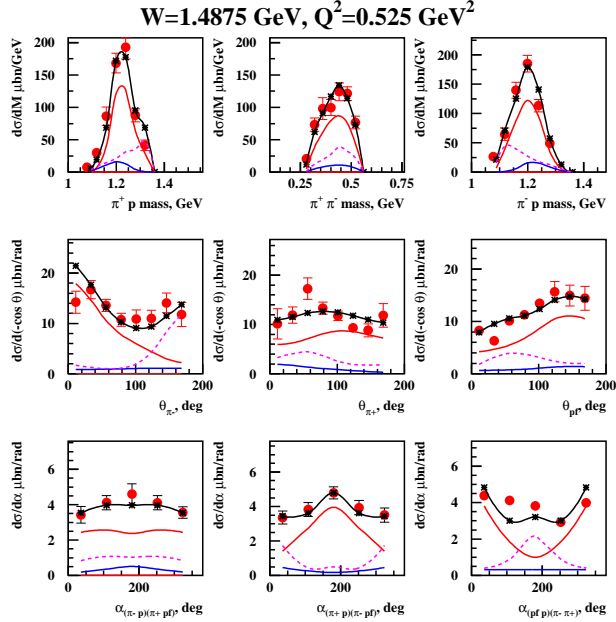


Figure A.70: 2π cross sections as function of hadronic variables fitted within a framework of JM05: black curve - total 2π cross section, red - $\pi^- \Delta^{++}$ channel, blue - $\pi^+ \Delta^0$, dashed magenta - direct 2π production.

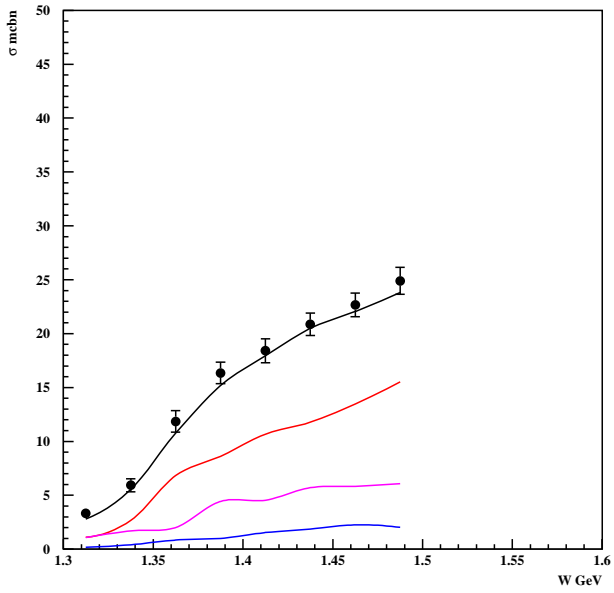


Figure A.71: W dependence of integrated 2π cross section for $Q^2 = 0.525 \text{ GeV}^2$. Black curve - total 2π cross section, red - $\pi^- \Delta^{++}$ channel, blue - $\pi^+ \Delta^0$, magenta - direct 2π production.

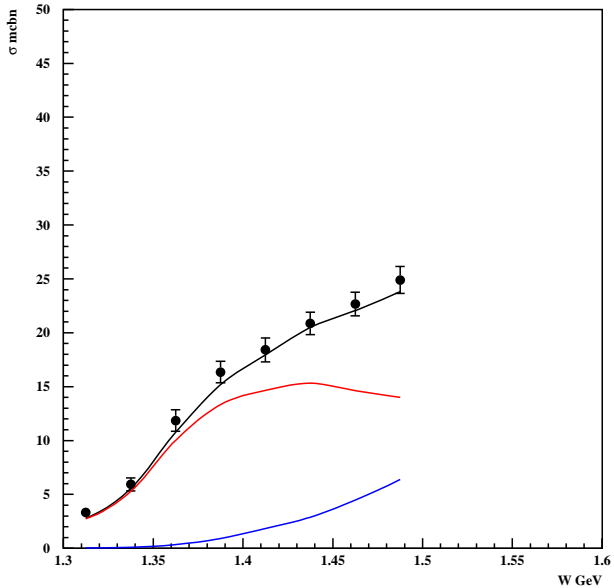


Figure A.72: W dependence of integrated 2π cross section for $Q^2 = 0.525 \text{ GeV}^2$. Black curve - total 2π cross section, red - non-resonant mechanisms, blue - N^* contribution.

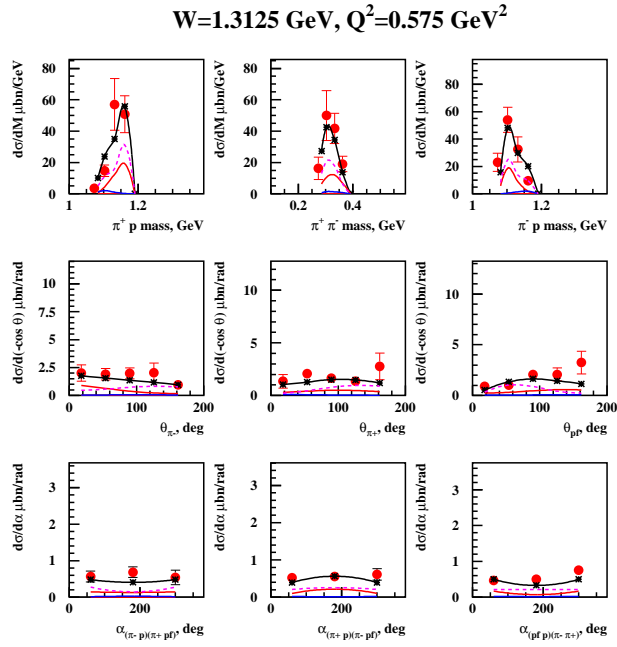


Figure A.73: 2π cross sections as function of hadronic variables fitted within a framework of JM05: black curve - total 2π cross section, red - $\pi^- \Delta^{++}$ channel, blue - $\pi^+ \Delta^0$, dashed magenta - direct 2π production.

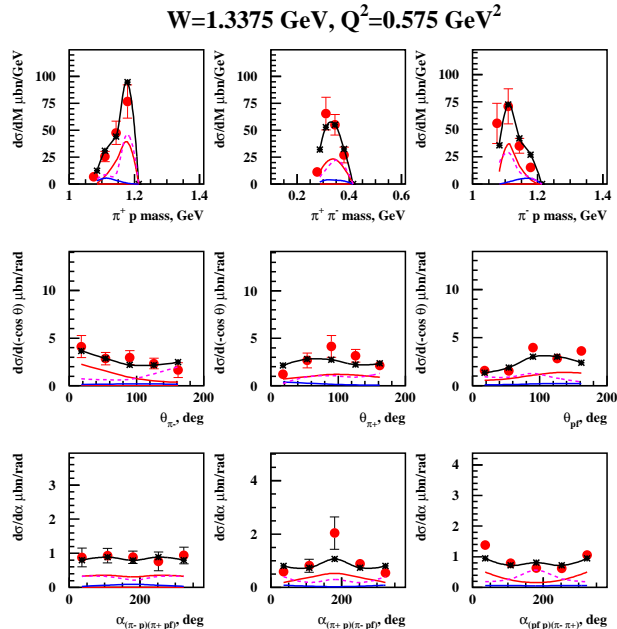


Figure A.74: 2π cross sections as function of hadronic variables fitted within a framework of JM05: black curve - total 2π cross section, red - $\pi^- \Delta^{++}$ channel, blue - $\pi^+ \Delta^0$, dashed magenta - direct 2π production.

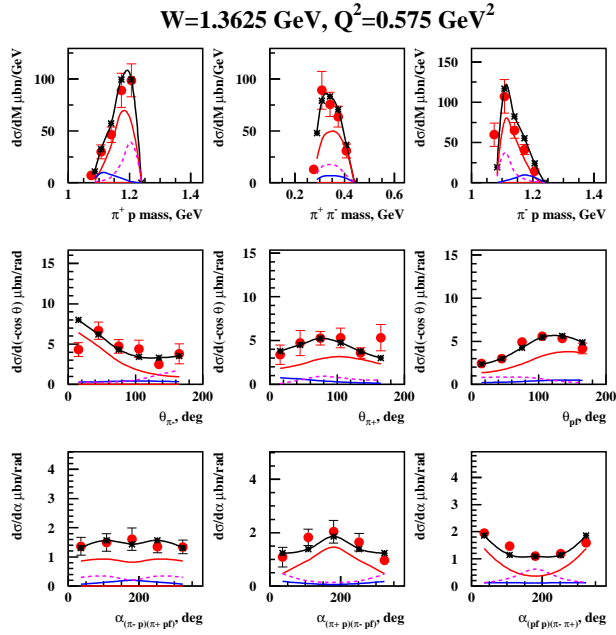


Figure A.75: 2π cross sections as function of hadronic variables fitted within a framework of JM05: black curve - total 2π cross section, red - $\pi^- \Delta^{++}$ channel, blue - $\pi^+ \Delta^0$, dashed magenta - direct 2π production.

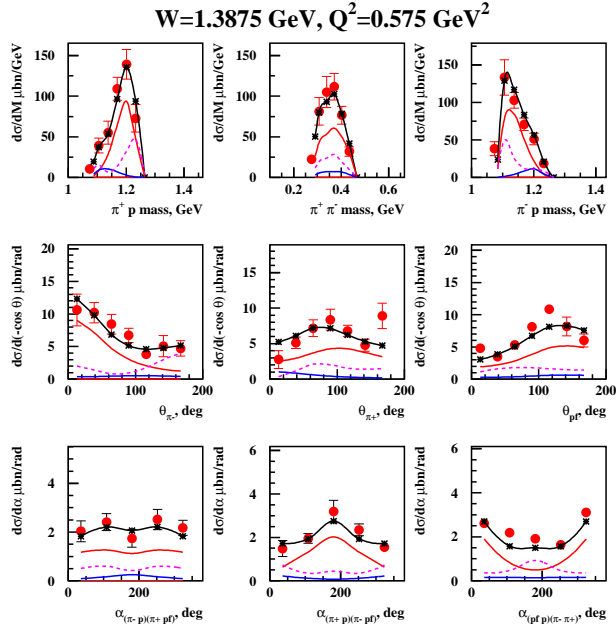


Figure A.76: 2π cross sections as function of hadronic variables fitted within a framework of JM05: black curve - total 2π cross section, red - $\pi^- \Delta^{++}$ channel, blue - $\pi^+ \Delta^0$, dashed magenta - direct 2π production.

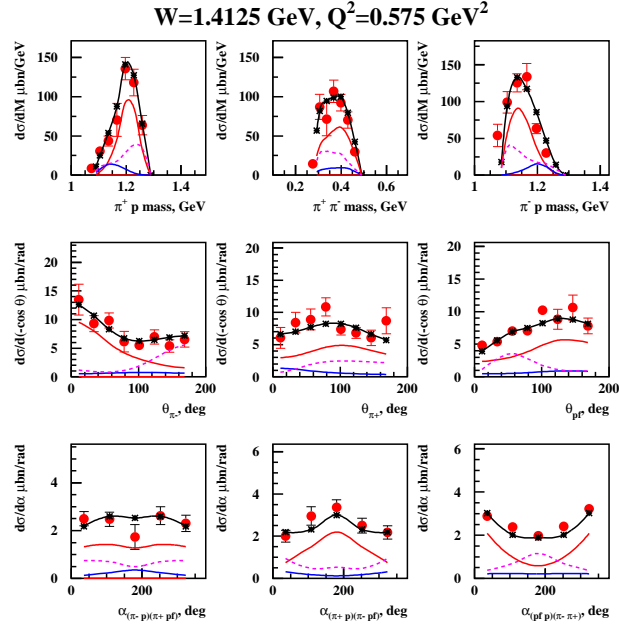


Figure A.77: 2π cross sections as function of hadronic variables fitted within a framework of JM05: black curve - total 2π cross section, red - $\pi^- \Delta^{++}$ channel, blue - $\pi^+ \Delta^0$, dashed magenta - direct 2π production.

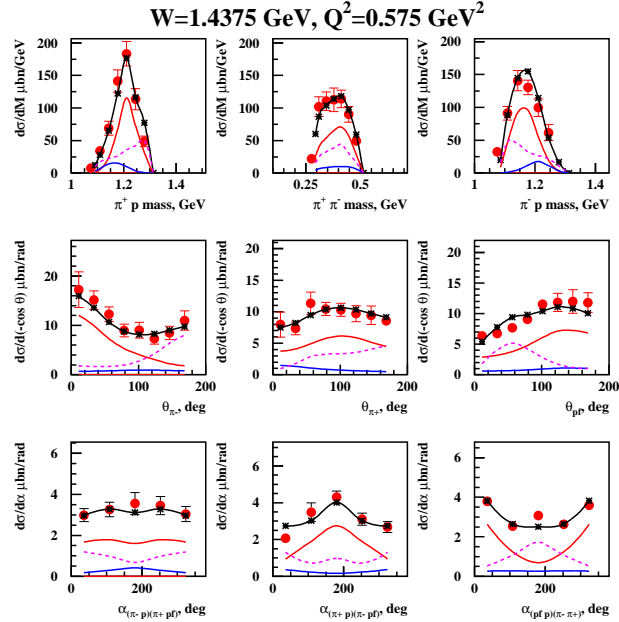


Figure A.78: 2π cross sections as function of hadronic variables fitted within a framework of JM05: black curve - total 2π cross section, red - $\pi^- \Delta^{++}$ channel, blue - $\pi^+ \Delta^0$, dashed magenta - direct 2π production.

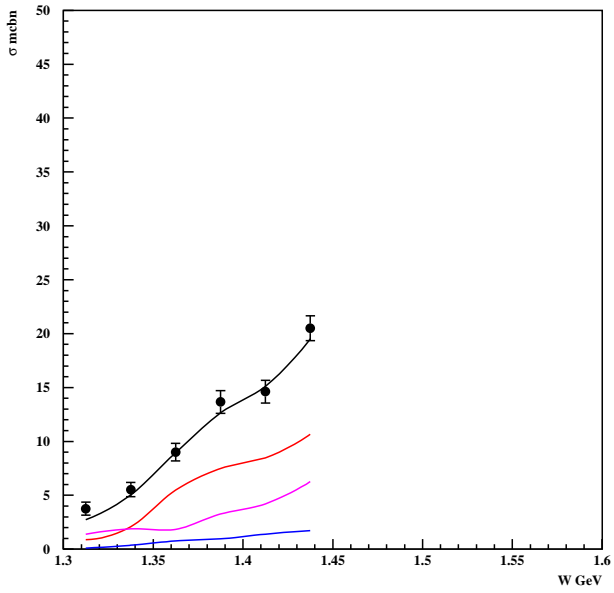


Figure A.79: W dependence of integrated 2π cross section for $Q^2 = 0.575 \text{ GeV}^2$. Black curve - total 2π cross section, red - $\pi^- \Delta^{++}$ channel, blue - $\pi^+ \Delta^0$, magenta - direct 2π production.

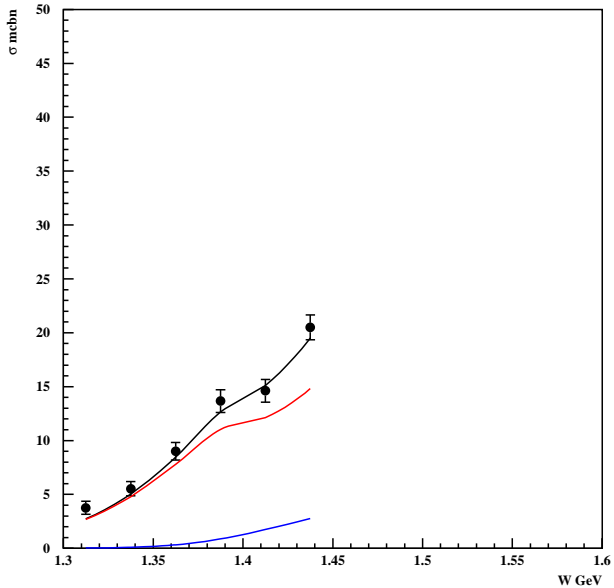


Figure A.80: W dependence of integrated 2π cross section for $Q^2 = 0.575 \text{ GeV}^2$. Black curve - total 2π cross section, red - non-resonant mechanisms, blue - N^* contribution.

Bibliography

- [1] T. Ebata, K. E. Lassia, Phys. Rev. **183**, 1425, (1969).
- [2] V. Mokeev, et. al. Phys. Atom. Nucl. **64**, 1292, (2001).
- [3] V. Burkert ,et. al. Phys. Atom. Nucl. **67**, 1918, (2004).
- [4] V. Mokeev, et. al. to appear in Proc. of NSTAR2004 workshop, April 24-27, 2004, Grenoble, France.
- [5] V. Burkert, T. S.-H. Lee, Jnt. J. Mod. Phys. **E13**, 1035, (2004).
- [6] A. Del Guerra, et. al. Nucl. Phys. **B99**, 253, (1975).
- [7] E. Amaldi, et. al. Phys. Lett. **B41**, 216, (1972).
- [8] P. Joos, et. al. Phys. Lett. **B62**, 230, (1976).
- [9] B. Jula-Diaz, D. O. Riska, F. Coester, Phys. Rev. **C70**, 045204, (2004).
- [10] A. W. Thomas, Annalen. Phys. **13**, 731, (2004).
- [11] I. G. Aznauryan, et. al. Phys. Rev. **C71**, 015201, (2005).
- [12] L. Ya. Glozman, hep-ph/0410194.
- [13] S. Eidelman, et. al. Phys. Lett. **B592**, 1, (2004).
- [14] V. D. Burkert, et. al. Phys. Rev. **C67**, 035204, (2003).
- [15] R. Thompson, et. al. CLAS Collaboration, Phys. Rev. Lett. **86**, 1702, (2001).
- [16] S. Capstick and B. D. Keister, Phys. Rev. **D51**, 3598, (1995).
- [17] E. Pace, G.Salme and S. Simula, Few Body Syst. Suppl. **10**, 407, (1999).
- [18] S. Simula, Proceedings of the Workshop on The Physics of Excited Nucleons, NSTAR 2001, p.135.

- [19] M. Warns, H. Schröder, W. Pfeil and H. Rollnik, Z. Phys. C-Particles and Fields, **45**, 627, (1990).
- [20] M. Aiello, M. M. Giannini and E. Santopinto, J. Phys. G:Nucl. Part. Phys., **24**, 753, (1998).
- [21] F. Gano and P. González, Phys. Lett. **B431**, 270, (1998).
- [22] Z. Li, V. Burkert, Phys. Rev. **D46**, 70, (1992).
- [23] T. P. Vrana, S. A. Dytman, Phys. Rep. **32B**, 184, (2000).
- [24] K. Joo, et. al. Phys. Rev. Lett. **88**, 12200, (2002).
- [25] C. Mertz et. al. Phys. Rev. Lett. **86**, 2963, (2001).
- [26] F. Kalleicher et. al. Z. Phys. **A359**, 201, (1997).
- [27] V. V. Frolov et. al. Phys. Rev. Lett. **82**, 45, (1999).
- [28] G. Blanpied et. al. Phys. Rev. **C64**, 025203, (2000).
- [29] R. Beck et. al. Phys. Rev. **C61**, 035204, (2001).
- [30] T. Pospischil et. al. Phys. Rev. Lett. **86**, 2959, (2001).
- [31] A. Silva et. al. Nucl. Phys. **A675**, 637, (2000).
- [32] S. S. Kamalov et. al. Phys. Rev. **C64**, 033201(R), (2001).
- [33] T. Sato and T. S.-H. Lee, Phys. Rev. **C63**, 055201, (2001).
- [34] L. Tiator et. al. nucl-th/0012046.
- [35] I. G. Aznauryan, Z. Phys. **A346**, 297, (1993).
- [36] K. Egian, CLAS-NOTE 99-007, (1999).
- [37] http://www.ge.infn.it/~golovach/cooking_status/momcor/momcor.html
- [38] http://www.jlab.org/~vllassov/cc/cc_e1b_eff/e1b_1500.html
- [39] STATISTICAL METHODS IN EXPERIMENTAL PHYSICS. By W. T. EADIE, D. DRYARD, F. E. JAMES, M. ROOS. CERN, Geneva (and university of Helsinki). NORTH-HOLLAND PUBLISHING COMPANY, AMSTERDAM, LONDON, 1971.
- [40] L. W. Mo, Y. S. Tsai, Rev. Mod. Phys. **41**, 205, (1969).
- [41] TWO PION ELECTROPRODUCTION WITH THE CLAS DETECTOR AT JEFFERSON LABORATORY. By M. Ripani, et. al. Nucl. Phys. **A663**, 675-678, (2000).

- [42] PHENOMENOLOGICAL MODEL FOR DESCRIBING PION PAIR PRODUCTION ON A PROTON BY VIRTUAL PHOTONS IN THE ENERGY REGION OF NUCLEON RESONANCE EXCITATION. V. I. Mokeev et. al. Phys. Atom. Nucl. **64**, 1292-1298, (2001).
- [43] NEW POSSIBILITIES FOR STUDYING NUCLEON RESONANCES IN THE PRODUCTION OF PI+ PI- PAIRS BY POLARIZED ELECTRONS ON AN UNPOLARIZED PROTON. V. Burkert et. al. Phys. Atom. Nucl. **67**, 1918-1922, (2004).
- [44] ABBHHM Collaboration, Phys. Rev. **175**, 1669 (1968).
- [45] PHENOMENOLOGICAL ANALYSIS OF THE CLAS DATA ON DOUBLE CHARGED PION PHOTO AND ELECTRO-PRODUCTION. By V. I. Mokeev, V. D. Burkert, L. Elouadrhiri, A. A. Boluchevsky, G. V. Fedotov, E. L. Isupov, B. S. Ishkhanov, N. V. Shvedunov. International Workshop on the Physics of Excited Baryons (NSTAR 05), Tallahassee, Florida, 10-15 Oct 2005.
- [46] P. E. Bosted, "Empirical fit to the nucleon electromagnetic form factors", Phys. Rev. **C51**, 409, (1995).
- [47] M. Ripani, V. Burkert, V. Mokeev "Measurement of Two Pion Decay of Electroproduced Light Quark Baryon States with CLAS", CLAS-ANALYSIS 2002-109.
- [48] A. Afanasev, I. Akushevich, V. Burkert, K. Joo, " QED radiative corrections in processes of exclusive pion electroproduction", Phys. Rev. **D66**, 074004, (2002).